



저작자표시-비영리-변경금지 2.0 대한민국

이용자는 아래의 조건을 따르는 경우에 한하여 자유롭게

- 이 저작물을 복제, 배포, 전송, 전시, 공연 및 방송할 수 있습니다.

다음과 같은 조건을 따라야 합니다:



저작자표시. 귀하는 원저작자를 표시하여야 합니다.



비영리. 귀하는 이 저작물을 영리 목적으로 이용할 수 없습니다.



변경금지. 귀하는 이 저작물을 개작, 변형 또는 가공할 수 없습니다.

- 귀하는, 이 저작물의 재이용이나 배포의 경우, 이 저작물에 적용된 이용허락조건을 명확하게 나타내어야 합니다.
- 저작권자로부터 별도의 허가를 받으면 이러한 조건들은 적용되지 않습니다.

저작권법에 따른 이용자의 권리는 위의 내용에 의하여 영향을 받지 않습니다.

이것은 [이용허락규약\(Legal Code\)](#)을 이해하기 쉽게 요약한 것입니다.

[Disclaimer](#)

이학박사 학위논문

**Unconventional Excitation Spectra of
Two-Dimensional Transition Metal
Compounds**

이차원 전이 금속 화합물의 독특한 들뜸 스펙트럼
연구

2019 년 8 월

서울대학교 대학원

물리천문학부 물리학전공

강 순 민

Unconventional Excitation Spectra of Two-Dimensional Transition Metal Compounds

Soonmin Kang

Supervised by
Professor Je-Geun Park

A Dissertation submitted to the Faculty of Seoul National
University in Partial Fulfillment of the Requirements for the
Degree of Doctor of Philosophy

August 2019

Department of Physics and Astronomy
Graduate School
Seoul National University

Abstract

This thesis delivers “a romance of dimensions” I explored during my PhD. Amongst many dimensions, two-dimensional “Flatland” is quite unexplored but important area especially in the aspect of fundamental degrees of freedom (DOF) in nature. The interplay of DOF and the enhanced quantum fluctuations in two-dimensional (2D) systems often breaks down the classical models in condensed matter, and causes exotic phases such as quantum spin liquids, unconventional superconductivity and quantum Hall effects. The comprehensive studies of those phases are significant in both respects of explaining the questions on fundamental physics and driving the development of technology. The purpose of this thesis is to research the DOF and their interactions in strongly correlated system in 2D limits making use of resonant inelastic x-ray scattering (RIXS) technique. RIXS is a state-of-the-art experimental method to investigate various excitations implying the energy difference between the ground and excited states in the materials. Specifically, I investigate the magnetic structure and the exotic phase from a strong spin-charge coupling in NiPS₃, and the metal-insulator transition (MIT) induced by quantum confinement effects in SrRuO₃ thin film.

NiPS₃ shows a zigzag-type antiferromagnetic order below the transition temperature 160 K. The high-resolution Ni L_3 edge RIXS gives an important evidence to resolve the exact magnetic structure with both single-magnon dispersion and two-magnon continuum. The XXZ-type model Hamiltonian can give a clue to understanding the ideal 2D XY model. In

addition, the small charge transfer energy between Ni and S forms complex multiplet states from the bonding of different electronic configurations. For this reason, the strong spin-charge coupling is observed through the unusual excitation attributed to the spin-flip of ligand hole and the formation of Zhang-Rice singlet states. The experimental results are interpreted by configuration interaction calculation and spin wave calculation.

In the case of SrRuO₃, the electronic structure of thin films as a function of thickness from the bulk limit to monolayer is examined via O *K* edge RIXS experiments. The study clarifies the interplay of orbital and charge DOF. I verified the orbital-selective quantum confinement effects (QCE), which splits the orbital levels of Ru, from the charge-transfer excitations. Moreover, the evidence of the MIT, the suppression of electron-hole continuum, coincides with the QCE at the same critical thickness. The result of RIXS experiments suggest that QCE by the geometrical restriction gives rise to MIT in ultrathin films.

Keywords: Resonant inelastic x-ray scattering (RIXS), Strongly correlated electron system, Magnetic van der Waals material, Spin-charge coupling, Magnon, Multiplet structure, Configuration interaction calculation, Quantum confinement effects

Student Number: 2013-20350

Abstract	i
List of Tables	vi
List of Figures	vii
1 Introduction	1
1.1 Two-dimensional systems in condensed matter physics	1
1.1.1 Strongly correlated systems	1
1.1.2 Novel phases in two-dimensional systems	3
1.2 Resonant inelastic x-ray scattering (RIXS) technique	5
1.2.1 Basic principles	7
1.2.2 Features of RIXS	10
1.2.3 Elementary excitations in strongly correlated systems	14
1.3 Outline of thesis	18
2 Experimental Details	23
2.1 Sample preparation	23
2.1.1 Chemical vapor transport method	24
2.1.2 Single crystal x-ray diffraction	26
2.2 RIXS experiments in large facilities	28
2.2.1 Choice of incident energy	29
2.2.2 Single crystal experiment on I21 at DLS	31
2.2.3 Thin film experiment on ADRESS at PSI	33

3	Exotic magnetic excitations in van der Waals antiferromagnet NiPS₃	37
3.1	Magnetism in two-dimensional van der Waals materials	37
3.1.1	Fundamental theories on 2D magnetism	37
3.1.2	Magnetic van der Waals materials	42
3.2	Magnetic structure of NiPS ₃	44
3.3	RIXS experiment on NiPS ₃	45
3.3.1	Result: XAS and overall RIXS spectra	46
3.3.2	Discussion 1: Configuration interaction calculations	49
3.3.3	Discussion 2: Multiplet structure of NiS ₆	52
3.3.4	Discussion 3: Spin-charge coupling	56
3.3.5	Discussion 4: Magnon dispersions	61
3.4	Conclusion	63
 4	 Orbital-selective confinement effect and metal-insulator transition of Ru 4<i>d</i> orbitals in SrRuO₃ ultrathin film	 68
4.1	Quantum confinement effect in low dimensional systems	68
4.1.1	General description of quantum confinement effects	68
4.1.2	Quantum confinement effects and magnetic transition in SrRuO ₃ thin films	70
4.2	Metal-insulator transition in SrRuO ₃ thin films	73
4.3	RIXS experiment in SrRuO ₃ thin films	74

4.3.1 Results: XAS and RIXS spectra as a function of thickness	74
4.3.2 Discussion 1: Configuration interaction calculations	79
4.3.3 Discussion 2: Quantum confinement effects	83
4.3.4 Discussion 3: Metal-insulator transition	85
4.4 Conclusion	88
5 Summary and outlook	92
Publication lists	95
국문 초록 (Abstract in Korean)	97
감사의 글 (Acknowledgement)	100

List of Tables

3.1	Physical parameters for the CI calculation in units of eV	49
3.2	The parameters used in spin wave calculations (in meV)	62
4.1	Physical parameters used for the CI calculations (in eV)	83

List of Figures

1.1	The emergent phenomena induced by the interaction of four fundamental degrees of freedom [Ref.1.15-19]	2
1.2	The schematic view of two-step process in RIXS	6
1.3	Schematic diagram of the process of XAS, XES, and RIXS. XAS investigate the unoccupied valence levels while the XES observes the occupied valence level [Ref.1.42]	8
1.4	Kinetic energy and momentum carried by the photon, electron and neutron [Ref.1.31]	11
1.5	Absorption edges of different chemical elements [Ref. 1.32,33]	12
1.6	The real part of the angular wave functions of five d orbitals. In the cubic crystal field, the degeneracy is lifted two e_g orbitals and three t_{2g} orbitals [Ref.1.41]	13
1.7	Elementary excitations in solids and their approximate energy scales in strongly correlated [Ref.1.31]	14
1.8	Collective magnetic excitations in $Sr_{14}Cu_{24}O_{41}$ [Ref.1.40] (a) Dispersion of magnetic excitations in Cu L_3 RIXS, (b) The momentum and energy transfer of two-triplons in $Sr_{14}Cu_{24}O_{41}$, (c) Polarization dependence of RIXS spectrum	17
2.1	Schematic view of the entire process of chemical vapor transport method using two-zone furnace	26

2.2	Picture of single crystal x-ray diffractometer (XtaLAB P200, Rigaku) and the four motors in this instrument	27
2.3	Picture of NiPS ₃ single crystal mounted on the sample stage and the analysis results from the SC-XRD	28
2.4	Classification of x-ray absorption edges	29
2.5	Picture of I21 at DLS and the schematic view of beamline from the undulator of synchrotron to detector across five different mirrors, sample and grating [Ref.2.4]	32
2.6	Schematic view of ADDRESS [Ref.2.5]	34
2.7	The photon flux with different polarizations: Linear horizontal (LH), linear vertical (LV) and circular (C) polarizations	34
3.1	The schematic view of three different types of magnetic ordering in 2D limits. The left shows the Ising type that has only 1D DOF, the middle model corresponds to XY-type, and the right one does to Heisenberg-type [Ref.3.10]	41
3.2	The schematic view of vortex-antivortex pairs in the lattice [Ref.3.15]	41
3.3	Possible physical issues and phases in magnetic vdW materials [Ref.3.10]	43
3.4	The different types of antiferromagnetic ordering in TMPS ₃ materials. (a) XY-type model of NiPS ₃ and CoPS ₃ , (b) Heisenberg-type model of MnPS ₃ , and (c) Ising-type model of FePS ₃ [Ref.3.26]	45
3.5	The results of fluorescence XAS of NiPS ₃ near Ni L ₃ edge at 14 K. The black and red lines show the experimental results with linear vertical and horizontal polarization. The blue and purple bar graphs demonstrate the distinct multiplet ground states calculated by	

configuration interaction calculation with NiS₆ cluster. The main absorption peak A is at 857.3 eV, and there are several satellite peaks above the main line. Among the satellite peaks, the first satellite peak B at 858.1 eV originates from $d^9\bar{L}^1$ ground states 47

3.6 (a) The experimental results and (b) theoretical description of RIXS maps as a function of incident energy containing a main absorption and a satellite peak region. The red dashed lines on both maps indicate the energy where the sharp peak at 1.45 eV has the strongest intensity, and the energy corresponds to the satellite peak in XAS 48

3.7 Schematic diagrams of NiS₆ and Ni₂S₁₀ clusters with open boundary condition. x , y , z (marked as black arrows) are local coordinates of NiS₆ octahedron where a , b , c (marked as blue arrows) are global coordinates of lattice. $\hat{x} = \sqrt{\frac{1}{6}}\hat{a} - \sqrt{\frac{1}{2}}\hat{b} + \sqrt{\frac{1}{3}}\hat{c}$, $\hat{y} = \sqrt{\frac{1}{6}}\hat{a} + \sqrt{\frac{1}{2}}\hat{b} + \sqrt{\frac{1}{3}}\hat{c}$, and $\hat{z} = -\sqrt{\frac{2}{3}}\hat{a} + \sqrt{\frac{1}{3}}\hat{c}$ 50

3.8 (a) The Tanabe-Sugano diagram of NiS₆ cluster as functions of hopping strengths between Ni 3*d* valence and S 3*p* ligand orbitals. r is the scale parameter of hopping strengths like $V_{pd\sigma} = -0.74 \times r$ and $V_{pd\pi} = 0.4 \times r$ eV. Each line shows different states with distinct symmetry whose irreducible representation is marked, respectively. (b) Schematic diagram of bonding nature between two multiplet states with d^8 and $d^9\bar{L}^1$ electronic configuration. The black thick bars are the multiplet states with $d^9\bar{L}^1$. The left and right side represent the $pd\sigma$ - and $pd\pi$ -type bonding between d^8 and $d^9\bar{L}^1$ multiplets 53

3.9 Energy splitting of $d^9\bar{c}^1$ and $d^{10}\bar{c}^1\bar{L}^1$ multiplets depicted with respect to the difference between the incident energy (ω_{in}) and the ground energy of final state (ω_0). The second column manifests the energy splitting of multiplet states with the combined

electronic configurations of $d^9\underline{c}^1$ and $d^{10}\underline{c}^1\underline{L}^1$ when $V_{pd\sigma} = -0.74$ and $V_{pd\pi} = 0.4$ eV ($r = 1$). Whereas, the first and third columns shows those for $d^9\underline{c}^1$ and $d^{10}\underline{c}^1\underline{L}^1$ configurations, respectively, without the hopping strength. Widths of magenta and cyan parts of lines at second column represent partial contributions of $d^9\underline{c}^1$ and $d^{10}\underline{c}^1\underline{L}^1$ on the multiplet states, respectively. The black arrows marked with ‘A’, ‘B’, ‘C’, and ‘D’ indicate the peak positions of theoretical XAS spectra 55

3.10 The schematic view of RIXS process occasioning Zhang-Rice singlet state. The arrows painted in blue and red color imply the spin states of the holes in each orbital. In the intermediate state of RIXS process, the spin is flipped due to the spin-orbit coupling and the potential of core-hole. Once the flipped spin is transferred to 3d orbital, it establish the singlet state with neighboring ligands 56

3.11 Schematic diagram of spin configurations in (a) Zhang-Rice-triplet lattice and (b) a Zhang-Rice-singlet excited lattice with on zigzag antiferromagnetic order. Large (small) red and blue arrows refer to the spin direction of Ni 3d (S 3p) holes. Green ellipsoids indicate edge-shared S sites in which spins of two ligand holes are antiparallel. A black dashed circle highlight the site of ZRS. The shaded arrow inside the circle represents the direction of expected electric dipole for the ZRS 58

3.12 The temperature dependence of ZRS peak. At the low temperature, the peak width of ZRS peak is comparable to the energy resolution 60

3.13 Magnon dispersion and two-magnon continuum in XXZ-type antiferromagnet NiPS3. (a) Low energy excitations in RIXS spectra with Q_{\parallel} dependence along b^* axis at 15 K. Black squares and red circles respectively correspond to the fitted magnon and two-

magnon energies. (b) Calculated magnon spin waves and two-magnon DOS using parameters described in Table 3.2. (c) Temperature dependence of low energy excitations. The blue colored shaded peak shows a fitting result of two-magnon continuum at 15 K. The inset graph indicates the intensity of two-magnon continuum as a function of temperature 63

4.1 Confined electron wave vectors in ultrathin films whose thickness is from one to four monolayers [Ref.4.2] 69

4.2 Variation of nonmagnetic and magnetic partial density of states as a function of thickness of films [Ref.4.6] 72

4.3 Schematic view of typical change of van Hove singularity in different dimension limits 72

4.4 The mechanism of orbital-selective quantum confinement effects inducing metal-insulator transition in SrRuO₃ thin films 74

4.5 XAS results as a function of the thickness of the sample. An energy of 529.8 eV was utilized for our RIXS experiments since other peaks mainly originate from the SrTiO₃ substrate [Ref.4.23] 75

4.6 (a) and (b) Overall feature of O K edge RIXS spectra with σ and π polarizations for SrRuO₃ thin films. As the thickness decreases, the peak on the low-energy side (dot line) becomes weaker, while the peak at 5 eV (dashed line) gets stronger for both polarizations. In addition to the 5 eV peak, the peak around 4.5 eV (dash-dotted line) also appears for the σ polarization. Note that this 4.5 eV peak becomes stronger below the 5-u.c. sample and

shifts towards higher energy with decreasing thickness. (c) The whole spectrum for the 1-u.c. sample with σ polarization. Altogether, seven Gaussian fitting functions are needed to fit the spectra based on the theoretical calculations explained in discussions. Different types of peaks are marked by different letters in (c) [Ref. 4.23] 77

4.7 (a) RuO₆ cluster used in the configuration interaction calculation. (b) and (c) Schematic view of charge transfer and d-d excitations. Oxygen 1s electrons are excited to vacant 2p levels which are hybridized with Ru t_{2g} orbitals. The energy losses should be different depending on orbitals from which the relaxation occurs. The top panel in (c) shows t_{2g}-eg excitations, and the bottom one indicates the charge transfer from O 2p to Ru 4d levels [Ref.4.23] 78

4.8 Low-energy RIXS spectra of 1 u.c. SrRuO₃ with the CI calculation of a Ru-O-Ru cluster. The symbols represent the experimental results, while the lines show the theoretical results, with different colors used for the different polarizations of the incident beam. The peak at 2 eV shows intersite d-d excitations 82

4.9 RIXS spectra with the results of CI calculation for monolayer SrRuO₃. The symbols represent the experimental results, while the lines show the theoretical results, with different colors used for the different polarizations. (Left) Calculation results with nonbonding p orbitals; (right) calculation results with bonding states 85

4.10 (a) and (b) Low-energy excitations are compared to the JDOS from the DFT calculation. We clearly observe the electron-hole continuum in the thick sample, which arises from its metallic phase. The intensity of peak A sharply decreases below 5 u.c., and it completely disappears for the monolayer SrRuO₃. (c) Electrical resistivity of SrRuO₃

thin films with different thickness. The resistivity increases progressively with reducing the thickness and crosses the theoretical Mott-Ioffe-Regel limit between 4 and 5 u.c. It is notable that the critical thickness from RIXS and the resistivity coincide with one another 87

Chapter 1

Introduction

1.1 Two-dimensional systems in condensed matter physics

1.1.1 Strongly correlated electron systems

With its curiosity leading the nature and progress of technology, mankind has widened the view of world, explaining and connecting the each part of its surrounding world. The field of condensed matter physics has emerged as an intense attempt, and now deals with the macroscopic and microscopic physical properties of matter.

Following the forerunners of E. Rutherford, N. Bohr, J. van der Waals and P. Drude [Ref.1.1-4], who built the foundation of this field, W. Pauli, A. Sommerfeld, F. Bloch, J. Maxwell and other physicists [Ref.1.5-8] have led the mainstream of modern condensed matter physics. Their contribution has heralded the advent of quantum mechanics and modern many-body physics. As a result, those fundamental theories and discoveries have boosted the technology such as transistor or magnetic storage devices.

While the early stage focused on the certain factors in the materials such as electron or spins, studies in modern condensed matter physics handles more complicated items, so-called “emergent phenomena”. One of the most famous examples is the superconductivity

[Ref.1.9, 10], which is induced by ‘pair’ or interaction between the electrons. Starting from the BCS-based superconductivity, the emergence of phenomena such as High- T_c superconductivity [Ref.1.11], multiferroicity [Ref.1.12], metal-insulator transition [Ref.1.13], and recent topological insulator [Ref.1.14] have been intensively investigated. The common feature of these examples is the strong interplay of four fundamental degrees of freedom (DOF) in solid; spin, charge, lattice and orbital (figure 1.1).

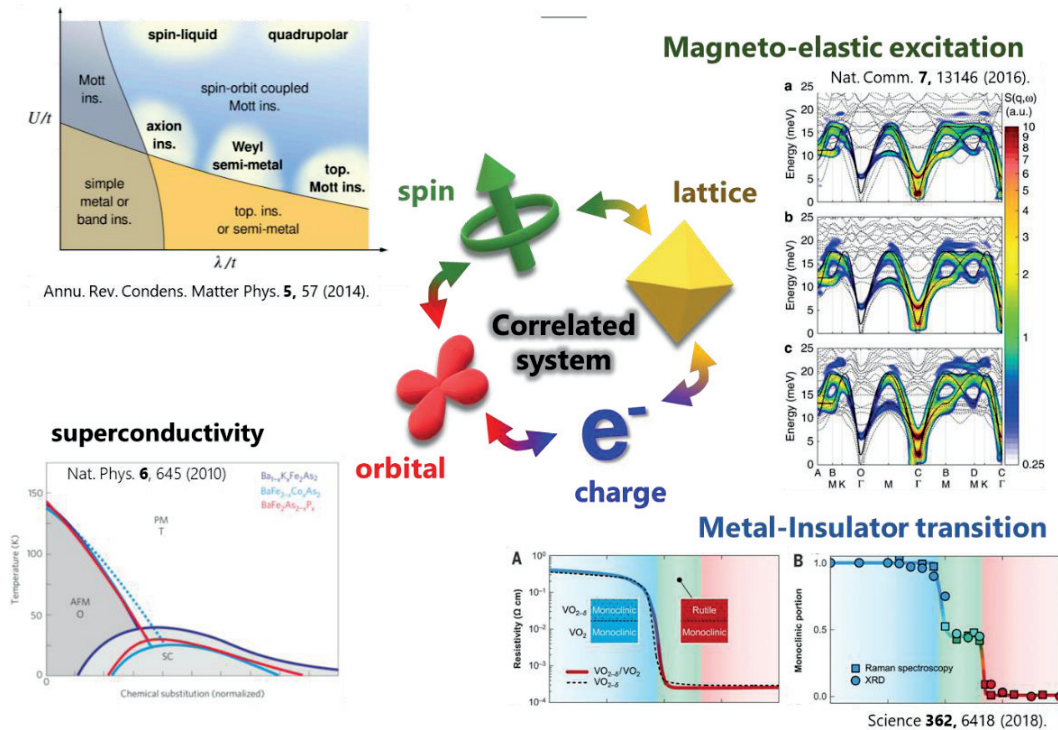


Figure 1.1. The emergent phenomena induced by the interaction of four fundamental degrees of freedom [Ref.1.15-19].

The category of materials showing emergent phenomena due to the interaction of DOF is called strongly correlated electronic system. The emergent phenomena of strongly

correlated systems are one of the most interesting but, simultaneously, most difficult topics to investigate due to their complexity. Not only do the individual factors of the system have importance in fundamental physical view but also the correlations between (or among) those factors connote a significance to the behavior in the whole system.

1.1.2 Novel phases in two-dimensional systems

When the strongly correlated system comes to low-dimensional limits, the interaction itself should be modified [Ref.1.19]. As the electrons or interactions in the system are confined geometrically, it often experience strong ‘quantum’ fluctuations showing unique phases. More precisely, quantum fluctuations get stronger than thermal fluctuations and survive longer in low-dimensional systems. In this regime, the mean-field theory, which explains the infinite dimensional cases, is no longer accurate. Thus, this leads to novel phases in low-dimensional materials compared to the classical physical phenomena in three-dimensional systems.

The quantum fluctuations indicate the temporary change in the energy in a certain space, due to Heisenberg’s uncertainty principle. From the quantum fluctuations perspective, the higher dimensions have more phase space for their spreading out. As the dimension decreases, a local disturbance or thermal fluctuation becomes small, which makes the quantum fluctuations to survive more easily in the system without decaying. That is to say, the strong quantum fluctuation destroys the classical models of solids. Thus, in a one-dimensional case, the quantum fluctuations freely propagate in the only one domain. This

makes the interaction in one-dimension play a different role for a system to have a more collective nature, which induces unique phases such as Luttinger liquids or spin-singlet states [Ref.1.20-22].

The two-dimensional system is quite special ground of investigating large quantum fluctuations without encountering the unique domain of one-dimension. One of the most famous examples is a fractional quantum spin-liquid phase [Ref.1.23]. This phase originates from the competition between the Néel-ordered state and the singlet state. On the other words, there can be a novel phase due to the competition of purely classical model and purely quantum mechanical concepts in the two-dimensional systems.

There can be two ways to reach two-dimension in the real world. One is to make layered structure where the inter-layer interaction is small enough to neglect compared to intra-layer one (Chapter 3) and the other way is to artificially make monolayer structure (Chapter 4). Former class of materials called layered van der Waals (vdW) materials, such as graphene, transition-metal (TM) dichalcogenides and TM phosphorus trichalcogenides ($TMPX_3$; $TM = 3d$ transition-metals, $X =$ chalcogens) have been investigated extensively over the last decade [Ref.1.24-28]. Especially, the magnetic vdW materials $TMPX_3$ provides a unique opportunity to study strongly correlated electronic systems in the two-dimensional limits as they have a unique spin DOF. In the latter cases, we can make use of thin films of TM oxides with perovskite [Ref.1.29-30]. Unlike three-dimensional cases, it is possible to confine the electronic interaction, which leads to distinct phases such as quantum Hall effects or magnetic skyrmions.

1.2 Resonant inelastic x-ray scattering technique

The conventional experiments such as bulk property measurements or optical spectroscopies have limitations in explaining complex interaction in the strongly correlated electron systems. Resonant inelastic x-ray scattering (RIXS) is a unique state-of-art technique to investigate the whole elementary excitations and their interactions at the same time. RIXS is composed of two step processes; ‘photon-in’ and ‘photon-out’ (Figure 1.2). This means that an electron is excited by the incident x-ray and relaxed with scattered photons. Between these processes, photons lose a certain amount of their energy to the sample and this corresponds to the energy different of distinct electronic states in a sample. The term of ‘inelastic’ means this energy loss in the RIXS process.

The term of ‘resonant’ indicates the energy irradiated to a target. The energy of the incident beam corresponds to a certain resonant energy (the so-called absorption edges) of the target, which is the exact energy difference between the atomic core level and a valence band level above the Fermi energy. This ‘resonance’ is one of the most powerful aspects of RIXS because one can enhance the cross-section of excitations by three or more orders of magnitude. For example, when we use Ni L-edge as an incident photon energy, an electron at $2p$ core level is excited to empty $3d$ states. After a short time, depending on the type of excitations, another electron fills the core hole with scattered photon leaving an excited states in the sample. As one utilizes the resonant energy, it is possible to measure magnetic excitations, or even single-magnon itself in this special case. The further features of RIXS will be described in the following sessions.

The objective of RIXS is to observe dispersion of excitations. This means we can measure both the energy and momentum loss. As we choose the energy and momentum of the incident x-ray beam, it is possible to calculate the energy and momentum losses in the samples by just measuring the properties of outgoing photons. From this, in principle, one can probe all the excitations in the sample from four elementary excitations to their interactions.

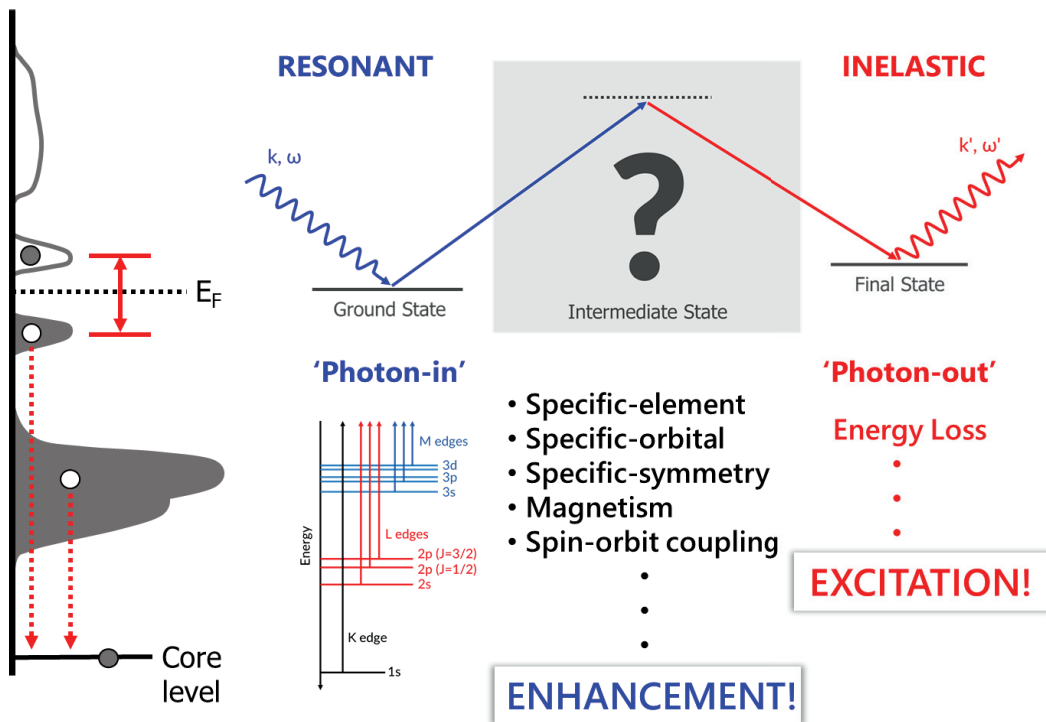


Figure 1.2. The schematic view of two-step process in RIXS.

1.2.1 Basic principles

Roughly speaking, RIXS is the combination of two distinct spectroscopies: x-ray absorption spectroscopy (XAS) and x-ray emission spectroscopy (XES). Typical XAS indicates the absorption of certain quantities of x-ray photons by a chemical elements due to the promotion of elements from an atomic orbital to another one. By analyzing the wavelength of the incident beam, one can determine the unoccupied levels because the results include the quantity of energy that is needed to excite an electron from a core level to an unoccupied level. Since the excited state is unstable, the promoted electron should be relaxed right after the process. The remaining energy is transferred to x-ray photon or another electron. This kind of electron called Auger electron can experience secondary or higher-order processes called total electron yield. In typical XAS experiments, one measure the quantity of this total electron yield or the radiative decay called fluorescence yield. On the other hand, XES investigates the occupied valence levels. In this experiment, the energy of the incident beam is not in concern as long as it is larger than the difference between the core and unoccupied states (Figure 1.3). Once a core hole is generated, another electron initially at occupied valence level fills the core hole. XES observes this process by counting the emitted x-ray photons.

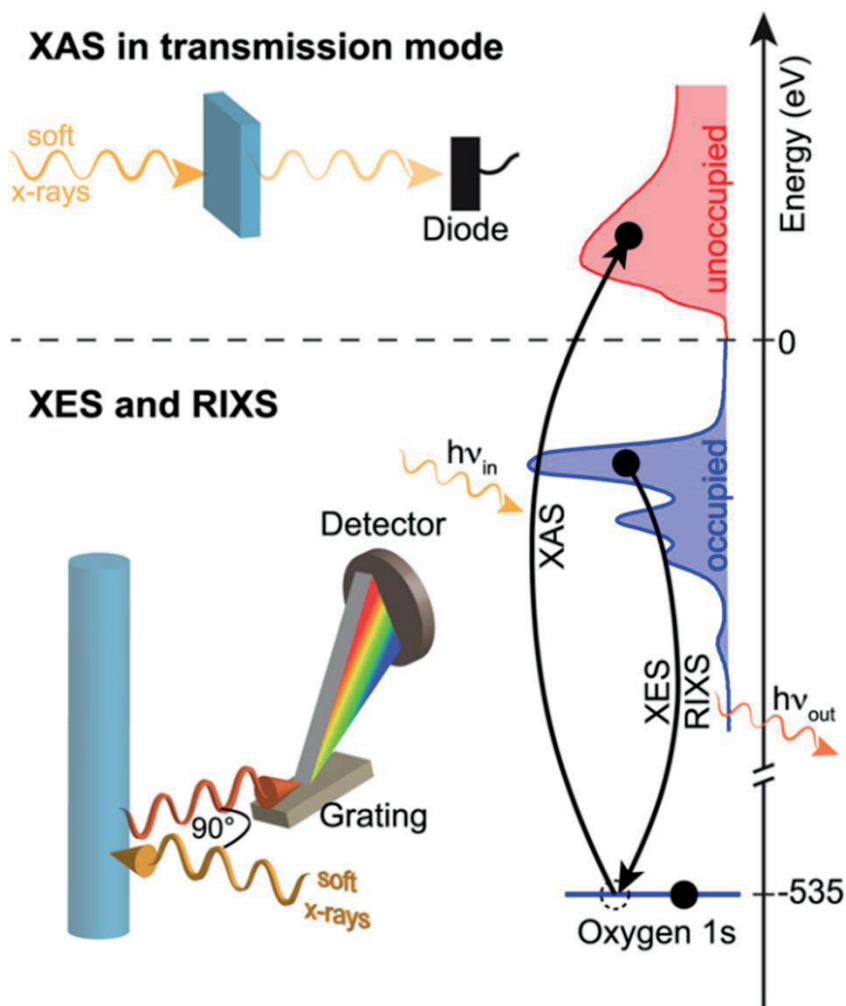


Figure 1.3. Schematic diagram of the process of XAS, XES, and RIXS. XAS investigate the unoccupied valence levels while the XES observes the occupied valence level [Ref.1.42].

These two traditional experiments are complementary tools to each other since each of them investigates the unoccupied and occupied states, respectively. However, mostly those are considered to be independent. For example, the results of XES are independent of the characteristics of incident beam, which is a crucial factor in XAS. That is to say, XES shows the non-monochromatic excitations that does not have specific intermediate states.

Different from the simple process of XAS and XES, RIXS probes the outgoing x-ray photons that are closely related to the energy and momentum of the incident photons. The excitations in RIXS can be made in two different mechanisms: direct and indirect RIXS. These two mechanisms can be distinguished by detailed scattering process. It is important to differentiate the two processes because each RIXS process allows different scattering channel. In case of direct RIXS, a core electron is excited into the empty state of the valence band, and another electron that is initially at occupied valence level fills the core hole. Thus, this process involves only two states of initial and final ones. The other process of RIXS is indirect one, which has another state called the intermediate states. The strong potential due to the Coulomb interaction of core hole or the Pauli exclusion principle influences the valence electrons in the intermediate state. This core-hole potential excites the valence electrons to another empty valence level in case the photo-excited electron is placed in the conduction band far from the Fermi level. Meanwhile, even when the core electron is promoted to the unoccupied valence level, there can be an indirect RIXS. In this case, the core-hole potential affects to valence electrons and modifies the quantity of electron such as spins.

1.2.2 Features of RIXS

RIXS has several advantages in studying solid materials compared to other spectroscopies since it utilizes resonant x-ray sources. First of all, x-ray photons enable researchers to explore the large scattering phase space compared to optical photon, neutron, or electron sources. It is because the wavelength of the x-ray has the order of a few angstroms, which is relatively comparable to the interatomic lattice spacing in solids. For example, the wavelength of optical photons in visible light is in the order of hundreds nm. If we assume that the wavelength of the optical photon is 500 nm, then their limit of momentum transfer is about $\hbar k = 2\pi\hbar/\lambda = 1.3 * 10^{-3} \hbar\text{\AA}^{-1}$, which is two or three order smaller than the momentum at the edge of the Brillouin zone of typical solids. On the other hand, photon carries much larger energies than neutron or electron that has same particle momentum as shown in Figure 1.4. This means RIXS can measure much higher energy losses than other inelastic scattering experiments using electrons or neutrons.

Another big advantage of RIXS comes from ‘resonance’. While the inelastic x-ray scattering only detects the interactions among the charge and lattice of the sample, RIXS can detect the quantities that is related to spin DOF. The resonant energy enhances the intensity of the dipole and even the quadratic terms in the scattering form factors, i.e. increases the cross-section, which is almost neglected in non-resonant scattering experiments. In addition, As the energy of incident beam is tuned to specific energy, which corresponds to the atomic transition, one can choose specific atoms in the sample. The quantity of atomic transition (the so-called absorption edge) is a unique property of atoms,

and even can be distinct depending on the chemical bonding, valencies or position of ions in solids. This characteristics of edge makes RIXS possible to measure specific ions in the sample. For example, in the thin film experiments like SrRuO₃ on SrTiO₃ substrate, both the sample of interest and the substrate have oxygen ions. However each oxygen ion has different chemical bonding in different circumstance so it is possible to choose incident energy to investigate the sample of interest from XAS results (Figure 1.5). In addition, by tuning the incident energy to different absorption edges of same chemical element, one can measure different types of spectra with changing the intensity of each excitations.

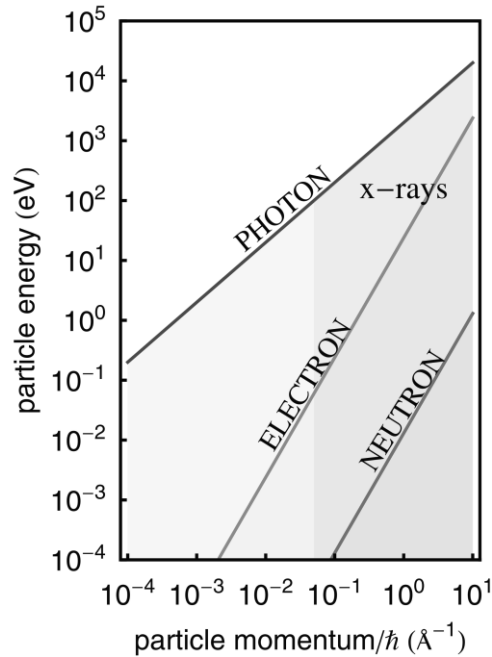


Figure 1.4. Kinetic energy and momentum carried by the photon, electron and neutron [Ref.1.31].

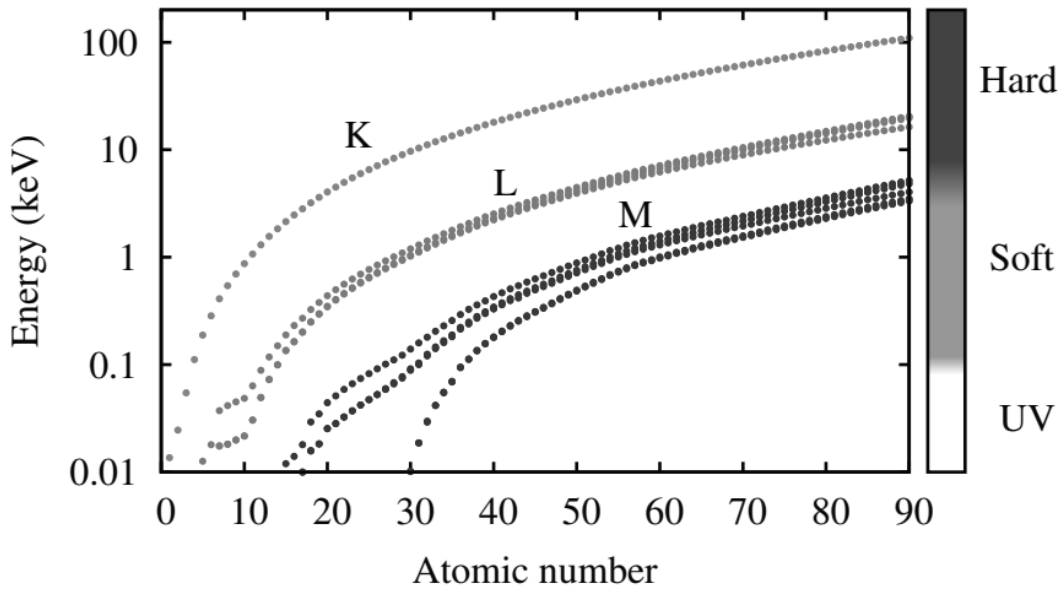


Figure 1.5. Absorption edges of different chemical elements [Ref. 1.32,33].

Third, by changing the polarization of the incident beam, one can choose certain orbitals with different symmetry. The distinct orbitals in the same element have their own geometrical features as shown in Figure 1.6. One can enhance the cross-section of the certain orbitals by choosing different polarization. For example, if one use grazing geometry and use linearly polarized beam, it will be possible to probe the orbitals that aligned to out-of-plane or in-plane separately. In addition, the change of polarization of the photon means the change of an angular momentum. Thus, if it is possible to measure the polarization of scattered photons, one can investigate the additional nature of excitations.

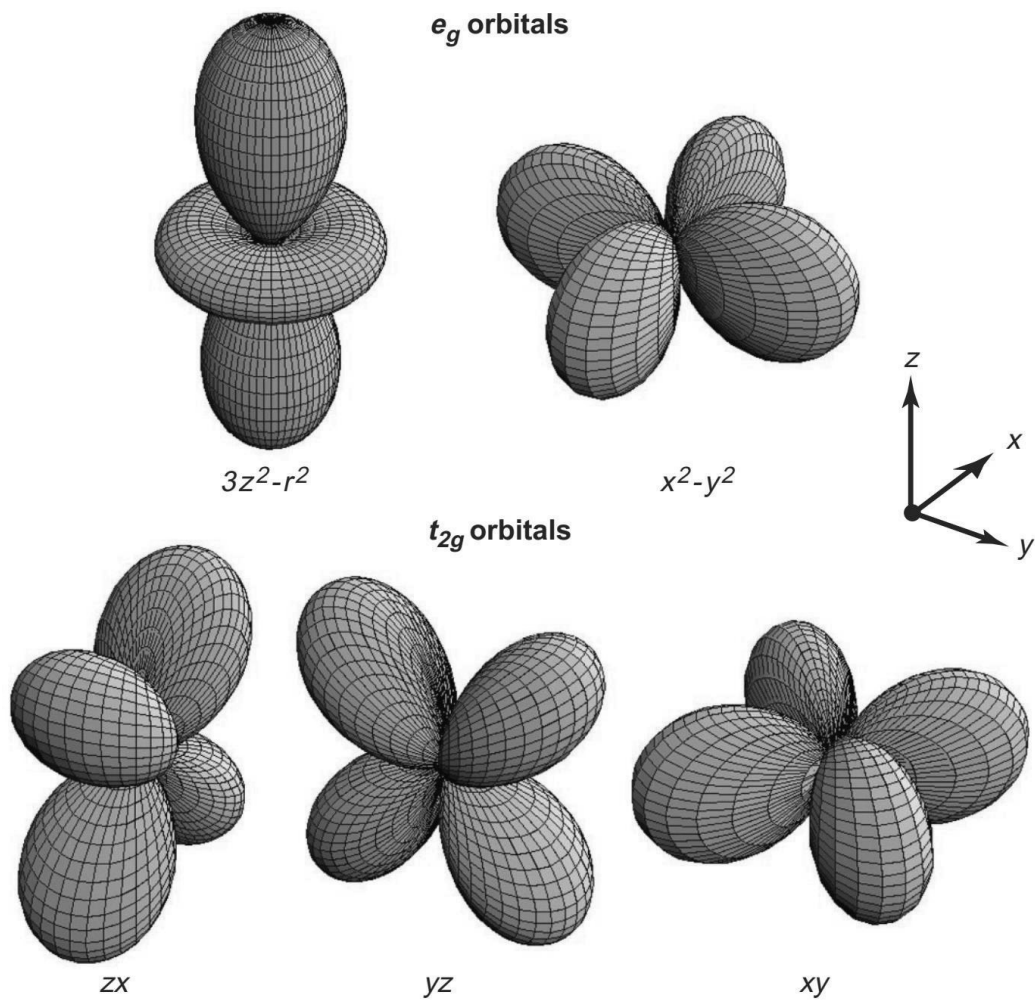


Figure 1.6. The real part of the angular wave functions of five d orbitals. In the cubic crystal field, the degeneracy is lifted two e_g orbitals and three t_{2g} orbitals [Ref.1.41].

RIXS has another advantage of choosing the sample to measure. As the typical penetration depth of x-ray is order of μm depending on its energy, RIXS has bulk-sensitivity. Compared to photoemission spectroscopies, which can only detect the sample surface, RIXS investigate the excitation from the scattering far from the surface of the sample.

1.2.3 Elementary excitations in strongly correlated systems

In condensed matter physics, there are four fundamental DOF including charge, orbital, spin and lattice. As I mentioned above, in principle, it is possible to access to all kinds of excitations with RIXS. Here I discuss how one can detect different elementary excitations related to each DOF and their approximate energy scales: charge-transfer (CT) excitations, orbital excitations, magnetic excitations and phonons.

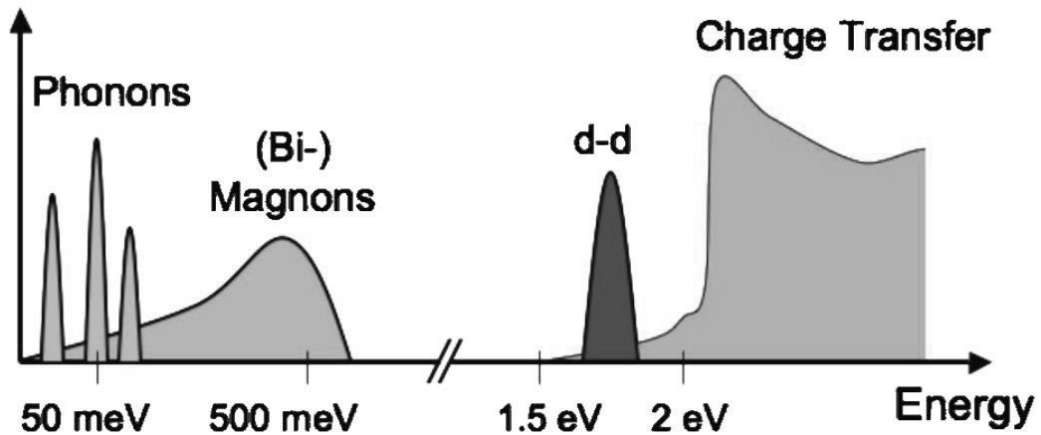


Figure 1.7. Elementary excitations in solids and their approximate energy scales in strongly correlated [Ref.1.31].

The CT excitations refer to the energy needed to transfer an electron from one site to another. The electrons in the ions of the solids are localized due to the large Coulomb interaction between them, which restricts the movement of the charge carriers. The Coulomb repulsion has decisive effect on the distribution of the electrons in the ions of the solids. In this respect, the CT excitations provide the significant information to investigate the electronic band structure. For example, the CT excitations for several TM oxides such as cuprates and nickelates correspond to the lowest excitation across the optical band gap (Ref.1.34). Thus, the excitations provide the information including the size of gap, the electronic transport, collective quasiparticle modes and their life time.

Depending on the type of ions where the transfer occur, we can determine the nature and the energy scale of the excitation. For the material I concern in this thesis, transition metal compounds, there are two CT processes. These processes concern the origin of band gaps and the nature of electron bands including valence and conduction levels. The CT excitations in Mott insulators, which can be explained by Mott-Hubbard theory (Ref.1.35, 36), are related to the charge fluctuations such as $d_i^n d_j^n \leftrightarrow d_i^{n-1} d_j^{n+1}$ (where d_i^n denotes there are n electrons in TM d orbital state on i site). This involves the Coulomb and exchange interaction (U). The other process is affected by another charge fluctuation, namely, ‘charge transfer (Δ)’ rather than U . Δ corresponds to the energy consumed to transfer an electron to TM from a surrounding ligand ($d_i^n \rightarrow d_i^{n+1} \underline{L}$, where \underline{L} denotes a hole in a ligand or vice versa). This kind of insulator called charge transfer insulator and Δ is smaller than U . Thus, U dominates CT excitations in case of Mott insulators ($U > \Delta$) with the order of up to several eVs while Δ gives minimum CT excitation for charge transfer

insulator ($U < \Delta$).

Orbital excitations in RIXS account for orbital DOF in solids. If electrons have orbital DOF, they get two or more choices of orbitals to occupy. It is important to understand orbital DOF especially in the strongly correlated systems of my main interest, because the electrons with orbital DOF partially fill the outer shell. As a result, they always involves magnetic properties. The Coulomb interaction between overlapped orbitals also can influence on the lattice. Like this, the orbitals with DOF are often correlated to other DOF. One of the most famous examples is the Goodenough-Kanamori rule [Ref.1.37, 38], which explains the interatomic spin-spin interactions between the ions depending on the states of overlapping orbitals on lattices. Thus, the understanding of orbital DOF and ground state can widen our knowledge of various emergent phenomena in strongly correlated systems. The simplest case of orbital excitations in RIXS is crystal-field transition commonly shown in Mott insulators. The crystal field involves the degeneracy breaking in orbital energy levels due to the local environment in the crystal. Once the orbital levels are split with crystal field, an electron in an orbital can be transferred to another orbital with different levels. In case the crystal field transitions are concerned in d orbitals, the excitations are called d - d excitations. Depending on the size of crystal field, one can find this excitation from 0.1 to several eVs in RIXS.

Since the RIXS experiments make use of resonant process, it enhance the scattering cross-section of the physical characteristics related to spin DOF, which cannot be detected with nonresonant spectroscopies. As I described above paragraph, most strongly correlated electron systems who carry partially filled outer shell include magnetic ions. The magnetic

interactions among these ions have been one of the most important and long subjects in the field of physics. These interactions often break the spin rotational symmetry, and result in magnetic ordering in the material. Once the spins form magnetic ordering, the collective magnetic excitations can emerge, which lead to quasiparticles such as magnons or spinons. Bimagnons are generated by spin-conserved process so these can be detected by TM or oxygen K-edge RIXS [Ref.1.39]. One should use TM L-edges to investigate magnons because the spin angular momentum of electrons should be 1 to form ‘single’ magnons compared to bimagnons. The energy of magnons is order of tens to hundreds meV for typical transition metal compounds.

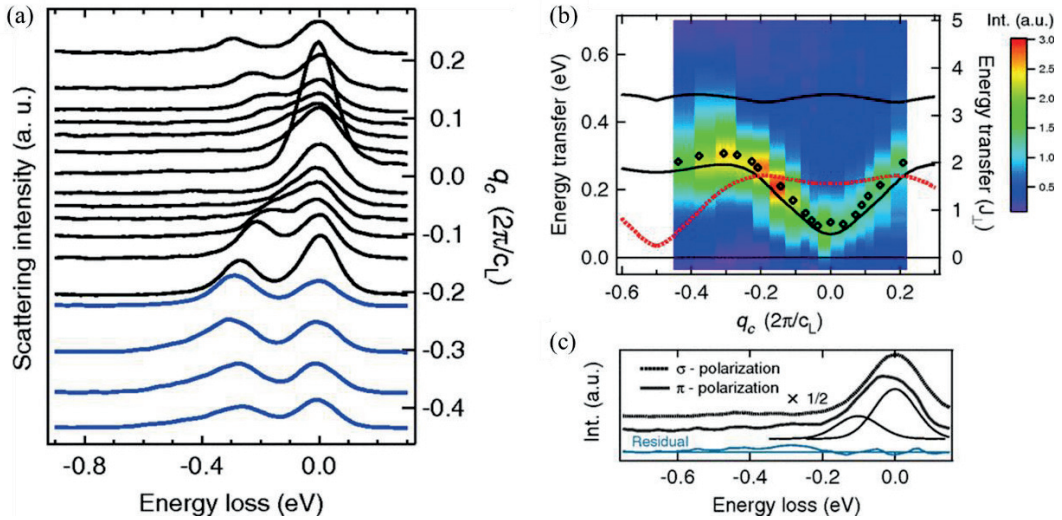


Figure 1.8. Collective magnetic excitations in $\text{Sr}_{14}\text{Cu}_{24}\text{O}_{41}$ [Ref.1.40] (a) Dispersion of magnetic excitations in Cu L_3 RIXS, (b) The momentum and energy transfer of two-triplons in $\text{Sr}_{14}\text{Cu}_{24}\text{O}_{41}$, (c) Polarization dependence of RIXS spectrum.

When the quantum fluctuations or frustrations in the systems increase, this ‘strict’ long-

range magnetic ordering often melts. In this situation, the magnetic moments interact in different way, which results in so-called spin liquid or spin ice states. Such states forms even unconventional magnetic excitations called spinons or triplons [Ref.1.40]. Those excitations have information about magnetic dipole-dipole interactions and the strength of magnetic bonds. Thus, the investigation of magnetic excitations via RIXS explains the spin DOS of strongly correlated systems.

The ions in crystals lie on a periodic lattice. Each atom on the lattice interacts with each other, and makes a certain kind of perturbation. This perturbation induces changes in the distribution of charges or ions in crystal, and forms lattice displacements. These collective lattice excitations due to the displacement of lattice are called phonons. The study of phonons, modes of vibrations, is an important and fundamental part of condensed matter physics because of the basic physical properties such as thermal conductivity and electrical conductivity rely on the vibration modes of solids. The energy of phonons is much smaller than any other electronic excitations (~ 100 meV). It is almost at the limit of the energy resolutions of the state-of-the-art RIXS instrument.

1.3 Outline of thesis

Throughout this thesis, I investigated the elementary excitations and their collective phenomena in strongly correlated electronic systems using the RIXS experiments. Particularly, I focus on the exotic excitations emerging at two-dimensional limits. Chapter 2 contains the experimental details including detailed sample preparations and the detailed

information of RIXS instrument at the large facilities. In the following two chapters, I introduce two case studies of using the RIXS technique. In Chapter 3, the strong spin-charge coupling and related exotic phases is investigated in the vdW antiferromagnet NiPS₃ using Ni *L*₃ edge RIXS. As those subjects are highly attributed to the complex multiplet structure of NiPS₃, I also describe the ground states induced by three different electronic configuration and their bonding states. In Chapter 4, I introduce an O *K* edge RIXS study mostly related to CT and *d-d* excitations. The orbital-selective quantum confinement effect and the metal-insulator transition in SrRuO₃ is the main subject.

References

- [Ref.1.1] E. Rutherford, Lond. Edinb. Dubl. Phil. Mag. **21**, 669 (1911).
- [Ref.1.2] N. Bohr, Lond. Edinb. Dubl. Phil. Mag. **26**, 476 (1913).
- [Ref.1.3] J. D. Van der Waals, Zeitschrift fur Physikalische Chemie **1**, 657 (1894).
- [Ref.1.4] P. Drude, Anna. Der Physik **306**, 566 (1900).
- [Ref.1.5] W. Pauli, Phys. Rev. **58**, 716 (1940).
- [Ref.1.6] A. Sommerfeld, and N. H. Frank, Rev. Mod. Phys. **3**, 1 (1931).
- [Ref.1.7] F. Bloch, Phys. Rev. **70**, 460 (1946).
- [Ref.1.8] J. C. Maxwell, *A Treatise on Electricity and Magnetism* (Clarendon Press, Oxford, 1873).
- [Ref.1.9] H. K. Onnes, Comm. Phys. Lab. Univ. Leiden **122**, 122 (1911).
- [Ref.1.10] C. A. Reynolds, V. Serin, W. H. Wright, and L. B. Nesbitt, Phys. Rev. **78**, 487

(1950).

[Ref.1.11] S. R. Foltyn, L. Civale, J. L. MacManus-Driscoll, Q. X. Jia, B. Maiorov, H. Wang, and M. Maley, *Nat. Mater.* **6**, 631 (2007).

[Ref.1.12] K. F. Wang, J.-M. Liu, and Z. F. Ren, *Adv. in Phys.* **58**, 321 (2009).

[Ref.1.13] M. Imada, A. Fujimori, and Y. Tokura, *Rev. Mod. Phys.* **70**, 1039 (1998).

[Ref.1.14] M. König, S. Wiedmann, C. Brune, A. Roth, H. Buhmann, L. W. Molenkamp, and X.-L. Qi, *Science* **318**, 766 (2007).

[Ref.1.15] J. Paglione, and R. L. Greene, *Nat. Phys.* **6**, 645 (2010).

[Ref.1.16] W. Witczak-Krempa, G. Chen, Y. B. Kim, and L. Balents, *Annu. Rev. Condens. Matter Phys.* **5**, 57 (2014).

[Ref.1.17] J. Oh, M. D. Le, H.-H. Nahm, H. Sim, J. Jeong, T. G. Perring, H. Woo, K. Nakajima, S. Ohira-Kawamura, Z. Yamani, Y. Yoshida, H. Eisaki, S.-W. Cheong, A. L. Chernyshev, and J.-G. Park, *Nat. Comm.* **7**, 13146 (2016).

[Ref.1.18] D. Lee, B. Chung, Y. Shi, G.-Y. Kim, N. Campbell, F. Xue, K. Song, S.-Y. Choi, J. P. Podkaminer, T. H. Kim, P. J. Ryan, J.-W. Kim, T. R. Paudel, J.-H. Kang, J. W. Spinuzzi, D. A. Tenne, E. Y. Tsybal, M. S. Rzechowski, L. Q. Chen, J. Lee, and C. B. Eom, *Science* **362**, 1037 (2018).

[Ref.1.19] S. D. Sarma, S. Adam, E. H. Hwang, and E. Rossi, *Rev. Mod. Phys.* **83**, 407 (2011).

[Ref.1.20] T. Giamarchi, *Quantum Physics in One Dimension* (Clarendon Press, Oxford, 2003).

[Ref.1.21] H. Ishii, H. Kataura, H. Shiozawa, H. Yoshioka, H. Otsubo, Y. Takayama, T.

Miyahara, S. Suzuki, Y. Achiba, M. Nakatake, T. Narimura, M. Higashiguchi, K. Shimada, H. Namatame, and M. Taniguchi, *Nature* **426**, 540 (2003).

[Ref.1.22] J. Friedel, *Phys. Today* **54**, 88 (2001).

[Ref.1.23] R. Coldea, D. A. Tennant, A. M. Tsvelik, and Z. Tylczynski, *Phys. Rev. Lett.* **86**, 1335 (2001).

[Ref.1.24] K. S. Novoselov, D. Jiang, F. Schedin, T. J. Booth, V. V. Khotkevich, S. V. Morozov, and A. K. Geim, *Proc. Natl. Acad. Sci. U.S.A.* **102**, 10451 (2005).

[Ref.1.25] A. K. Geim, and I. V. Grigorieva, *Nature* **499**, 419 (2013).

[Ref.1.26] C. Gong, L. Li, Z. Li, H. Ji, A. Stern, Y. Xia, T. Cao, C. Wang, Y. Wang, Z. Q. Qiu, R. J. Cava, S. G. Louie, and J. Xia, *Nature* **546**, 265 (2017).

[Ref.1.27] C. T. Kuo, M. Neumann, K. Balamurugan, H. J. Park, S. Kang, H. W. Shiu, J. H. Kang, B. H. Hong, M. Han, T. W. Noh, and J. G. Park, *Sci. Rep.* **6**, 20904 (2016).

[Ref.1.28] K. S. Burch, D. Mandrus, and J. G. Park, *Nature* **563**, 47 (2018).

[Ref.1.29] Y. J. Chang, C. H. Kim, S.-H. Phark, Y. S. Kim, J. Yu, and T. W. Noh, *Phys. Rev. Lett.* **103**, 057201 (2009).

[Ref.1.30] S. Kang, Y. Tseng, B. H. Kim, S. Yun, B. Sohn, B. Kim, D. McNally, E. Paris, C. H. Kim, C. Kim, T. W. Noh, S. Ishihara, T. Schmitt, and J.-G. Park, *Phys. Rev. B* **99**, 045113 (2019).

[Ref.1.31] L. J. P. Ament, M. van Veenendaal, T. P. Devereaux, J. P. Hill, and J. van den Brink, *Rev. Mod. Phys.* **83**, 705 (2011).

[Ref.1.32] J. A. Bearden, *Rev. Mod. Phys.* **39**, 78 (1967).

[Ref.1.33] J. W. Robinson, *Practical handbook of spectroscopy* (CRC Press, 1991).

[Ref.1.34] J. Zaanen, G. A. Sawatzky, and J. W. Allen, Phys. Rev. Lett. **55**, 418 (1985).

[Ref.1.35] N. F. Mott, Proc. Phys. Soc. London, Sect. A **62**, 416 (1949).

[Ref.1.36] J. Hubbard, Proc. Roy. Soc. London, Ser. A **277**, 237 (1964).

[Ref.1.37] J. B. Goodenough, Phys. Rev. **100**, 564 (1955).

[Ref.1.38] J. Kanamori, J. Phys. Chem. Solids **10**, 87 (1959).

[Ref.1.39] V. Bisogni, L. Simonelli, L. J. P. Ament, F. Forte, M. Moretti Sala, M. Minola, S. Huotari, J. van den Brink, G. Ghiringhell, N. B. Brookes, and L. Braicovich, Phys. Rev. B **85**, 214527 (2012).

[Ref.1.40] J. Schlappa, T. Schmitt, F. Vernay, V. N. Strocov, V. Ilakovac, B. Thielemann, H. M. Rønnow, S. Vanishri, A. Piazzalunga, X. Wang, L. Braicovich, G. Ghiringhelli, C. Marin, J. Mesot, B. Delley, and L. Patthey, Phys. Rev. Lett. **103**, 047401 (2009).

[Ref.1.41] Y. Tokura, and N. Nagaosa, Science **288**, 462 (2000).

[Ref.1.42] S. Schreck, A. Pietzsch, K. Kunnus, B. Kennedy, W. Quevedo, P. S. Miedema, P. Wernet, and A. Fohlich, Struct. Dyn. **1**, 054901 (2014).

Chapter 2

Experimental Details

2.1 Sample preparation

In this section, I introduce the process of sample preparation for the RIXS experiments. The process includes both sample growth and alignment. First of all, the synthesis of high quality single crystals is essential to performing RIXS experiments. One of the purposes of RIXS is to investigate the momentum dependence of excitations along preferred orientations. Using single crystals instead of powder samples allows us to investigate more specific momentum space we want to know. The main obstacle to performing the RIXS experiments is the intensity with enough energy resolutions to study low energy excitations such as magnetic excitations. The intensity of x-ray scattering experiment signals with polycrystalline sample is smaller than that with the same quantity of single crystal because the orientation of crystals in the polycrystalline sample is randomly distributed. For this reason, we need high quality single crystal samples without defects or disorder.

The next step of sample preparations is to identify the orientation of samples. This step is crucial to studying the dispersive characteristics of the excitations in Brillouin zones. One can reach a particular point in the Brillouin zone by aligning the sample properly. Here I describe the basic principle of the single crystal x-ray diffraction with four circle

diffractometer and explain a way how to align the sample with this tool.

2.1.1 Chemical vapor transport method

The chemical vapor transport (CVT) technique is known as a famous way to get a large sized of single crystal, especially in case of van der Waals (vdW) materials such as TM dichalcogenides and TM phosphorus trichalcogenides [Ref.2.1]. The term of ‘chemical vapor transport’ indicates the multi-step reactions involving several phase transitions of reactants usually from gas to solid or vice versa. However, the proper phase can be obtained with the presence of another reactant, so-called the transport agent, which helps the volatilization and deposition of main reactant. The deposition typically happen in the different place of volatilization when there are distinct external conditions, in my case it is temperature, for pertinent chemical equilibrium of crystallization.

In principle, there can be two practical ways of CVT method in real laboratory with open and closed systems. An open system usually can be applied to quartz or ceramic tubes with both end side opened. The solid state of the source reactants should be kept at a certain position and the transport agent flows continuously over the source. The deposition will take place at the different position with proper external conditions. One can make use of a sealed ampoule in case of a closed CVT system (Figure 2.1). In this situation, the transport agent is kept in the ampoule so much less agent is needed. Most common selection of this method is a sealed quartz tube with the length of 10 to 20 cm and diameter of 1 to 2 cm. Different from the growth condition, one can modulate the pressure inside the quartz tube

by controlling the amount of source reactants and transport agent. This pressure usually differs from 0.5 to 3 bar depending on the target crystals.

There can be several conditions for experimentalists to consider when trying crystal growth with CVT method. First of all, one should be considerable to choose the phase of reactant whether a pure element or polycrystalline crystals, and the suitable transport chemical for the crystal growth. In addition one can also control the several conditions including pressure and temperatures for volatilization of reactant and deposition of crystal. For the selection of these conditions, some general qualitative calculation should be preceded described in Ref.2.1.

Figure 2.1 shows a simple process of the CVT method to synthesize van der Waals NiPS₃ single crystals. Starting materials are mixed in a proper stoichiometric ratio as a powder and placed at the end of the quartz tube. I added solid state of sulfur or iodine as a transport agent to select, which can be easily volatilized at low temperature. Then, these mixed materials are sealed in a quartz ampoule under vacuum pressure lower than 0.01 Torr to prohibit the access of oxygen, and placed into a horizontal 2-zone furnace with a certain temperature difference as shown in the inset graph in Figure 2.1.

After the growth, all samples are immediately subjected to chemical analysis using a COXIE M-30 scanning electron microscope equipped with a Bruker QUANTAX 70 energy dispersive x-ray system to find the 1:1:3 stoichiometry of all the samples used in this thesis.

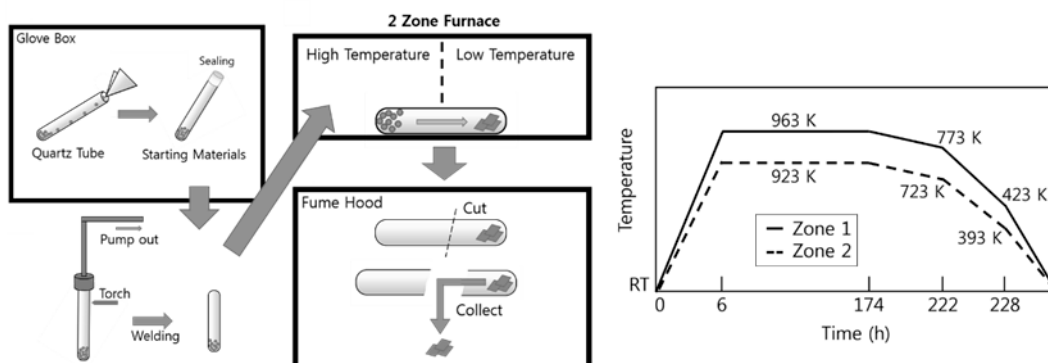


Figure 2.1. Schematic view of the entire process of chemical vapor transport method using two-zone furnace.

2.1.2 Single crystal x-ray diffraction

After the crystal growth by the CVT method, we need to determine the orientation of single crystals. The single crystal x-ray diffraction (SC-XRD) is a useful method to identify the crystal structure and the orientation of single crystal samples. Once a sample is mounted on the sample stage, x-ray beam is irradiated to the crystal. The scattered x-ray photons interfere with each other following the Laue conditions and the constructive interference makes strong signals on the detector. By analyzing the positions and intensities of the peaks, the crystal structure of the sample can be verified. There are several advantages to utilize this technique compared to powder XRD. First, it allows experimentalist to observe larger number of Bragg peaks than possible with the powder XRD diffraction. One can also collect a few thousands of Bragg peaks by SC-XRD while the randomly distributed orientation of polycrystalline sample only allow to measure a much smaller number of

concentric circle signals. There should be always ambiguity by average effects under powder XRD, which makes weak reflections buried in a strong background. Therefore, one can get much more and accurate information about the samples from SC-XRD, which enables to identify small difference in the structures, tiny defects, or distortions on the crystal.

To perform the SC-XRD, I utilized the XtalLAB P200 (Rigaku, Figure 2.2), which is equipped with a four circle diffractometer. The diffractometer has four different motors: three (κ , ω , φ) on the sample state and one on the detector. The x-ray source is molybdenum, which emits 0.7107 Å. Figure 2.3 shows the mounted NiPS₃ single crystal and the analysis result.

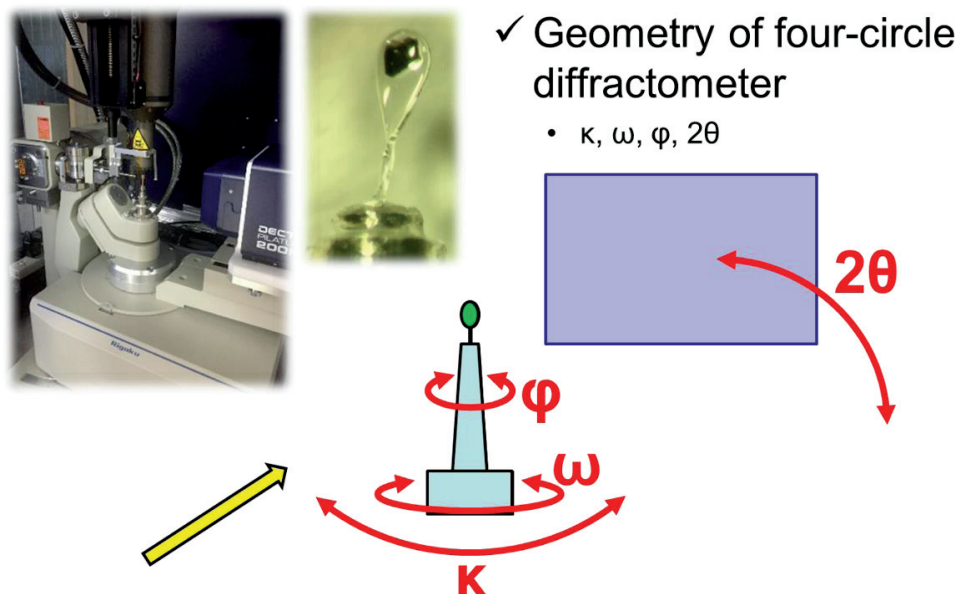


Figure 2.2. Picture of single crystal x-ray diffractometer (XtaLAB P200, Rigaku) and the four motors in this instrument.

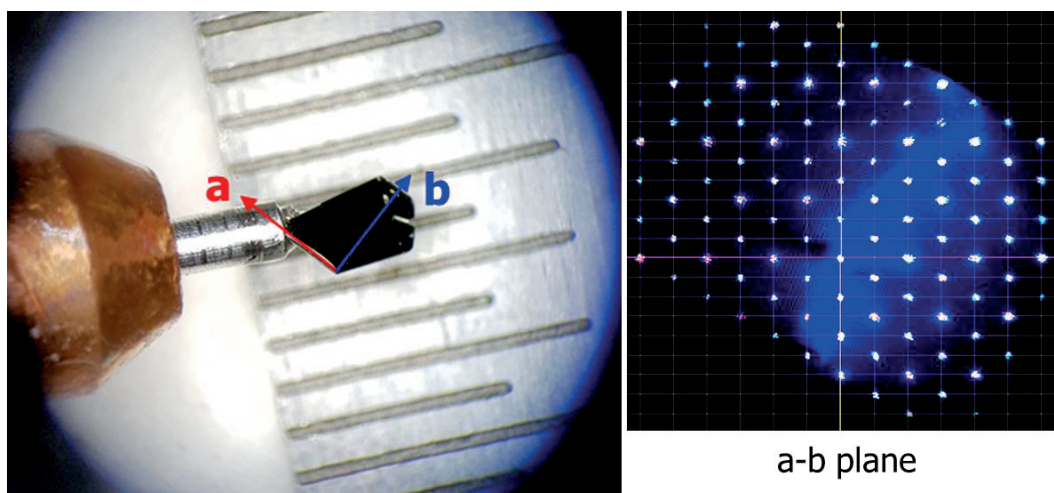


Figure 2.3. Picture of NiPS₃ single crystal mounted on the sample stage and the analysis results from the SC-XRD.

2.2 RIXS experiments in large facilities

RIXS experiments need high incident photon flux to get enough energy resolutions in reasonable time and the energy-tunable x-ray source to tune the incident energy to particular edges for resonance. To satisfy these requirements, we utilize high-brilliance synchrotrons. For my research described in Chapter 3 and 4, I visited two different beamlines: I21 at Diamond Light Source (DLS), UK, and ADDRESS at Paul Scherrer Institut. Following sections introduce the experimental details of the RIXS experiments I performed.

2.2.1 Choice of incident energy

Researchers who perform RIXS experiments should first choose the proper absorption edges, which can provide the physical information of interest. X-ray absorption edges can be classified into several groups such as *K*, *L*, and *M* edges depending on the core level as shown in Figure 2.4. X-rays of *K* edges excite the electrons at $1s$ orbital and *L* edge promotes the electrons from $2s$ or $2p$ orbital. *L* edges can be divided to three detail categories. The core level of L_1 edge corresponds to $2s$, L_2 edge does to $2p_{1/2}$, and L_3 edge does to $2p_{3/2}$. The classification of x-ray absorption edge is crucial for those who perform RIXS experiments since the spectral weights are quite different at different edges. Among the various edges, TM *L* and *K* edges or oxygen *K* edges are most commonly utilized.

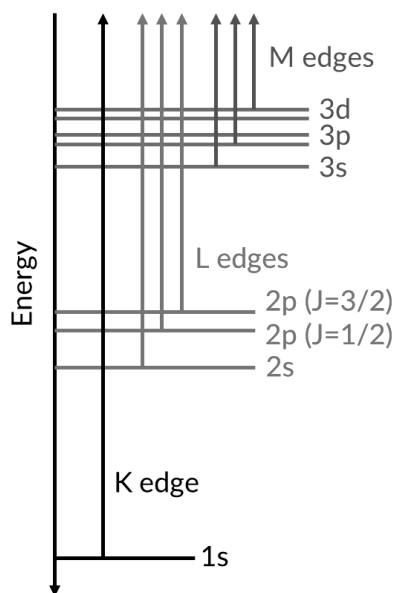


Figure 2.4. Classification of x-ray absorption edges.

Different from K edges, TM L edges have distinct features. The core electrons at $2p$ orbitals are excited to d orbital when the incident beam is tuned to TM L edges. It means that experimentalist can observe d orbitals directly. That is to say, the dipole transitions directly involves the d orbitals. This makes the spectral weights of d - d excitations or other orbital excitations enhanced as compared to K edge RIXS experiments. Another powerful advantage of TM L edges is opportunity to observe excitations related to ‘spin-flip’ processes. A good quantum number of core hole is the total spin angular momentum J ($=L+S$), not S , due to the large spin-orbit coupling of p orbitals. For this reason, the spin angular momentum S does not need to be conserved in the intermediate state. In the intermediate process of RIXS, spin can be flipped or form ‘spin waves’. As a results, one can study ‘single’ magnon excitations or ‘spin-flip’ excitations.

The K edges excite the $1s$ core electron to $4p$ or $5p$ orbitals, which means that the dipolar transition does not involve the d orbitals. The transitions to d orbitals are quadrupolar and their spectral weights are relatively small. Instead, the dipole transitions from $1s$ to $4p$ orbitals shows stronger intensity. Hence, K edge RIXS is a better tool to study the charge-transfer excitations rather than d - d excitations or magnons. Unlike L edges, spin angular momentum S should be conserved during all RIXS process in K edges since there is no spin-orbit coupling for the core hole. Spin-conserving magnetic excitations such as bimagnons are still observable, but single magnon is not. For the TM K edges, they are in the hard x-ray region having larger energy, which makes it possible to investigate a wider range of phase space including both energy and momentum. O K edge can be used as an alternative tool of TM edges when both TM L and K edges are impossible to be accessed

[Ref.2.2]. As TM element often hybridizes with surrounding oxygen in TM oxides, one can still get enough information about charge transfer excitations or $d-d$ excitations.

Choosing an absorption edge is not a final step of confirming the incident energy. Before performing high statistics RIXS scans, in real experiments one needs to get fluorescence XAS spectrum and rough RIXS maps around absorption edges. Since XAS contains the information about the unoccupied valence levels, each energy of XAS peak enhances the different features. At L edges, one often observe a main absorption peak and a satellite peak above the main peak. The main line shows the transition of the metal center itself while the satellite energy emphasizes the charge transfer features. I will show some related results in Chapter 4.

One can also observe several different absorption peaks near K edge. The weak pre-edge peak below the main peak enhances the direct transitions to d orbitals, which is similar to an L edge RIXS. On the other hand, the main peak contains more information about the CT excitations as I described above paragraph.

2.2.2 Single crystal experiment on I21 at DLS

The I21 beamline at the Diamond Light Source (DLS) is a newly constructed second-generation RIXS facility (Figure 2.5). It provides a highly focused (in space) and highly monochromatized (in energy) X-ray beam. The I21 beamline features an energy resolution of about 35 meV (20 meV) at 1 keV (500 eV) being one of the best RIXS instruments. Such high resolution enables the delicate studies of low energy excitations such as magnetism

and spin-orbit physics in aforementioned systems.

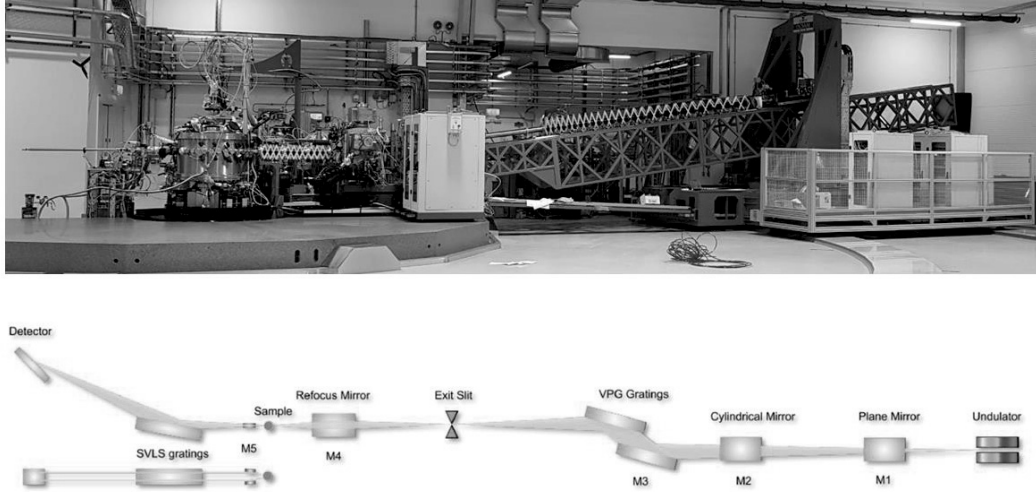


Figure 2.5. Picture of I21 at DLS and the schematic view of beamline from the undulator of synchrotron to detector across five different mirrors, sample and grating [Ref.2.4].

I carried out the Ni L edge RIXS experiments on NiPS₃ single crystal to investigate the unconventional magnetic excitations and related collective excitations. I prepared the single crystal of NiPS₃ whose size is about 1 mm* 0.7 mm by the chemical vapor transport method and direction is verified by SC-XRD (Figure 2.3). The sample has been mounted on the copper sample holder with silver paint and the surface of the sample has been cleaved with Scotch tape to get clean and flat surface.

Since the main question of our study is the collective magnetic excitations and $d-d$ excitations of Ni, the energy of incident beam was chosen to Ni L_3 -edge. The energy

resolution of RIXS in this study is 33.24 /meV, which is enough to investigate the single magnon dispersion from the previous studies [Ref.2.3]. We fixed our detector at 140° , which is the largest value in I21, to explore a wide area in the phase space of NiPS₃. The Q_{\parallel} values along b^* axis change from 0 to 1 by the variation of θ , which is the angle between the incident beam and the sample surface. To confirm the origins of each peak, the temperature of the sample was changed from 14 to 300 K.

2.2.3 Thin film experiment on ADDRESS – X03MA at PSI

ADvanced **RE**Sonant Spectroscopies (ADDRESS) is a RIXS beamline installed in the Swiss Light Source (SLS) at the Paul Scherrer Institut (PSI). It provides a soft x-ray radiation whose energy range is from 300 to 1800 eV and high resolution of 70 meV at 1 keV [Ref.2.5]. It utilizes the collimated-light PGM optical scheme (Figure 2.6). The figure 2.7 shows the high photon flux at the 0-180° variable linear polarizations, which enables the thin film experiment as a function of polarization.

I carried out O *K* edge RIXS at the ADDRESS [Ref.2.5, 6] on the SrRuO₃ thin films. The energy of the ruthenium *L* edge (~ 3 keV), however, just happens to be situated in between soft and hard x-ray regimes. For this technical reason, it is not easy to get enough photon flux and energy resolution at the Ru *L* edge, which makes it experimentally challenging to do RIXS at the Ru *L* edge. Instead, I carried out our experiment at the oxygen *K* edge to study the charge dynamics of the Ru *4d* orbitals while varying the thickness of thin-film samples.

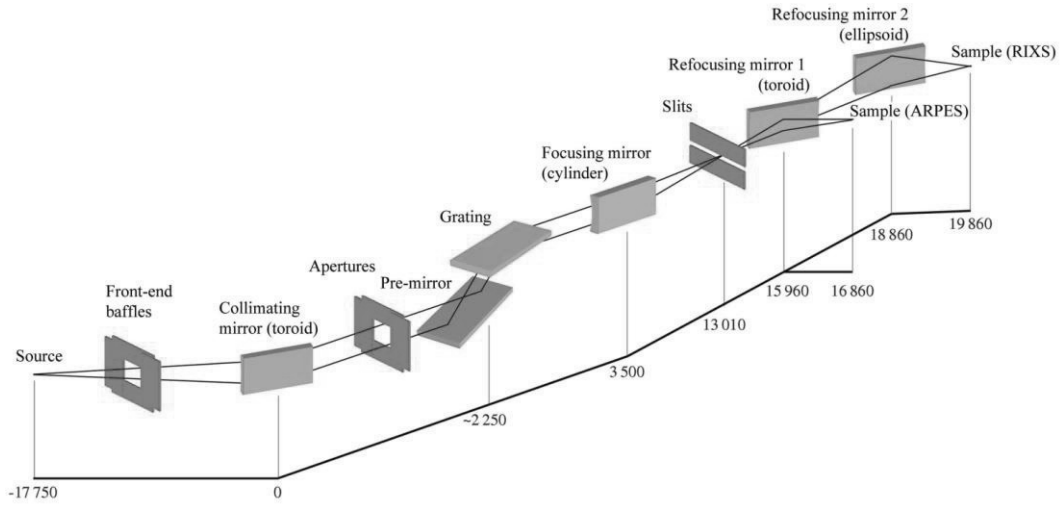


Figure 2.6. Schematic view of ADDRESS [Ref.2.5]

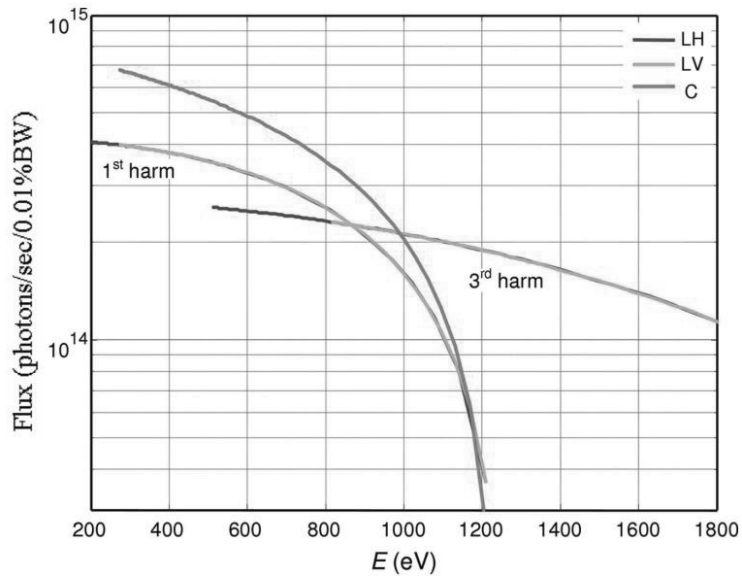


Figure 2.7. The photon flux with different polarizations: Linear horizontal (LH), linear vertical (LV) and circular (C) polarizations.

The energy resolution is less than 70 meV by checking the full width at half maximum of the elastic line from diffuse scattering at a carbon tape reference. All our samples were aligned with a grazing angle ($\theta = 15^\circ$) to increase the scattering cross-section especially for ultrathin samples. The scattering angle from the incident beam to the detector was fixed to 130° , with a corresponding momentum transfer of q_{\parallel} . We employed two different polarizations for our experiments: linearly vertical (σ) polarization is parallel to the sample plane, and linearly horizontal (π) polarization is nearly perpendicular to the plane. Thus, the former is more sensitive to the p_x (p_y) orbital, while the latter is more sensitive to the p_z orbital due to the incident angle. All experiments were performed at 20 K.

References

- [Ref.2.1] P. Schmidt, M. Binnewies, R. Glaum, and M. Schmidt, *Chemical Vapor Transport Reactions-Methods, Materials, Modeling*, (IntechOpen, London, 2013).
- [Ref.2.2] S. Kang, Y. Tseng, B. H. Kim, S. Yun, B. Sohn, B. Kim, D. McNally, E. Paris, C. H. Kim, C. Kim, T. W. Noh, S. Ishihara, T. Schmitt, and J.-G. Park, *Phys. Rev. B* **99**, 045113 (2019).
- [Ref.2.3] D. Lançon, R. A. Ewings, T. Guidi, F. Formisano, and A. R. Wildes, *Phys. Rev. B* **98**, 134414 (2018).
- [Ref.2.4] Website of Diamond Light Source, <https://www.diamond.ac.uk/>
- [Ref.2.5] V. N. Strocov, T. Schmitt, U. Flechsig, T. Schmidt, A. Imhof, Q. Chen, J. Raabe, R. Betemps, D. Zimoch, J. Krempasky, X. Wang, M. Grioni, A. Piazzalunga, and L. Patthey,

J. Synchrotron Radiat. **17**, 631 (2010).

[Ref.2.6] G. Ghiringhelli, A. Piazzalunga, C. Dallera, G. Trezzi, L. Braicovich, T. Schmitt, V. N. Strocov, R. Betemps, L. Patthey, X. Wang, and M. Grioni, Rev. Sci. Instrum. **77**, 113108 (2006).

Chapter 3

Exotic magnetic excitations in van der Waals antiferromagnet NiPS₃

3.1 Magnetism in two-dimensional van der Waals materials

Two-dimensional (2D) magnetism has played a very significant and special role in advancing our fundamental understanding of magnetism [Ref.3.1-3.6] and the advance in state-of-the-art technology [Ref.3.7]. The discovery of graphene using mechanical exfoliation with adhesive tape [Ref.3.8] rapidly enlarges the field of so-called van der Waals (vdW) material, which has a layered structure and a relatively weak vdW interaction between the layers. This revolution of vdW materials also opens up another opportunity of 2D magnetism, so-called vdW magnetic materials [Ref.3.9, 3.10]. In this section, I introduce the theories on 2D magnetism and the exotic phases of vdW magnetic materials.

3.1.1 Fundamental theories on 2D magnetism

A field of magnetism has been studied nearly three thousand years since Greek scholars found a lodestone [Ref.3.11]. However, the systematic investigation of magnetism in condensed matter started in 19th century by P. Curie, M. Curie, and P. Weiss. In addition,

the modern understanding of magnetism with the theoretical explanation about the electrons started in 20th century only after the advent of quantum mechanical models by E. Ising [Ref.3.12] and W. Heisenberg [Ref.3.13]. The early theories have successfully described the interaction between the spins in condensed matter and even been used until now. For example, the Heisenberg model is a fundamental model of long-range magnetic orderings such as ferromagnetic or antiferromagnetic ordering, which can be described as

$$H = J \sum_{\langle ij \rangle}^N \mathbf{S}_i \cdot \mathbf{S}_j,$$

where J is an exchange constant and \mathbf{S}_i is a spin at site i . It gives a clear and accurate description of magnetism in traditional bulk samples whose interactions are in three dimension. However, when it comes to 2D limits. 2D magnetism shows quite distinct behavior from the traditional 3D magnetic ordering because the effects of spin fluctuations get enhanced [Ref.3.4]. The strengthened spin fluctuations make the symmetry-broken ordering unsustainable, which disturb the long-range ordering. There are several well-established theories for 2D systems such as the Mermin–Wagner theorem for two dimension[Ref.3.3], the Onsager solution for Ising-type magnetic ordering [Ref.3.4], and Berezinskii–Kosterlitz–Thouless (BKT) transition in the XY model [Ref.3.1, 3.2].

Mermin-Wagner theorem describes how the variation of dimension affect to the long-range magnetic ordering in the solids. The theorem is stated in Ref.3.3. **“The one- and two-dimensional isotropic Heisenberg models with interactions of finite range can be neither ferromagnetic nor antiferromagnetic at non zero temperature.”** According to this statement, there cannot be traditional long-range magnetic ordering whose origin is the

broken continuous rotational symmetry and the short-range interaction. This theorem can also be understood as the excitations of spin waves prohibit the magnetic order.

For example, in the isotropic ferromagnetic case, the dispersion relation for the spin waves can be calculated using the Hamiltonian for the Heisenberg model, which describe as

$$\hbar\omega = 4JS[1 - \cos(qa)],$$

where q is the wave vector and a is the distance between spins. If we think of small q ,

$$\hbar\omega \approx 2JSq^2a^2,$$

so that $\omega \sim q^2$. The magnon DOS, $N(E)$, over the d -dimensional q space is written as

$$N(E) \sim E^{(d-2)/2},$$

since the volume element is proportional to $k^{d-1}dk$. Thus the magnon DOS is constant in two dimension. On the other hand, the number of magnon modes excited at temperature T , n_{mag} , can be calculated by integrating the magnon DOS over all frequencies after multiplying the Bose factor [Ref.3.11] because magnons are bosons:

$$n_{\text{mag}} = \int_0^\infty \frac{N(E)}{e^{E/k_B T} - 1} dE .$$

When the $N(E)$ is constant like 2D ferromagnet, this integral diverges logarithmically. This implies that the magnetization becomes zero at any finite temperature, which means the breakdown of magnetic order. From the calculation, we can know that magnetic order for isotropic Heisenberg model cannot survive because spin waves are easy to be excited infinitely at finite temperature. It is easy to misinterpret this theorem as any magnetic ordering cannot exist in two dimension. However, we need to focus on two important assumption: the ‘isotropic’ and ‘finite-range’ interactions.

For example, if there is an easy axis or single-ion anisotropy in the system, the magnon dispersion should be expressed in different way such as

$$\hbar\omega = A + Bq^2,$$

where $A (> 0)$ and B are constant. In this case, the number of magnons does not diverge at finite temperature since the integral has a lower boundary. If we think of long-range interactions such as dipolar interaction, the magnon dispersion should be changed again such as

$$\hbar\omega = q^{1/2}.$$

In this case, the integral for magnon numbers does not diverge like the anisotropic case either because the magnon DOS is now proportional to ω^3 . Thus, the magnetic ordering in two dimension can be stabilized by the anisotropy or long-range interaction, which makes a gap at the low-energy modes.

From the more generalized form of Heisenberg-type Hamiltonian,

$$H = \sum_{\langle ij \rangle}^N J_{ij} (\alpha S_i^x S_j^x + \alpha S_i^y S_j^y + \gamma S_i^z S_j^z),$$

there exist three famous magnetic orderings known as 2D Ising-type, XY-type, and Heisenberg-type (Figure 3.1). When the magnitude of γ is much larger than that of α , the magnetic ordering can be of 2D Ising-type as established by L. Onsager [Ref.3.4]. The Ising-type Hamiltonian only allow the spins in the lattice to flip, which means they only have DOF in one direction.

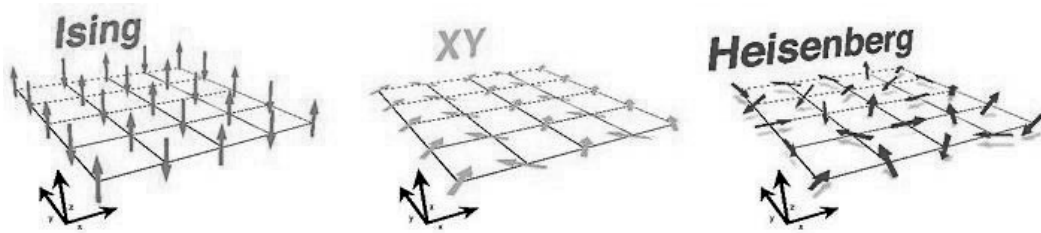


Figure 3.1. The schematic view of three different types of magnetic ordering in 2D limits. The left shows the Ising type that has only 1D DOF, the middle model corresponds to XY-type, and the right one does to Heisenberg-type [Ref.3.10].

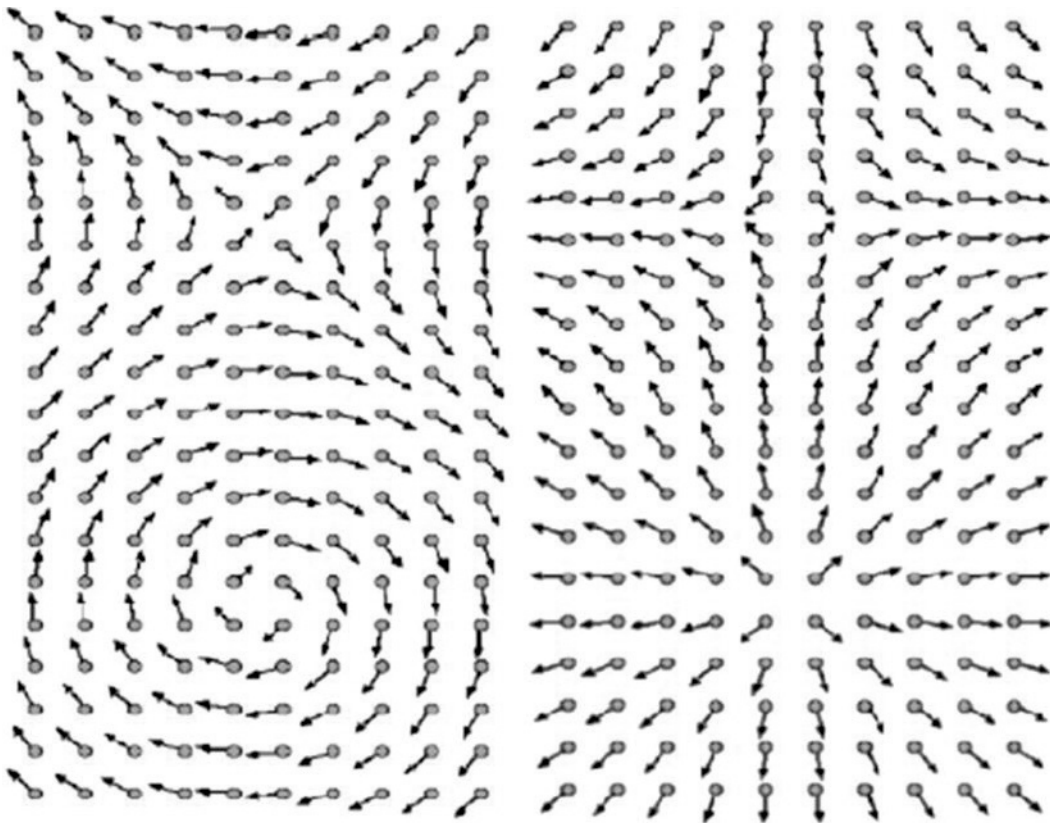


Figure 3.2. The schematic view of vortex-antivortex pairs in the lattice [Ref.3.15].

In the other limit of $\alpha \gg \gamma$, the magnetic moments have DOF in two directions, which is called XY-type interaction. One of famous examples having XY-type interaction is the BKT transition [Ref.3.1, 3.2], which introduce a new class of topological order. The topological order is related to the vortex-antivortex pairs defined by the opposite winding numbers [Ref.3.15]. The vortex and the antivortex should be formed in the lattice simultaneously, and stabilize the locally ordered states such as a magnetic skyrmion [Ref.3.16].

3.1.2 Magnetic van der Waals materials

Although the fundamental understanding of 2D magnetism is quite well-established as I described in the previous sessions, the experimental observations have not been realized until quite recently. The main obstacle of this finding proper materials, which one can use to produce a clean magnetic monolayer. The discoveries of magnetic vdW materials such as TM dichalcogenides [Ref.3.17-3.20] and TM phosphorus trisulfides (TMPS₃; TM = 3d transition metals) [Ref.3.21-3.24] open a window of new opportunities to investigate the fundamental theories of 2D magnetism, which is induced by the strongly enhanced spin fluctuations. The spin fluctuation itself can be an important subject that has an opportunity of new quantum phases, such as the suppression of topological order.

In addition to the fundamental issues of 2D magnetism, the novel phenomena and the application to the industries is another attractive aspect of magnetic vdW materials (Figure 3.3). One of the advantages to use vdW materials is the demonstration of new system by stacking the distinct materials. Different from the film growth, vdW materials do not

require the so-called lattice matching for fabrication of the heterostructures. Thus the choice of material and method, such as angle, to make heterostructures is much wider than in any other materials. For example, the recently found moiré pattern [Ref.3.25] can be obtained only with the vdW materials. The unique feature of heterostructures with vdW materials enables the spin DOF in one material to couple with the external perturbations from other materials beyond the internal coupling. This would also make possible the emergence of novel quantum phenomena such as quantum spin liquids, unconventional superconductivity in two dimensions, fractionalization of quasi-particles, and quantum spin Hall effects.

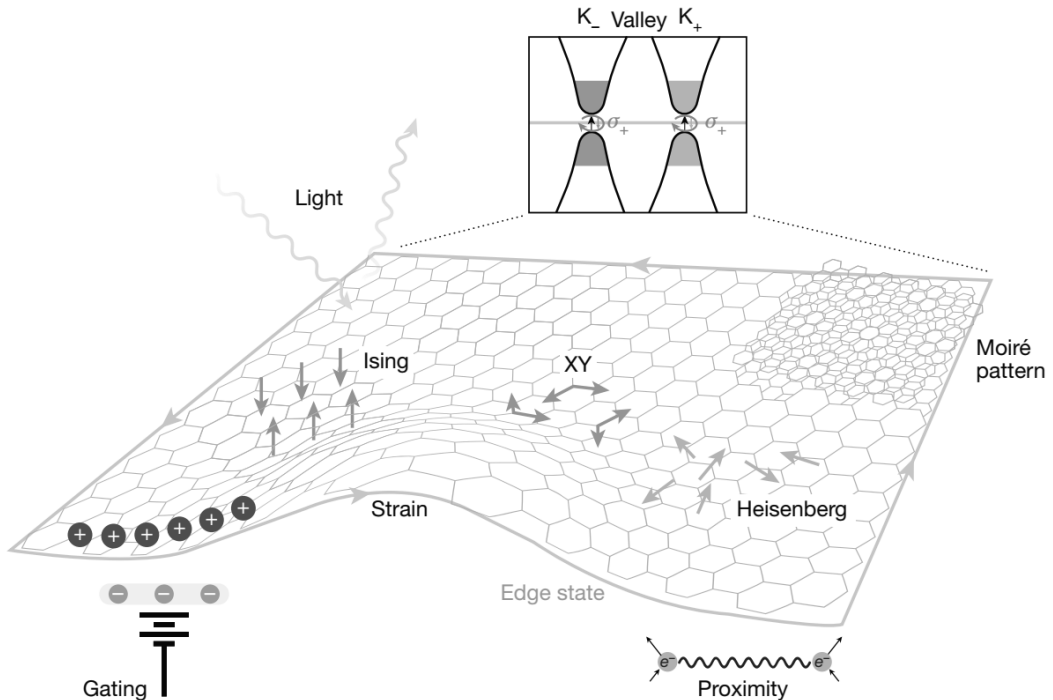


Figure 3.3. Possible physical issues and phases in magnetic vdW materials [Ref.3.10].

3.2 Magnetic structure of NiPS₃

NiPS₃ has a layered structure with Ni²⁺ ions forming a honeycomb lattice in ab plane and each layer interacts with vdW forces. It belongs to a new class of 2D antiferromagnets TMPS₃ whose members have an isostructural monoclinic C2/m space group but different type of magnetism depending on the TM. For instance, the magnetic interactions in FePS₃ is explained by Ising-type Hamiltonian while MnPS₃ has a Heisenberg-type antiferromagnetic ordering [Ref.3.21, 3.26]. It is verified that XXZ-type model Hamiltonian explains correctly the magnetic structure of NiPS₃ by the optical Raman spectroscopy [Ref.3.24] and the inelastic neutron scattering [Ref.3.27]. The first nearest-neighbor exchange parameter has a positive value (ferromagnetic) and the third nearest-neighbor exchange is large but antiferromagnetic. These exchange values construct a zigzag spin ordering as shown in Figure 3.4.

In addition to its unique 2D magnetism, a self-doped hole due to a small charge transfer (CT) in NiPS₃ is another interesting aspect (Table 3.1). The energy needed to transfer an electron from Ni ions to S ions is small enough to stabilize the self-doped ground state. This makes complex ground states (Figure 3.8) and unusual Ni-S singlet states (Figure 3.10). The exotic singlet states can be localized due to the strong spin-charge coupling in NiPS₃.

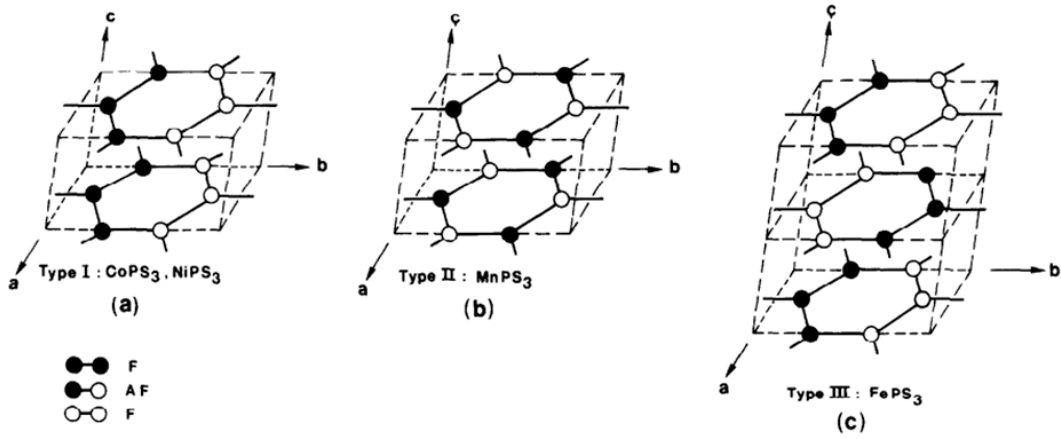


Figure 3.4. The different types of antiferromagnetic ordering in TMPS_3 materials. (a) XY-type model of NiPS_3 and CoPS_3 , (b) Heisenberg-type model of MnPS_3 , and (c) Ising-type model of FePS_3 [Ref.3.26].

3.3 $\text{Ni } L_3$ edge RIXS on NiPS_3 single crystal

In the following sections, I present the result of $\text{Ni } L_3$ edge RIXS, and discuss about the magnon dispersion and the collective excitations related to spin-charge coupling. First, I introduce the configuration interaction calculation and the multiplet structure with different symmetries. Using these results, the strong spin-charge coupling will be investigated via XAS and RIXS spectra. In addition, the spin dynamics confirms the proposed XXZ-type model Hamiltonian from the low-energy spectrum of high-resolution RIXS experiment on several different temperatures across the transition temperature.

3.3.1 Result: XAS and overall RIXS spectra

The fluorescence XAS experiments provide the abundant information about the valence states and help to choose a proper incident energy for RIXS. Especially, for the NiPS₃ case, the investigation of valence levels is rather significant because it has an issue of negative charge transfer [Ref.3.28]. We found two main absorption peaks in our XAS data taken around Ni L_3 edge as shown in Figure 3.5. The strongest on-resonance peak emerges at 857.2 eV and a satellite peak exists at 858.1 eV, which seems like a shoulder of the first peak. Each absorption with different energy implies the different ground and excitation states according to the valence state and orbital configuration of Ni ions. In general, the on-resonance absorption line mainly probes the transition related to the metal center while the CT features are emphasized in a slightly higher energy region [Ref.3.29]. For instance, the first absorption peak predominantly originates from a Ni d^8 configuration to the unoccupied valence state with a $d^9\bar{c}$ electronic configuration, where \bar{c} denotes a core hole. On the other hand, the satellite peak at 858.1 eV emerges due to the excitation from $d^9\bar{L}^1$ to $d^{10}\bar{c}^1\bar{L}^1$ states, where \bar{L} indicates a hole in the ligand (sulfur). We confirmed the origins of absorption peaks from the configuration interaction (CI) calculations with a NiS₆ cluster model (see the multiplet structure in Section 3.3.2). The results of XAS with a main absorption peak and three satellite peaks agree with the previous study [Ref.3.28], which predicted originally the negative CT. Synthetically considering both XAS and RIXS results with CI calculations, however we concluded that CT value may not be negative unlike the earlier expectation. Although the CT energy is not negative but positive value, it

is small enough to make a $d^9\bar{L}$ ground state stable.

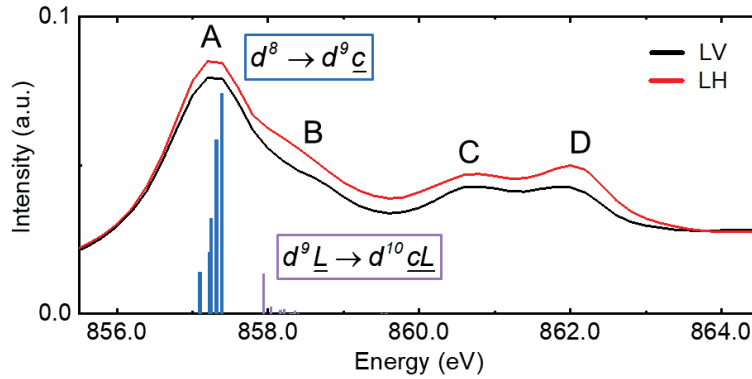


Figure 3.5. The results of fluorescence XAS of NiPS₃ near Ni L_3 edge at 14 K. The black and red lines show the experimental results with linear vertical and horizontal polarizations. The blue and purple bar graphs demonstrate the distinct multiplet ground states calculated by configuration interaction calculations with a NiS₆ cluster. The main absorption peak A is located at 857.3 eV, and there are several satellite peaks above the main line. Among the satellite peaks, the first satellite peak B at 858.1 eV originates from the $d^9\bar{L}^1$ ground states.

A RIXS map depending on the incident energy of NiPS₃ at 14 K is displayed in Figure 3.6. The presence of constant energy loss d-d excitations extended from 1 to 2 eV indicates the localized character of the Ni 3d states. Another remarkable feature of the energy-detune map is that a sharp peak emerges at the energy loss of 1.45 eV especially when the incident energy is tuned to 858.1 eV. This incident energy corresponds to the satellite absorption line whose multiplet ground states predominantly have a $d^9\bar{L}^1$ configuration. This implies that the RIXS spectra at 858.1 eV involves the enhanced CT feature as expected. That is to

say, a sharp peak at 1.45 eV contains a noteworthy information about CT.

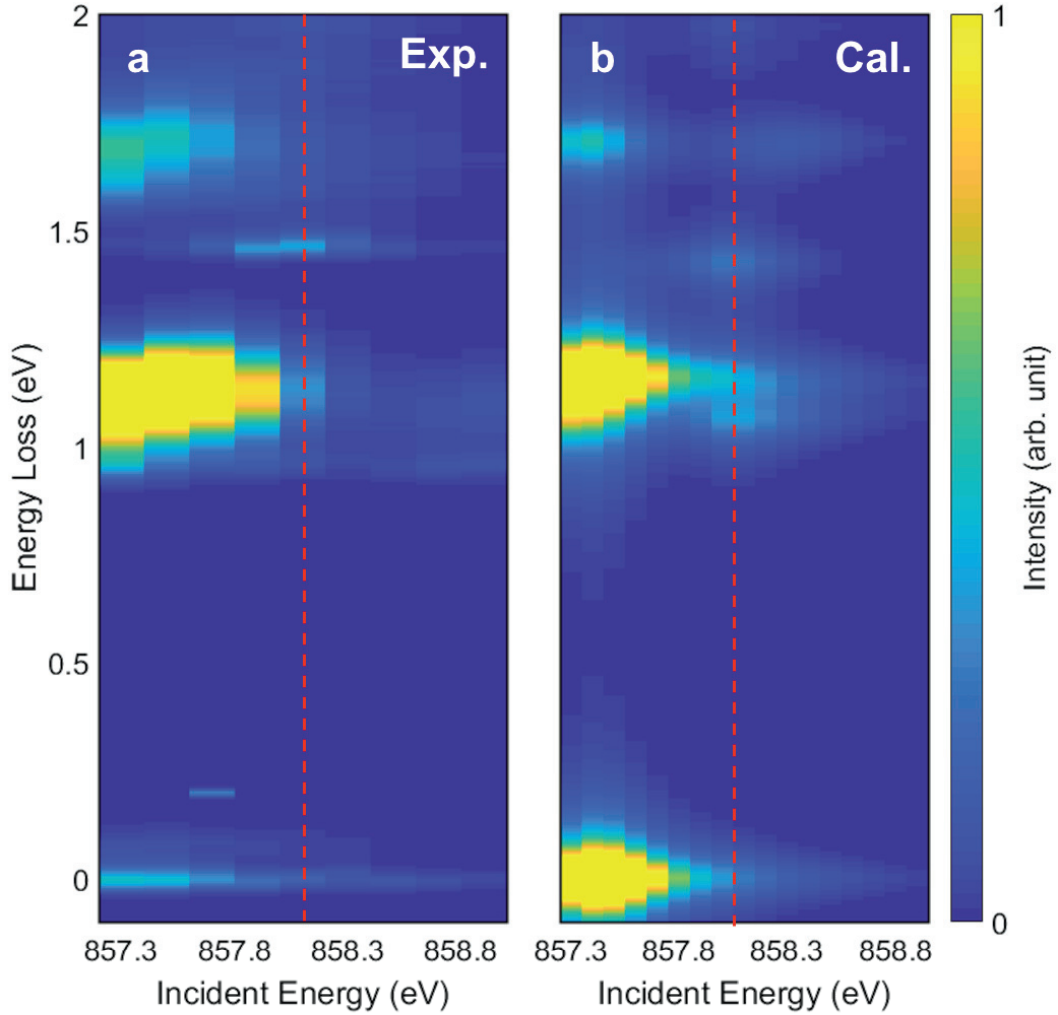


Figure 3.6. (a) The experimental results and (b) theoretical description of RIXS maps as a function of incident energy containing a main absorption and a satellite peak region. The red dashed lines on both maps indicate the energy where the sharp peak

at 1.45 eV has the strongest intensity, and the energy corresponds to the satellite peak in XAS.

10Dq	λ_d	F_{dd}^0	F_{dd}^2	F_{dd}^4	λ_c	F_{pd}^2	G_{pd}^1
1	0.08	8	14.68092	9.11772	11.5	6.1773	4.6304
G_{pd}^2	Δ	Δ'	U_p	J_p	$V_{pd\sigma}$	$V_{pd\pi}$	
2.6334	0.95	-0.55	1	0	-0.74	0.4	

Table 3.1. Physical parameters for the CI calculation in units of eV.

3.3.2 Discussion 1: Configuration interaction calculations

We performed the CI calculations of both NiS₆ and Ni₂S₁₀ clusters for microscopic understanding of Ni L_3 edge RIXS spectra. The clusters are assumed to have open boundary as shown in Figure 3.7. The Hamiltonian we employed in this study can be written as

$$H = H_d + H_c + H_{dc} + H_L + H_t$$

, where H_d , H_c , and H_L represent Hamiltonians describing the local energies of Ni $3d$ valence, Ni $2p$ core, and S $3p$ ligand orbitals, respectively [Ref.3.30]. H_{dc} refers to the Coulomb interaction between Ni $3d$ valence and Ni $2p$ core orbitals. H_t is the hopping Hamiltonian between Ni $3d$ valence and S $3p$ ligand orbitals.

H_d is composed of the cubic crystal field $10Dq$, the spin-orbit coupling (SOC) λ_d , and the Coulomb interaction among Ni $3d$ orbitals. The first three terms ($F_{dd}^0, F_{dd}^2, F_{dd}^4$) survive in Slater-Condon parameters used to calculate the Coulomb interaction. When we consider H_c , each Ni $2p$ core level is separated by a spin-orbit coupling λ_c . The SOC of

ligand is neglected and the Kanamori-type Coulomb interaction is applied among ligand orbitals. In the process we express the Coulomb interaction between Ni 3*d* valence and S 3*p* ligand orbitals, there are four Slater-Condon parameters nonzero elements ($F_{pd}^0, F_{pd}^2, G_{pd}^1, G_{pd}^2$).

We manipulated two CT energies Δ and Δ' in the absorption process, where Δ indicates the strength of CT from d^8 to $d^9\underline{L}^1$ and Δ' involves CT from $d^9\underline{c}^1$ to $d^{10}\underline{c}^1\underline{L}^1$. Note that the difference of these two CT corresponds to the difference of U_{pd} and U_{dd} . Our selection of the parameters used in H are presented in table 3.1. The value of F_{pd}^0 parameter has been determined as $\Delta - \Delta'$ is known to be about -1 to -2 eV [Ref.3.31].

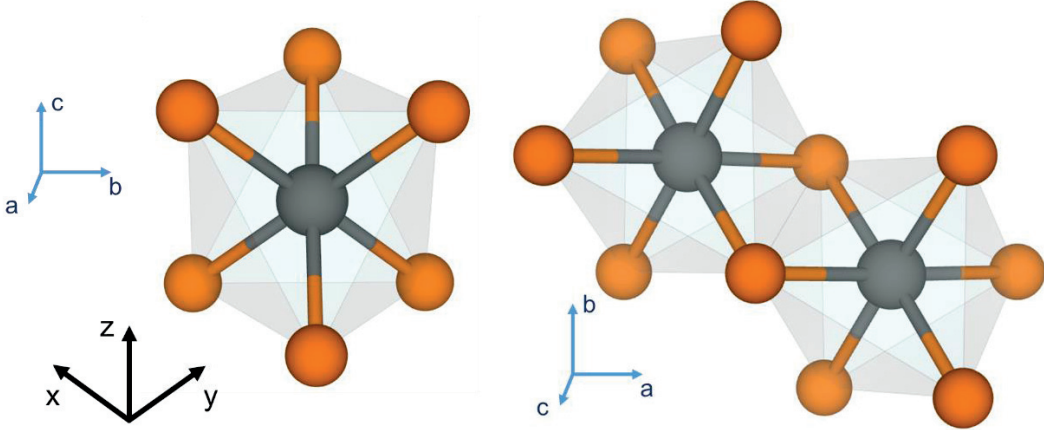


Figure 3.7. Schematic diagrams of NiS₆ and Ni₂S₁₀ clusters with open boundary

condition. x, y, z (marked as black arrows) are the local coordinates of NiS₆ octahedron

where a, b, c (marked as blue arrows) are global coordinates of lattice. $\hat{x} = \sqrt{\frac{1}{6}}\hat{a} -$

$$\sqrt{\frac{1}{2}}\hat{b} + \sqrt{\frac{1}{3}}\hat{c}, \hat{y} = \sqrt{\frac{1}{6}}\hat{a} + \sqrt{\frac{1}{2}}\hat{b} + \sqrt{\frac{1}{3}}\hat{c}, \text{ and } \hat{z} = -\sqrt{\frac{2}{3}}\hat{a} + \sqrt{\frac{1}{3}}\hat{c}.$$

As the Ni L_3 edge RIXS observe the direct dipolar transitions, the XAS intensity I_{XAS} is described as

$$I_{XAS} = -\frac{1}{n_d\pi} \text{Im} \sum_{ia} \langle \Psi_g | \hat{e}_\xi \cdot \mathbf{D}_i^\dagger \frac{1}{\omega_{in} - H + E_g + i\delta_{in}} \hat{e}_\xi \cdot \mathbf{D}_i | \Psi_g \rangle,$$

where n_d is the number of Ni sites, ω_{in} and δ_{in} are incident energy and broadening, and \hat{e}_ξ is the unit vector of $\xi (= a, b, c)$ coordinate axis. \mathbf{D}_i is the dipole operator given as

$$\mathbf{D}_i = \sum_{\mu m \sigma} \langle \psi_\mu^d | \mathbf{r} | \psi_m^c \rangle d_{i\mu\sigma}^\dagger c_{im\sigma},$$

where ψ_μ^d and ψ_m^c are wave functions of Ni $3d$ orbital μ and Ni $2p$ orbital m , respectively. The XAS calculation results are in Figure 3.5.

Utilizing the Kramers-Heisenberg formula [Ref.3.32], the RIXS intensity is given as

$$I_{RIXS} = -\frac{1}{n_d\pi} \text{Im} \sum_i \langle \Psi(\omega_{in}, \mathbf{q}, \epsilon, \epsilon') | \frac{1}{\omega - H + E_g + i\delta_b} | \Psi(\omega_{in}, \mathbf{q}, \epsilon, \epsilon') \rangle,$$

where $\omega = \omega_{in} - \omega_{out}$ and $\mathbf{q} = \mathbf{k} - \mathbf{k}'$ when an incident (outgoing) x-ray has energy ω_{in} (ω_{out}), momentum \mathbf{k} (\mathbf{k}'), and polarization ϵ (ϵ'). The dipolar transition is involved in $|\Psi(\omega_{in}, \mathbf{q}, \epsilon, \epsilon')\rangle$ described as

$$|\Psi(\omega_{in}, \mathbf{q}, \epsilon, \epsilon')\rangle = \sum_j e^{i\mathbf{q}\cdot\mathbf{r}_j} \mathbf{D}_j^\dagger \frac{1}{\omega_{in} - H + E_g + i\delta_{in}} \hat{e}_\xi \cdot \mathbf{D}_j | \Psi_g \rangle,$$

where \mathbf{r}_j is the position of j -th Ni site. Figure 3.6. includes the theoretical demonstration of RIXS using these relations.

3.3.3 Discussion 2: Multiplet structure of NiS₆

The close investigation of the multiplet structure gives a significant information for understanding of the feature of each peak presented in XAS and RIXS spectra. Figure 3.8 shows the Tanabe-Sugano diagram as a function of hopping strengths between Ni 3*d* and S 3*p* orbitals ($V_{pd\sigma}$ and $V_{pd\pi}$) when $\lambda_d = 0$ eV and Ni 2*p* core are ignored. The other remaining parameters used for the CI calculations of XAS and RIXS are shown in Table 3.1. When the hopping strength is zero ($r = 0$), a d^8 multiplet structure is composed of several states such as ${}^3A_{2g}(F)$, ${}^3T_{2g}(F)$, ${}^3T_{1g}(F)$, ${}^1E_g(D)$, ${}^1T_{2g}(D)$, ${}^3T_{1g}(P)$, ${}^1A_{1g}(G)$, ${}^1T_{1g}(G)$, ${}^1E_g(G)$, and ${}^1T_{2g}(D)$ in the cubic crystal field consistently with previous literatures [Ref.3.33]. When the hopping strengths get increased from $V_{pd\sigma} = V_{pd\pi} = 0$ to $V_{pd\sigma} = -0.74$ and $V_{pd\pi} = -0.4$ eV ($r = 1$), d^8 and $d^9\bar{L}$ multiplet states tend to be mixed with each other. For example, the ground states with ${}^3A_{2g}(F)$ symmetry are coupled with $t_{2g}^6 e_g^3 \bar{L}^1$ multiplets via the $pd\sigma$ bonding. Its partial contribution of $d^9\bar{L}^1$ states changes from 0 to 41%. Multiplet states with the symmetry such as ${}^3T_{2g}(F)$ composed of $t_{2g}^5 e_g^3$ electronic configuration can overlap with $t_{2g}^6 e_g^3 \bar{L}^1$ multiplet states forming the $pd\pi$ -type bonding.

Because the multiplet states are constituted of such bonding states, it is difficult to define each peak with the traditional categories of the elementary excitations such as CT or $d-d$ excitations. Each peak would be rather classified based on the symmetry of excited states. A noteworthy example is the bonding state of ${}^1A_{1g}(G)$ and $t_{2g}^6 e_g^3 \bar{L}^1$, which is a singlet state with ${}^1A_{1g}$ symmetry.

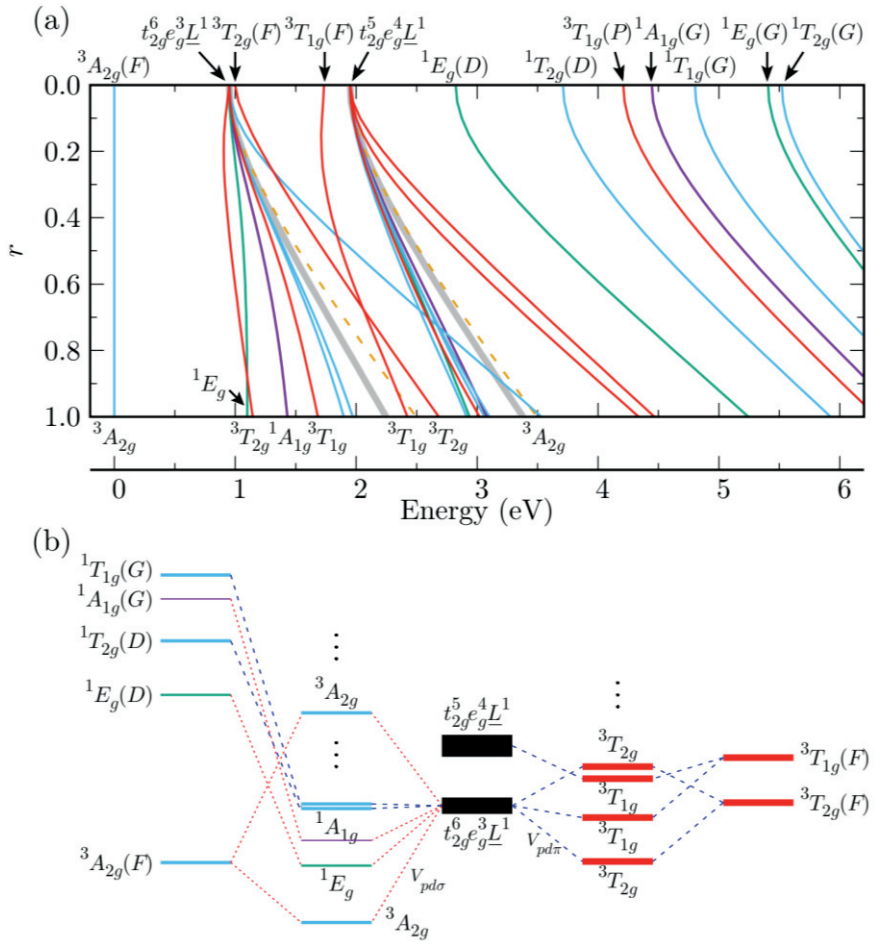


Figure 3.8 (a) The Tanabe-Sugano diagram of NiS₆ cluster as a function of hopping strengths between Ni 3d valence and S 3p ligand orbitals. r is the scale parameter of hopping strengths like $V_{pd\sigma} = -0.74 \times r$ and $V_{pd\pi} = 0.4 \times r$ eV. Each line shows different states with distinct symmetry whose irreducible representation is marked, respectively. (b) Schematic diagram of bonding nature between two multiplet states with d^8 and d^9L^1 electronic configuration. The black thick bars indicate the multiplet states with d^9L^1 . The left and right side represent the $pd\sigma$ - and $pd\pi$ -type bonding between d^8 and d^9L^1 multiplets.

The XAS spectrum involves only one simple transition from Ni 3*p* core to empty valence levels, and it provides rich information of the valence levels where the core electron is excited to. Thus the peak positions on XAS spectra are highly dependent on the multiplet structure of states with $d^9\underline{c}^1$ and $d^{10}\underline{c}^1\underline{L}^1$ electronic configurations, which can be the induced final state from d^8 and $d^9\underline{L}^1$ ground state, respectively. Figure 3.9 presents their multiplet structures when $\lambda_d = 0$ eV. The middle column in Figure 3.9 demonstrates the final state with $V_{pd\sigma} = -0.74$ and $V_{pd\pi} = -0.4$ eV ($r = 1$), which correspond to the proper values necessary to explain the RIXS experiment results as shown in Figure 3.6 and 3.8. Because nonbonding states with $d^{10}\underline{c}^1\underline{L}^1$ configuration are located near 1.5 eV, the multiplet states dominated by the state with $d^{10}\underline{c}^1\underline{L}^1$ are spread from 0.8 to 1.3 eV. However, the $d^9\underline{c}^1$ -prominent states are distributed widely from 0 to 0.3 eV or from 2.5 to 3 eV. Above 3.0 eV, the contribution of $d^{10}\underline{c}^1\underline{L}^1$ states gets reduced less than 20%. Labels ‘A’, ‘B’, ‘C’, and ‘D’ in Figure 3.5 are the peak positions of the theoretical XAS spectra.

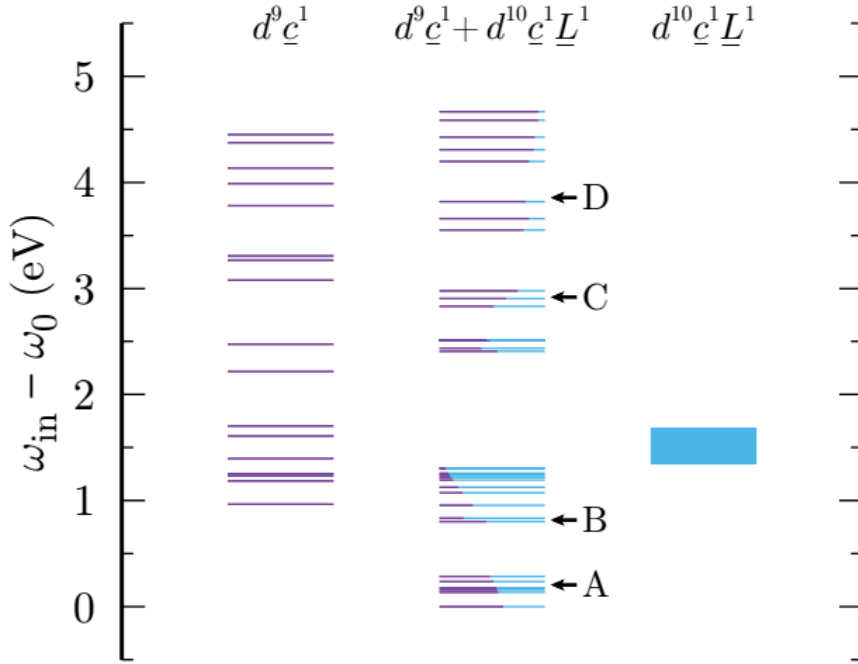


Figure 3.9. Energy splitting of $d^9 \underline{c}^1$ and $d^{10} \underline{c}^1 \underline{L}^1$ multiplets depicted with respect to the difference between the incident energy (ω_{in}) and the ground energy of final state (ω_0). The second column manifests the energy splitting of multiplet states with the combined electronic configurations of $d^9 \underline{c}^1$ and $d^{10} \underline{c}^1 \underline{L}^1$ when $V_{pd\sigma} = -0.74$ and $V_{pd\pi} = 0.4$ eV ($r = 1$). Whereas, the first and third columns shows those for $d^9 \underline{c}^1$ and $d^{10} \underline{c}^1 \underline{L}^1$ configurations, respectively, without the hopping strength. Widths of magenta and cyan parts of lines at second column represent partial contributions of $d^9 \underline{c}^1$ and $d^{10} \underline{c}^1 \underline{L}^1$ on the multiplet states, respectively. The black arrows marked with ‘A’, ‘B’, ‘C’, and ‘D’ indicate the peak positions of theoretical XAS spectra.

3.3.4 Discussion 3: Spin-charge coupling

The CT energy Δ is estimated to be about 0.95 eV in NiPS₃ from the CI calculation, which fully explains the experimental XAS and RIXS results. Although the value is not negative as originally proposed [Ref.3.28], it is small enough that the S 3*p* ligand holes can be self-doped in the ground state. The ground multiplet states with the ${}^3A_{2g}(F)$ symmetry of the NiS₆ cluster are contributed to not only the d^8 states but also the $d^9\bar{L}^1$ states. The self-doped state, which constitute 41% of the ground state, are spin triplet states between the holes on Ni 3*d* and S 3*p* orbitals, so-called Zhang-Rice triplet (ZRT) states.

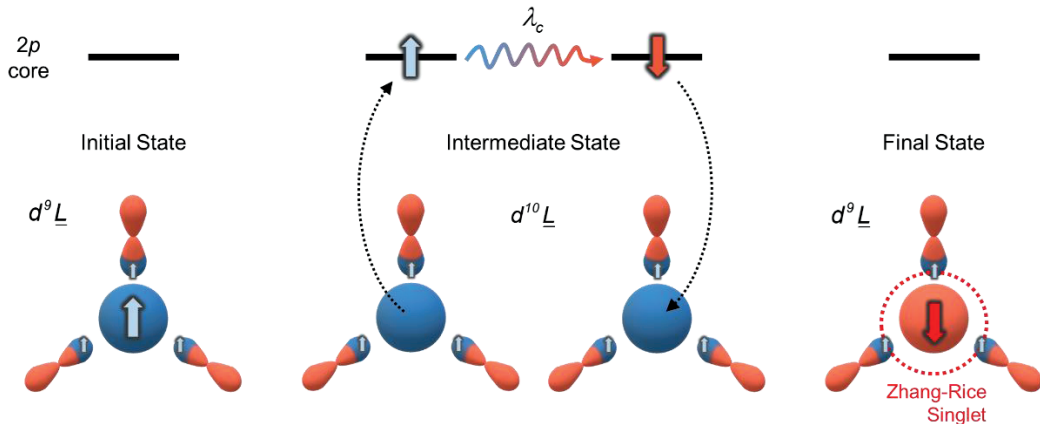


Figure 3.10. The schematic view of RIXS process with a Zhang-Rice singlet state. The arrows painted in blue and red color imply the spin states of the holes in each orbital. In the intermediate state of RIXS process, the spin is flipped due to the spin-orbit coupling and the potential of core-hole. Once the flipped spin is transferred to 3*d* orbital, it forms the singlet state with neighboring ligands.

The ZRT states originate from the strong σ -type bonding of $3d$ and $3p$ orbitals due to their geometrical characters (Figure 3.10). The lobes of $3p$ orbitals involved in the bonding point along the displacement between Ni and S sites. Because the bonding angle of Ni-S-Ni is almost 90° , 8 orbitals of two $3p$ ligand holes located at same site are almost perpendicular to each other at the neighboring ZRT states. Their spin states can be parallel or antiparallel when the spin ordering of two neighboring Ni sites is ferromagnetic or antiferromagnetic, respectively (Figure 3.11).

Figure 3.11(a) shows the schematic diagram of spin configurations when the ZRT states are formed at overall sites in the honeycomb lattice of NiPS₃ with a zigzag-type antiferromagnetic order. The spins of two holes on S sites inside the green ellipsoids are antiparallel to each other while the ones on the other ligand sites are parallel to each other. Note that the exchange Coulomb interaction or Hund's coupling prefers to the ferromagnetic spin order of two-hole states. That is to say, a pair of ligand holes with parallel spins has slightly lower energy than that with antiparallel spins due to Hund's coupling energy. For this reason, S orbitals inside the green ellipsoids in Figure 3.11(a) would have less hole density than the others. This difference can induce the local electric polarization on Ni sites. When the pair of antiparallel spins are located along $\pm\hat{b}$ from Ni site, the strength of the electrical dipole per Ni site is proportional to $\pm(\bar{n}_A - \bar{n}_F)\hat{b}$, where \bar{n}_F (\bar{n}_A) is the hole density per ligand orbital shared by two ferromagnetic(antiferromagnetic)-ordered Ni ions.

On the other hand, these ZRT states can be excited into the Zhang-Rice singlet (ZRS) states through the indirect RIXS process as shown in Figure 3.10. In Ni L_3 edge RIXS, the

spin-orbit coupling is strong enough that the valence electrons feel the core-hole potential.

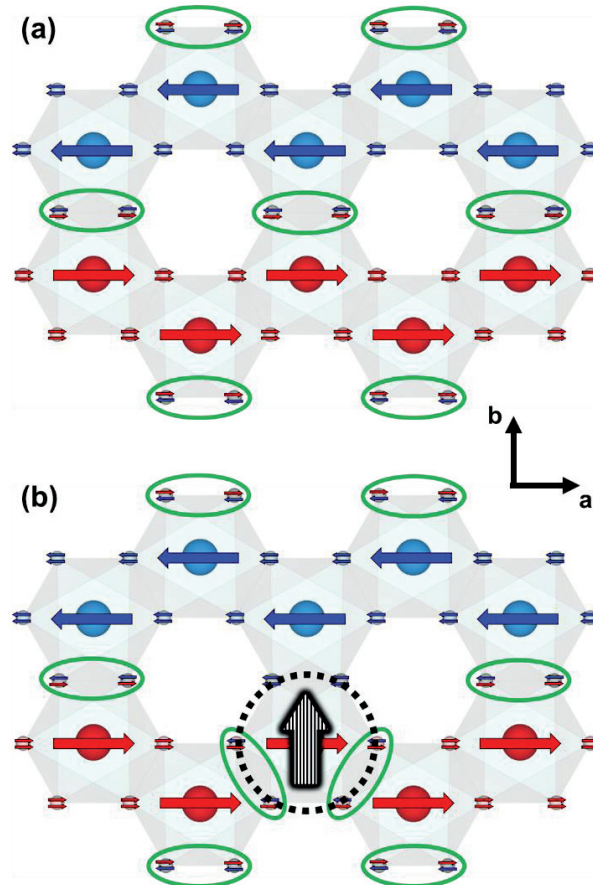


Figure 3.11. Schematic diagram of spin configurations in (a) Zhang-Rice-triplet lattice and (b) a Zhang-Rice-singlet excited lattice with zigzag antiferromagnetic order. Large (small) red and blue arrows refer to the spin direction of Ni $3d$ ($S 3p$) holes. Green ellipsoids indicate edge-shared S sites in which spins of two ligand holes are antiparallel. A black dashed circle highlights the site of ZRS. The shaded arrow inside the circle represents the direction of expected electric dipole for the ZRS.

In addition, the good quantum number of core-hole is not spin angular momentum S but total angular momentum J so that S does not need to be conserved in the intermediate process. The spin-flip excitation ($\Delta S = \pm 1$) due to the strong core-hole potential can realize the ZRS states and can be measured via Ni L_3 edge RIXS.

The process of the spin-flip excitation in the lattice gets slightly more complicated when there is a long-range zigzag antiferromagnetic order like in NiPS₃. Because Ni spins are strongly bounded by the ordering field, the spin states of holes at S sites bonded with the center Ni ion can be reversed to form the spin singlet instead of ones at Ni sites. It makes the spins at surrounding six S sites flipped. Through this spin-flip process on S orbitals, the S sites initially with parallel spin pairs will have antiparallel spin pairs and vice versa. Since the spin configuration of ligand holes can change the hole density, the spin-flip induces the local electric dipole as shown in Figure 3.11(b). In summary, the electronic correlation effects of self-doped ligand holes result in the strong charge-spin coupling, and it leads to local electric dipole with the ZRS excitation.

As we investigated in the multiplet structure, there exists the bonding state of ${}^1A_{1g}(G)$ and $t_{2g}^6 e_g^3 \underline{L}^1$, which is a spin-singlet state with ${}^1A_{1g}$ symmetry. The peak induced by this multiplet state appears near 1.44 eV in the CI calculation as shown in Figure 3.6. Note that this peak has maximum intensity at the incident energy of satellite absorption peak B, and very small peak width comparable to the elastic peak. Those characteristics of the singlet peak is quite distinct from the other excitations in RIXS spectra, considering the intensity of others is maximum at on-resonance energy (857.2 eV) and their peak width is much broader than the elastic peak.

The first feature of the peak indicates that the multiplet ground state has a $d^9\bar{L}$ electronic configuration rather than d^8 . The multiplet structure shown in Figure 3.9 supports that the partial contribution of $d^9\bar{L}$ dominates over d^8 when the energy of incident beam is tuned to the satellite region, which corresponds to 0.8~1.3 eV above the main absorption. Because the ZRT states depicted in Figure 3.11 are the ground state of this peak, we can conclude that the excitation at 1.44 eV is attributed to ZRS states.

The extra-ordinary sharpness of the ZRS peak originates from the local electric field due to the strong spin-charge coupling. The peak width of the ZRS peak is about 40 meV below 100 K, which corresponds to the energy resolution of the RIXS instrument (Figure 3.12). The local field can induce the long path way, and generate a quantum phase such as quantum Hall effects [Ref.3.34]. In this study, we verified the large spin-charge coupling leads to the local electric dipole in the zigzag type antiferromagnetic ordering on the 2D honeycomb lattice, which makes the extremely long life time of ZRS by observing an extremely sharp peak in the RIXS spectra.

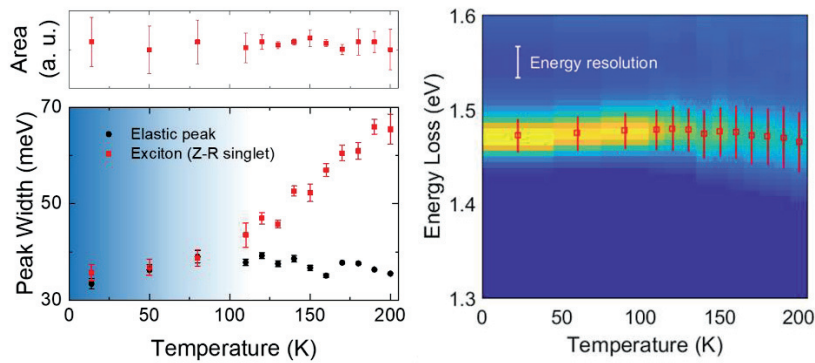


Figure 3.12. The temperature dependence of ZRS peak. At the low temperature, the peak width of ZRS peak is comparable to the energy resolution.

3.3.5 Discussion 4: Magnon dispersions

Ni L_3 edge RIXS opens an exciting opportunity to study spin dynamics by the enhanced intensity of dipolar transition and allows the spin non-conserving process. The 2D magnetism in NiPS₃ itself is another interesting subject. It has been known that NiPS₃ has the XXZ-type antiferromagnetic ordering [Ref.3.21, 3.27], which has similar Hamiltonian to the XY model. The single magnon dispersion in NiPS₃ can be obtained by the linear spin-wave theory. In order to have the zigzag pattern magnetic structure, we used J_1 - J_2 - J_3 Heisenberg Hamiltonian for the honeycomb lattice. According to previous neutron studies of the J_1 - J_2 - J_3 model, the zigzag magnetic structure can be stabilized by considering up to third-nearest neighbor interaction (J_3) [Ref.3.27]. For example, when there is an antiferromagnetic J_1 , a zigzag magnetic structure has been found if both J_2 and J_3 are larger than $0.6J_1$. To be consistent with the experimental evidence suggesting the XY symmetry in the physical properties of NiPS₃, we used the following J_1 - J_2 - J_3 XXZ Hamiltonian as given below

$$H = J_1 \sum_{\langle i,j \rangle} [S_i^x S_j^x + S_i^y S_j^y + \alpha S_i^z S_j^z] + J_2 \sum_{\langle\langle i,j \rangle\rangle} [S_i^x S_k^x + S_i^y S_k^y + \alpha S_i^z S_k^z] \\ + J_3 \sum_{\langle\langle\langle i,j \rangle\rangle\rangle} [S_i^x S_k^x + S_i^y S_k^y + \alpha S_i^z S_k^z] + \sum_i [D_1 (S_i^x)^2 + D_2 (S_i^z)^2]$$

First three terms denote the XXZ anisotropic Hamiltonian up to third nearest neighbors with an anisotropy parameter α . The last terms in the bracket are single-ion anisotropies (SIA) along the x- and z-axes, respectively. We neglected an inter-layer coupling as it is

known to be smaller by two orders of magnitude than the intra-layer coupling.

J_1	J_2	J_3	α	D_1	D_2
3.18	4.82	9.08	0.66	-0.89	2.85

Table 3.2. The parameters used in spin wave calculations (in meV).

Two-magnon spectrum corresponds to the sum of the two single-magnon with a total momentum of $\mathbf{q} = 0$. We calculated the two-magnon DOS in the following way. First, for a given \mathbf{k} point of the two magnon continuum, a single-magnon dispersion is calculated at randomly chosen one million sampling \mathbf{q} points using the SpinW software [Ref.3.35]. After that, two-magnon DOS was calculated with the following sum rule satisfying kinematic constraints,

$$D_{\mathbf{k}}(\varepsilon_{\mu\mathbf{k}}) = \pi \sum_{\mathbf{q}, mn} \delta(\varepsilon_{\mu, \mathbf{k}} - \varepsilon_{m, \mathbf{q}} - \varepsilon_{n, \mathbf{k}-\mathbf{q}}),$$

where $\varepsilon_{\mu, \mathbf{k}}$ is the dispersion of the μ -th magnon band. The parameters used in this calculation is described in Table 3.2.

Figure 3.13 shows the experimental and theoretical results in a low energy region. We successfully observed both single-magnon dispersion and bimagnon continuum. The dispersion of single magnon is extended from 10 to 50 meV, and the bimagnons are distributed up to 85 meV. The theoretical expectation is in excellent agreement with the experimental results. The fitting results of two-magnon peak indicates that the magnetic ordering disappears above the transition temperature of 160 K.

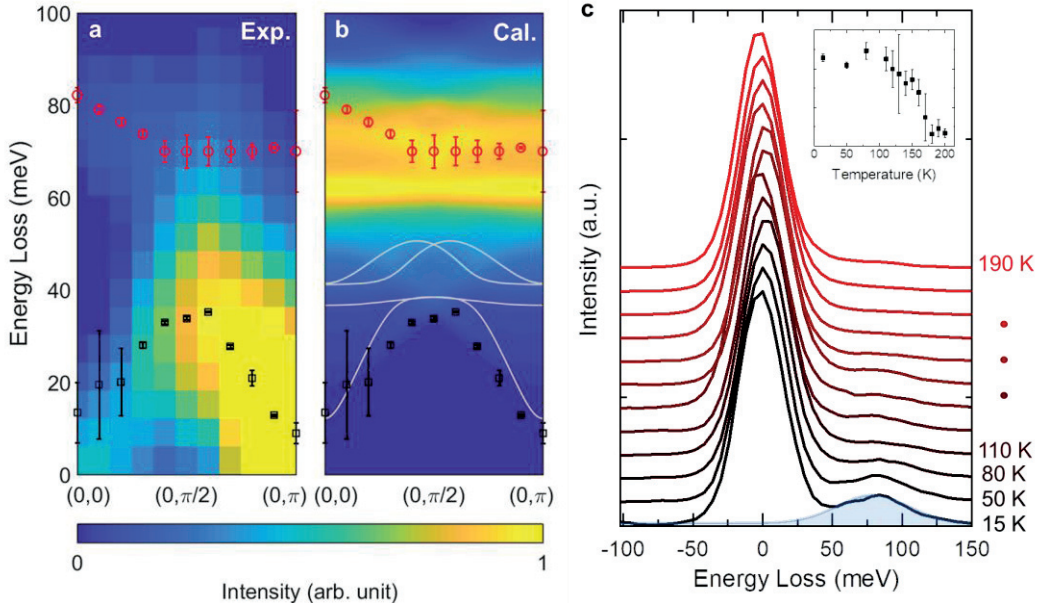


Figure 3.13. Magnon dispersion and two-magnon continuum in XXZ-type antiferromagnet NiPS₃. (a) Low energy excitations in RIXS spectra with Q_{\parallel} dependence along b^* axis at 15 K. Black squares and red circles respectively correspond to the fitted magnon and two-magnon energies. (b) Calculated magnon spin waves and two-magnon DOS using parameters described in Table 3.2. (c) Temperature dependence of low energy excitations. The blue colored shaded peak shows a fitting result of two-magnon continuum at 15 K. The inset graph indicates the intensity of two-magnon continuum as a function of temperature.

3.4 Conclusion

We investigated the strong spin-charge coupling and the XXZ-type magnetic ordering in

vdW antiferromagnet NiPS₃. The high-resolution Ni L_3 edge RIXS enables the observation of the spin-flip process and the single magnon dispersion. The complex multiplet structure attributed to the small CT in NiPS₃ makes an unconventional d^8 and $d^9\bar{L}$ mixed ground state, which connected to the energy dependence of the excitations. When the ground states have the $d^9\bar{L}$ electronic structure, ZRT states can be stabilized. ZRT can be excited to ZRS states, which induces a local electric dipoles in zigzag antiferromagnetic order on 2D honeycomb lattice. The verification of ZRS at 1.44 eV and its nature supports that the electronic correlation of S $3p$ ligand-hole orbitals plays an important role in the spin-charge of self-doped NiPS₃ and the creation induces local electric fields because of the different behavior of the hole-density against the magnetic ordering. In addition, we got a clear evidence of XXZ-type antiferromagnetism in the low energy region below 100 meV. It is noteworthy that this observation is the first single-magnon dispersion in NiPS₃ single crystal and the results contains both single-magnon dispersion and two-magnon continuum in one graph.

References

- [Ref.3.1] V. Berezinskii, Sov. Phys. JETP **32**, 493 (1971).
- [Ref.3.2] J. M. Kosterlitz, and D. J. Thouless, J. Phys. C **6**, 1181 (1973).
- [Ref.3.3] N. D. Mermin, and H. Wagner, Phys. Rev. Lett. **17**, 1133 (1966).
- [Ref.3.4] L. Onsager, Phys. Rev. **65**, 117 (1944).
- [Ref.3.5] A. Kitaev, Ann. Phys. **321**, 2 (2006).

- [Ref.3.6] N. Samarth, *Nature* **546**, 216 (2017).
- [Ref.3.7] F. Hellman, et. al., *Rev. Mod. Phys.* **89**, 025006 (2017).
- [Ref.3.8] K. S. Novoselov, A. K. Geim, S. V. Morozov, D. Jiang, Y. Zhang, S. V. Dubonos, I. V. Grigoieva, and A. A. Firsov, *Science* **306**, 666 (2004).
- [Ref.3.9] J.-G. Park, *J. Phys. Condens. Matter* **28**, 301001 (2016).
- [Ref.3.10] K. S. Burch, D. Mandrus, and J.-G. Park, *Nature* **563**, 47 (2018).
- [Ref.3.11] S. Blundell, *Magnetism in Condensed Matter* (Oxford University Press, Oxford, 2001).
- [Ref.3.12] E. Ising, *Zeitschrift fur Physik* **31**, 253 (1925).
- [Ref.3.13] W. Heisenberg, *The Physical Principles of the Quantum Theory* (Courier Corporation, New York, 1949).
- [Ref.3.14] B. Huang, G. Clark, E. Navarro-Moratalla, D. R. Klein, R. Cheng, K. L. Seyler, D. Zhong, E. Schmidgall, M. A. McGuire, D. H. Cobden, W. Yao, D. Xiao, P. Jarillo-Herro, and X. Xu, *Nature* **546**, 270 (2017).
- [Ref.3.15] B. V. Costa, and A. B. Lima, *J. Mag. Magn. Mater.* **324**, 1999 (2012).
- [Ref.3.16] S. Muhlbauer, B. Binz, F. Jonietz, C. Pfleiderer, A. Rosch, A. Neubauer, R. Georgii, and P. Boni, *Science* **323**, 915 (2009).
- [Ref.3.17] S. Son, M. J. Coak, N. Lee, J. Kim, T. Y. Kim, H. Hamidov, H. Cho, C. Liu, D. M. Jarvis, P. A. C. Brown, J. H. Kim, C.-H. Park, D. I. Khomskii, S. S. Saxena, and J.-G. Park, *Phys. Rev. B* **99**, 041402(R) (2019).
- [Ref.3.18] C. Gong, L. Li, Z. Li, H. Ji, A. Stern, Y. Xia, T. Cao, W. Bao, C. Wang, Y. Wang, Z. Q. Qiu, R. J. Cava, and S. G. Louie, *Nature* **546**, 265 (2017).

- [Ref.3.19] M. Bonilla, S. Kolekar, Y. Ma, H. C. Diaz, V. Kalappattil, R. Das, T. Eggers, H. R. Guterrez, M.-H. Phan, and M. Batzill, *Nat. Nanotechnol.* **13**, 289 (2018).
- [Ref.3.20] D. J. O'Hara, T. Zhu, A. H. Trout, A. S. Ahmed, Y. K. Luo, C. H. Lee, M. R. Brenner, S. Rajan, J. A. Gupta, D. W. McComb, and R. K. Kawakami, *Nano Lett.* **18**, 3125 (2018).
- [Ref.3.21] J.-U. Lee, S. Lee, J. H. Ryoo, S. Kang, T. Y. Kim, P. Kim, C.-H. Park, J.-G. Park, and H. Cheong, *Nano Lett.* **16**, 7433 (2016).
- [Ref.3.22] S. Lee, K.-Y. Choi, S. Lee, B. H. Park, and J.-G. Park, *APL materials* **4**, 086108 (2016).
- [Ref.3.23] C.-T. Kuo, M. Neumann, K. Balamurugan, H. J. Park, S. Kang, H. W. Shiu, J. H. Kang, B. H. Hong, M. Han, T. W. Noh, and J.-G. Park, *Scientific Reports* **6**, 20904 (2016).
- [Ref.3.24] K. Kim, S. Y. Lim, J.-U. Lee, S. Lee, T. Y. Kim, K. Park, G. S. Jeon, C.-H. Park, J.-G. Park, and H. Cheong, *Nat. Comm.* **10**, 345 (2019).
- [Ref.3.25] Y. Cao, V. Fatemi, S. Fang, K. Watanabe, T. Taniguchi, E. Kaxiras, and P. Jarillo-Herrero, *Nature* **556**, 43 (2018).
- [Ref.3.26] R. Brec, *Solid State Ionics* **22**, 3 (1986).
- [Ref.3.27] D. Lancon, R. A. Ewings, T. Guidi, F. Formisano, and A. R. Wildes, *Phys. Rev. B* **98**, 134414 (2018).
- [Ref.3.28] S. Y. Kim, T. Y. Kim, L. J. Sandilands, S. Sinn, M.-C. Lee, J. Son, S. Lee, K.-Y. Choi, W. Kim, B.-G. Park, C. Jeon, H.-D. Kim, C.-H. Park, J.-G. Park, S. J. Moon, and T. W. Noh, *Phys. Rev. Lett.* **120**, 136402 (2018).

[Ref.3.29] G. Ghiringhelli, M. Matsubara, C. Dallera, F. Fracassi, R. Gusmeroli, A. Piazzalunga, A. Tagliaferri, N. B. Brookes, A. Kotani, and L. Braicovich, *J. Phys. Condens. Matter* **17**, 5397 (2005).

[Ref.3.30] R. J. Green, M. W. Haverkort, and G. A. Sawatzky, *Phys. Rev. B* **94**, 195127 (2016).

[Ref.3.31] F. de Groot, *Coord. Chem. Rev.* **249**, 31 (2004).

[Ref.3.32] L. J. P. Ament, M. van Veenendaal, T. P. Devereaux, J. P. Hill, and J. van den Brink, *Rev. Mod. Phys.* **83**, 705 (2011).

[Ref.3.33] F. de Groot, *J. Phys.: Condens. Matter* **6**, 8625 (1994).

[Ref.3.34] Y.-M. Li, J. Li, L.-K. Shi, D. Zhang, W. Yang, and K. Chang, *Phys. Rev. Lett.* **115**, 166804 (2015).

[Ref.3.35] S. Toth, and B. Lake, *J. Phys. Condens. Matter* **27**, 166002 (2015).

Chapter 4

Orbital-Selective Confinement Effect and Metal-Insulator Transition of Ru 4*d* Orbitals in SrRuO₃ Ultrathin Film

4.1. Quantum confinement effect in low dimensional systems

4.1.1. General description of quantum confinement effects

In most cases of condensed matter physics, researchers concerns the bulk properties of crystal. It means that the crystals of interest are often assumed to be large enough to neglect the impact of finite dimensions on the electronic structure compared to the effect of periodic potential by the lattice. In these common cases, the energy of the electrons in a valence band of a metal can be simply described with the propagation wave vector whose size $k = 2\pi/\lambda$, where λ is the wavelength of an electron.

On the other hand, once the crystal gets thinner or smaller and finally the dimension of crystal reaches the comparable length of interatomic distances or the wavelength of an electron, the energy of the electron is affected by not only the periodic potential but also the crystal boundaries. The boundaries between the crystal and the surrounding environment, or so-called boundary conditions, outside the crystal act like wells as we learned in quantum mechanics. The effect of the drastic change of potential at the boundaries can be explained

by the famous jellium model [Ref.4.1]. The Jellium model is a quantum mechanical model describing the interaction of electrons with the assumption that the ions are considered to form a uniform positive background. As a result, the wave vectors of the electrons should be confined inside the crystal like Figure 4.1.

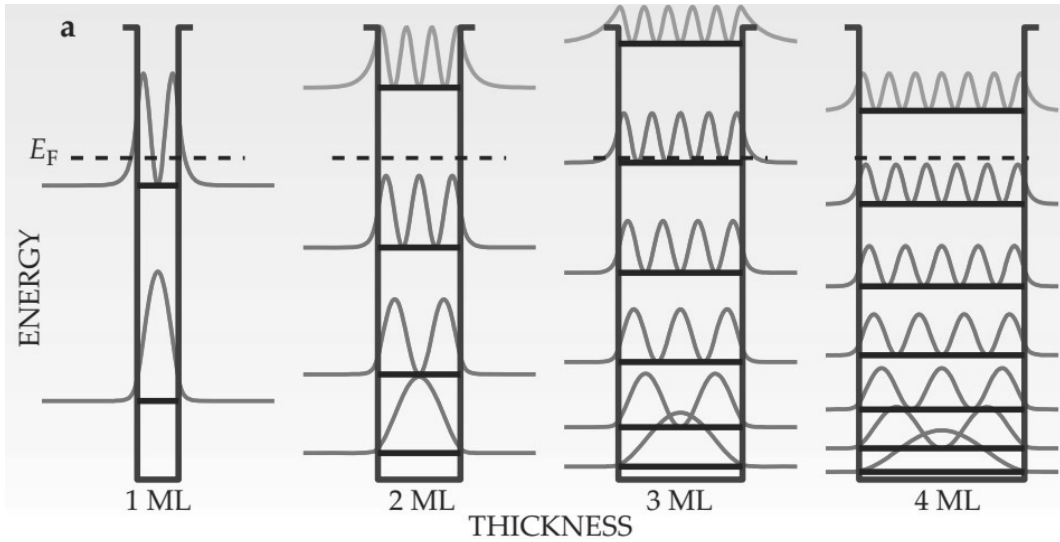


Figure 4.1. Confined electron wave vectors in ultrathin films whose thickness is from one to four monolayers [Ref.4.2].

Ultrathin films and nano-wires are the famous examples of the materials that feels the boundaries, which results in the confinement of electrons. This phenomena is known as quantum size effects or quantum confinement effects (QCE). Since the electrons in these kinds of material affected by the boundaries, the phase difference must obey the Sommerfeld-Bohr quantization rule: $2k_z d + \Phi_1 + \Phi_2 = 2\pi n$ [Ref.4.2], where k_z is the z component of allowed wave vector, d is the thickness of crystal, $\Phi_1(\Phi_2)$ is the phase

term across the boundary. These QCE can influence significantly the physical properties such as conductivity, surface energy, Hall effects, and chemical reactivity in the crystal [Ref.4.3, 4].

4.1.2. Quantum confinement effects and magnetic transitions in SrRuO₃ thin films

The QCEs in SrRuO₃ thin films are first suggested by a way to explain the magnetic transition with reducing the thickness [Ref.4.5]. The bulk SrRuO₃ has a long range ferromagnetic order below the Curie temperature of 160 K [Ref.4.6]. As the thickness gets reduced, however, the magnetic properties becomes paramagnetic instead of ferromagnetic [Ref.4.6, 4.7]. The ferromagnetic ground states of SrRuO₃ can be described by Stoner model. The kinetic energy and the exchange energy compete with each other, and the ferromagnetic state become a ground state when $IN_0 > 1$, where I is the electron-electron interaction and N_0 is the nonmagnetic density of states (DOS) at Fermi level. In addition, Curie temperature should change with the variation of the nonmagnetic DOS.

As the t_{2g} orbitals have the anisotropic shape toward different orientations, each type of orbital has directional hybridizations with oxygen $2p$ orbitals in a RuO₆ octahedron. In a bulk SrRuO₃ case, the d orbitals of ruthenium ions interact in two-dimensional network, and the energy of each t_{2g} orbital gets extended in a different plane is degenerated. However, when it comes to an ultrathin region, the interaction of d orbitals toward the z -direction gets smaller due to the geometrical restriction. For example, in a monolayer SrRuO₃ [001] case,

there is no more orbitals pointing toward the z-direction. In this situation, the d_{xy} orbitals still interact in a two-dimensional network while $d_{xz}(d_{yz})$ orbitals has a one-dimensional chain network. The wave functions of electrons in the material are now confined in one or two dimension, i.e., the film exhibits QCE. QCE modifies the DOS in ultrathin film as shown in Figure 4.2. The van Hove singularity in three-dimension is simple parabolic but it changes in low dimensional limits. The van Hove singularity is at the center of band in two-dimensional limit and it is at the edges of band in one-dimensional limits [Ref.4.1] (Figure 4.3).

It is notable that this systematic change of the DOS is orbital-selective. As individual t_{2g} orbitals have a different network in the ultrathin film, each of them has a different type of van Hove singularity. While the d_{xy} orbital has 2D van Hove singularity, the others have 1D van Hove singularity. For this reason, the degenerate t_{2g} levels should be split and it subsequently stabilizes the nonmagnetic ground state.

Although the change of Curie temperature in the electrical conductivity give an evidence of QCE in SrRuO₃, direct evidence of QCE has not yet been reported in transition metal oxide thin films. As the QCE in the SrRuO₃ thin film originates from the strong hybridization of Ru 4d and O 2p orbitals, I utilized the O K edge RIXS to provide an direct evidence of QCE by investigating CT excitations.

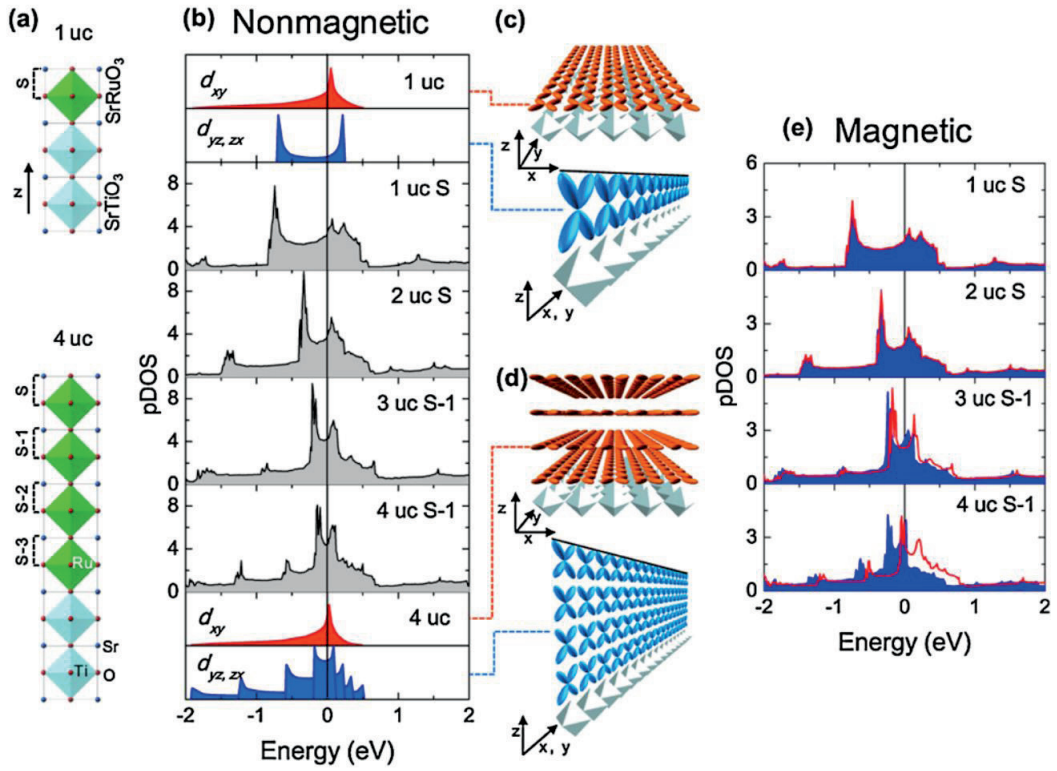


Figure 4.2. Variation of nonmagnetic and magnetic partial density of states as a function of thickness of films [Ref.4.6].

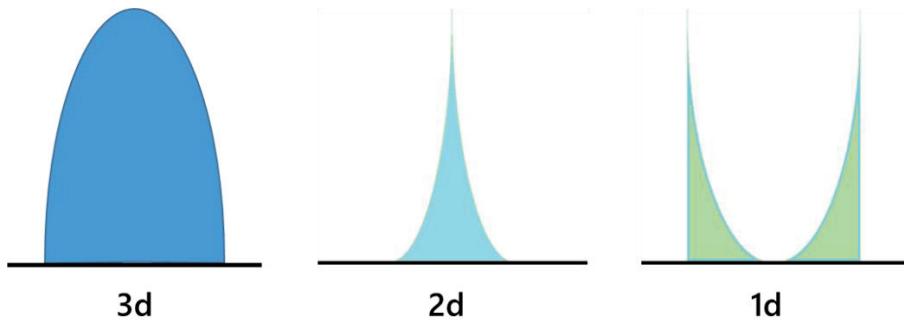


Figure 4.3. Schematic view of typical change of van Hove singularity in different dimension limits.

4.2. Metal-insulator transition in SrRuO₃ thin films

Another interesting feature of SrRuO₃ is its good electrical conductivity. Unlike other ferromagnetic materials, the conductivity of bulk SrRuO₃ is high enough to make it a popular choice of electrode for various thin-film samples with a stable perovskite structure [Ref.4.8, 4.9]. For this reason, SrRuO₃ has also been applied in numerous state-of-the-art technology such as Josephson junctions [Ref.4.10], magnetic tunneling junctions [Ref.4.11], Schottky junctions [Ref.4.12], field effect devices [Ref.4.13], ferroelectric capacitors [Ref.4.14, 4.15], and multiferroic devices [Ref.4.16]. Interestingly, it is known too that the metallic phase of bulk SrRuO₃ is close to a transition between Fermi-liquid and non-Fermi-liquid states [Ref.4.17, 4.18]. Another interesting point, more relevant to my work, is that SrRuO₃ thin films undergo a metal-insulator transition (MIT) with decreasing thickness, whose origin is, to date, not well understood [Ref.4.5, 4.19, 4.20].

In the following sections, I will try to explain this exotic MIT including the QCE of SrRuO₃. Figure 4.4 shows the basic idea to combine the QCE and MIT on SrRuO₃ thin films. As I described in the previous section, QCE transforms the DOS of respective t_{2g} orbitals and split the energy levels. In case the Fermi level is located between two different van Hove singularities, the insulating phase can be formed by confining the conduction electrons. Choosing the pre-edge incident energy will allow us to observe both $d-d$ excitations and CT excitations involving electron-hole continuum.

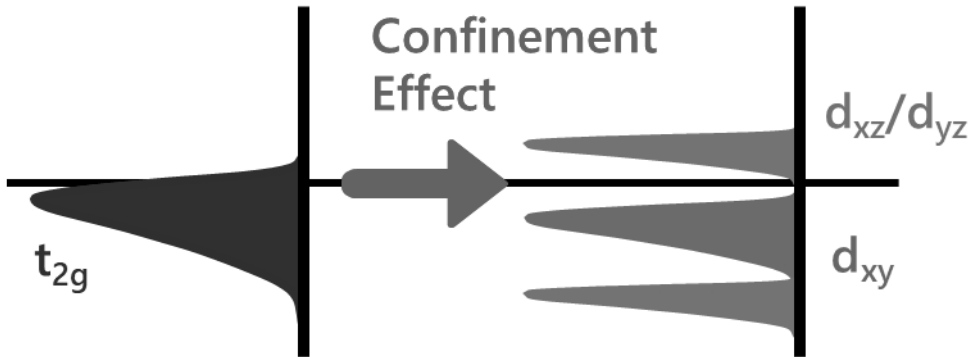


Figure 4.4. The mechanism of orbital-selective quantum confinement effects inducing metal-insulator transition in SrRuO₃ thin films.

4.3. RIXS experiment in SrRuO₃ thin films

The purpose of this study was twofold. First, we wanted to investigate the proposed QCE by measuring the orbital-dependent charge transfer with the high-resolution O *K* edge RIXS studies as a function of thickness. Second, we want to study how the charge dynamics changes across the MIT by examining low-energy excitations across the critical thickness. Furthermore, we tried to find a correlation between those two distinct characteristics of the SrRuO₃ thin films.

4.3.1 Results: XAS and RIXS spectra as a function of thickness

The proper energy of the incident beam was chosen through the fluorescence XAS experiment with different thicknesses from 1 to 33 unit cells (u.c.), as shown in Figure 4.5.

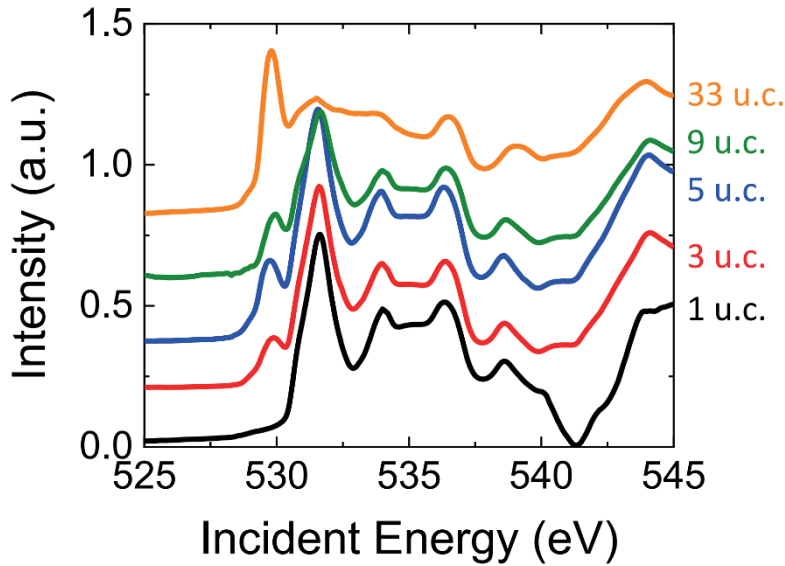


Figure 4.5. XAS results as a function of the thickness of the sample. An energy of 529.8 eV was utilized for our RIXS experiments since other peaks mainly originate from the SrTiO₃ substrate [Ref.4.23].

The first peak at around 529.8 eV gets weaker as the thickness of the samples becomes reduced. From the fact that the relative intensity changes for different samples and also based on previous XAS studies in SrTiO₃ [Ref.4.21, 4.22], I concluded that peaks above 530 eV are mainly due to absorptions from the substrates. Therefore, I chose 529.8 eV as the incident energy for RIXS experiment with high statistics, which is slightly lower than the pure O *K* edge. The energy difference between the pure O *K* edge and absorption from our sample comes from the hybridization energy. At O *K* edge region, the x-ray photon promotes the O 1s core electron and the photoelectron annihilates an O 2p hole, which is strongly hybridized to a metal *d* orbital. After a short time, another O 2p electron decays,

filling the O 1s core hole and leaving the system in an excited state. Thus, the O *K* edge RIXS here is a direct RIXS process.

Figure 4.6 shows RIXS results for all seven samples with different thicknesses. To explain the RIXS spectra, I roughly divided the spectra into two groups depending on the characteristic energy of the peaks and their apparent relevance to our two main questions: QCE and MIT. For example, on the high energy side ranging from 2 to 10 eV there are several strong peaks, marked as C and D. These peaks are due to the charge transfer from O 2*p* to Ru 4*d* orbitals and so reflect the expected change in the Ru 4*d* orbitals. I employed two different linear polarizations for the experiments: σ polarization is parallel to the sample plane and π polarization is nearly perpendicular to the plane. Thus, the former is more sensitive to the p_x (p_y) orbital while the latter is more sensitive to the p_z orbital due to the incident angle. As a result, the orbital selective properties of QCE can be investigated by comparing the spectra with different polarization.

On the other hand, there are two relatively weaker peaks below 2 eV with a strong thickness dependence. These low-energy excitations can be interpreted as arising from *d-d* excitations or coherent peaks connected to quasiparticle states that are closely related to the metallic phase of SrRuO₃. In the remainder of this chapter, I focus on the charge transfers to explain the QCE first and then move on to the low-energy part for the MIT.

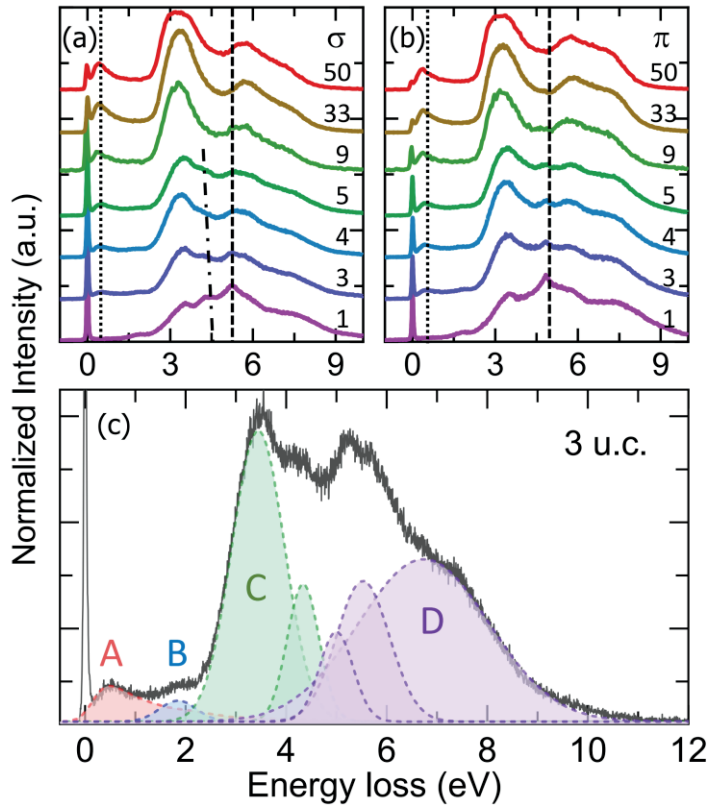


Figure 4.6. (a) and (b) Overall feature of O *K* edge RIXS spectra with σ and π polarizations for SrRuO₃ thin films. As the thickness decreases, the peak on the low-energy side (dot line) becomes weaker, while the peak at 5 eV (dashed line) gets stronger for both polarizations. In addition to the 5 eV peak, the peak around 4.5 eV (dash-dotted line) also appears for the σ polarization. Note that this 4.5 eV peak becomes stronger below the 5-u.c. sample and shifts towards higher energy with decreasing thickness. (c) The whole spectrum for the 1-u.c. sample with σ polarization. Altogether, seven Gaussian fitting functions are needed to fit the spectra based on the theoretical calculations explained in discussions. Different types of peaks are marked by different letters in (c) [Ref. 4.23].

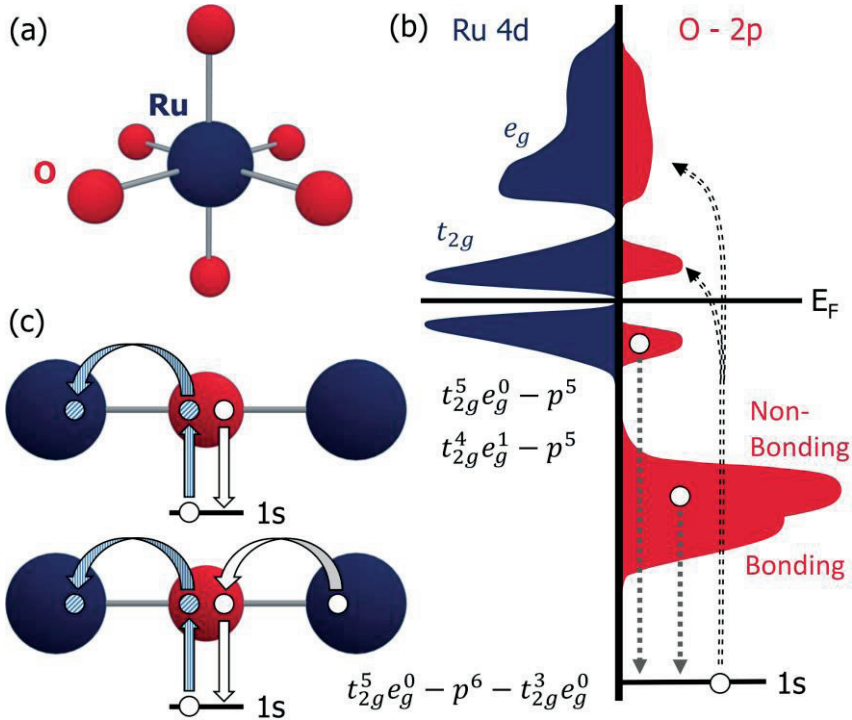


Figure 4.7. (a) RuO₆ cluster used in the configuration interaction calculation. (b) and (c) Schematic view of charge transfer and $d-d$ excitations. Oxygen 1s electrons are excited to vacant 2p levels which are hybridized with Ru t_{2g} orbitals. The energy losses should be different depending on orbitals from which the relaxation occurs. The top panel in (c) shows $t_{2g}-e_g$ excitations, and the bottom one indicates the charge transfer from O 2p to Ru 4d levels [Ref.4.23].

4.3.2 Discussion 1: Configuration interaction calculations

In order to explain the peaks related to CT and d-d excitations, we performed the configuration (CI) calculations using two cluster models of RuO₆ and Ru-O-Ru (Figure 4.7). Each of the calculations with different clusters shows the distinct features of SrRuO₃. For instance, the calculation with the RuO₆ cluster model has the advantage of explaining the charge transfer between O 2*p* and Ru *d* orbitals because the cluster consists of six oxygen atoms. On the other hand, the calculation with the Ru-O-Ru cluster gives a better description of intersite *d-d* excitations. We note that our model calculations are acceptable to interpret RIXS experiments whose process is about the localized *t*_{2g} orbitals in an ion.

These calculations can also reflect the QCE by the extra control of adjusting the amount of Ru *d* splitting. As the QCE alters the DOS of individual *t*_{2g} orbitals depending on their geometrical character, there can be energy level splitting between *d*_{xy} and *d*_{xz} (*d*_{yz}) orbitals. This splitting of *t*_{2g} energy level resembles that of tetragonally distorted octahedron. Hence, the artificial energy splitting between Ru *d* orbitals is apply to realize the QCE. For example, we set Ru *d* orbitals to split into $\varepsilon_{xy} = 2/3\Delta_{t_{2g}}$, $\varepsilon_{xz} = \varepsilon_{yz} = -1/3\Delta_{t_{2g}}$, $\varepsilon_{z^2} = 10Dq - 1/2\Delta_{e_g}$, and $\varepsilon_{x^2-y^2} = 10Dq + 1/2\Delta_{e_g}$. It should be noted that we used an unusually large energy splitting between *d*_{xy} and *d*_{xz} (*d*_{yz}) orbitals ($\Delta_{t_{2g}} = 0.8$ eV) from the results of the first-principles calculation in Ref.4.5, which corresponds to the energy difference between the 2D-type singularity of *d*_{xy} and the 1D-type singularity of *d*_{xz} (*d*_{yz}).

We also take into account both the spin-orbit coupling λ and the Kanamori-type Coulomb interaction (*U* and *J*_H) among *d* orbitals [Ref.4.24]. The energy levels of oxygen *p* orbitals

in the valence band can depend on whether they are hybridized with Ru d orbitals or not [Ref.4.25-27]. For example, O $2p$ orbitals are assumed in our calculations to be non-interacting, and their energy levels are given as e_p for nonbonding p orbitals and $e_p - \Delta_p$ for bonding p orbitals. Here, e_p is determined as $e_p = 4U - 7J_H - \Delta$, where Δ is the CT energy in the cubic symmetry defined as the energy difference between the lowest $d^5\bar{L}$ and d^4 states. The hopping integrals between the p and d orbitals are parameterized by $V_{pd\pi}$ for t_{2g} orbitals and $V_{pd\sigma}$ for e_g orbitals according to the Slater-Koster theory [Ref.4.28]. We used the parameters shown in Table 4.1 in order to fit the experimental RIXS spectrum.

For more details on our calculations, let $|\Psi_g\rangle$ and E_g be the ground state and its energy, respectively. In the dipole and fast collision approximation, the oxygen K-edge RIXS intensity at zero momentum is given as

$$I \sim -\frac{1}{\pi} \text{Im} \left\langle \Psi_g \left| \hat{R}(\epsilon, \epsilon') \frac{1}{\omega - H + E_g + i\delta} \hat{R}(\epsilon, \epsilon') \right| \Psi_g \right\rangle.$$

And $\hat{R}(\epsilon, \epsilon')$ is the RIXS scattering operator, given as

$$\hat{R}(\epsilon, \epsilon') = \frac{1}{3} \sum_{imm'\sigma} \epsilon_m \epsilon'_{m'} c'_{im\sigma} c^\dagger_{im'\sigma},$$

where $c^\dagger_{im'\sigma}$ is the creation operator of the oxygen p electron with the $m = (x, y, z)$ orbital and σ spin at the i th site and ϵ and ϵ' are the polarizations of incident and outgoing x-rays, respectively [Ref.4.24]. Here, δ is the Lorentz broadening, and we set $\delta = 0.2$ eV for our calculations.

In our calculations, p -orbital states can be expressed with a linear combination of bonding and nonbonding states as

$$c_{im'\sigma}^\dagger = \sum_{\alpha} (U_{\alpha,im}^B)^* c_{\alpha\sigma}^\dagger + \sum_{\mu} (U_{\mu,im}^N)^* c_{\mu\sigma}^\dagger,$$

where $U_{\alpha,im}^B$ and $U_{\mu,im}^N$ are the coefficients of the m orbital at the i th site for bonding and nonbonding states α and μ , respectively. Because nonbonding p orbitals are fully occupied in the ground state, only the annihilation operation is allowed. We can then get the scattering operator associated with nonbonding orbitals as follows:

$$\hat{R}^N(\epsilon, \epsilon') = \sum_{\alpha\mu\sigma} R_{\alpha\mu}^N(\epsilon, \epsilon') c_{\mu\sigma} c_{\alpha\sigma}^\dagger,$$

where $R_{\alpha\mu}^N = \frac{1}{3} \sum_{imm'} U_{\mu,im'}^N (U_{\alpha,im}^B)^* \epsilon_{m'} \epsilon_m$. The RIXS intensity attributed to nonbonding p orbitals is given as

$$I^N = -\frac{1}{\pi} \text{Im} \sum_{\alpha\alpha'\mu} R_{\alpha'\mu}^N(\epsilon, \epsilon')^* R_{\alpha\mu}^N(\epsilon, \epsilon') \langle \Psi_g | c_{\alpha'\sigma} \frac{1}{\omega - H + E_g + e_p + i\delta} c_{\alpha\sigma}^\dagger | \Psi_g \rangle.$$

The RIXS intensity attributed to the bonding p orbitals can then be calculated using the following relation:

$$I^B = -\frac{1}{\pi} \text{Im} \langle \Psi_g | \hat{R}^B(\epsilon, \epsilon') \frac{1}{\omega - H + E_g + i\delta} \hat{R}^B(\epsilon, \epsilon') | \Psi_g \rangle,$$

where

$$\hat{R}^B(\epsilon, \epsilon') = \frac{1}{3} \sum_{\alpha\beta\sigma imm'} U_{\alpha,im'}^B (U_{\alpha,im}^B)^* \epsilon_{m'} \epsilon_m c_{\beta\sigma} c_{\alpha\sigma}^\dagger.$$

In the case of the CI calculation of a Ru-O-Ru cluster, mainly to explain the low-energy excitations, we directly used the equations of zero momentum case instead of considering

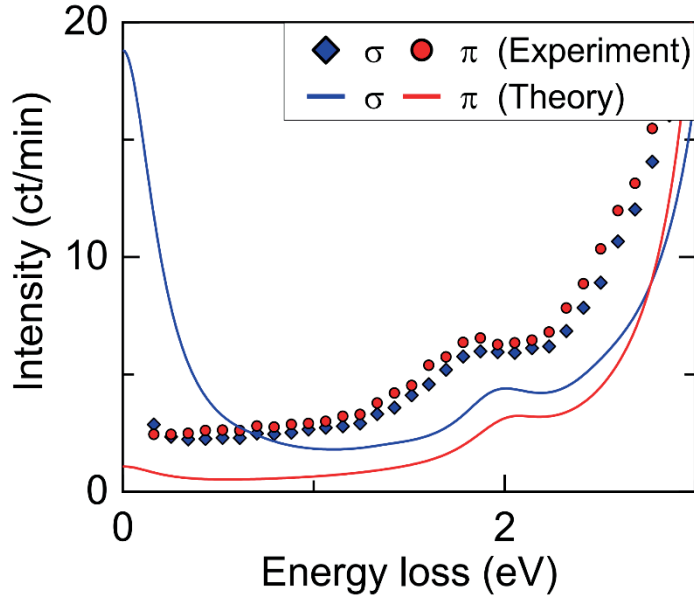


Figure 4.8. Low-energy RIXS spectra of 1 u.c. SrRuO₃ with the CI calculation of a Ru-O-Ru cluster. The symbols represent the experimental results, while the lines show the theoretical results, with different colors used for the different polarizations of the incident beam. The peak at 2 eV shows intersite *d-d* excitations.

bonding and nonbonding states. In addition, we restricted the Hilbert space with the assumption that the oxygen atom between two Ru atoms has three possible states, p^4 , p^5 , and p^6 electron configurations. The result of Ru-O-Ru calculation is shown in Figure 4.8.

The peaks in the O *K* edge RIXS spectrum can also be categorized according to Ru *4d* orbitals that participate in the RIXS process. Electrons in the core oxygen levels are excited to vacant O *2p* levels that are hybridized with Ru *4d* orbitals as seen in the O *K* edge RIXS, and the subsequent relaxation occurs from the occupied *2p* states. Note that the explanation such as ‘CT excitations from O *2p* to Ru *4d*’ does not mean that the core electron is excited

10Dq	$\Delta_{t_{2g}}$	Δ_{e_g}	λ	U	J_H	Δ	Δ_p	$V_{pd\sigma}$	$V_{pd\pi}$
2.1	0.8	0.4	0.1	2.0	0.3	3.3	1.6	-1.0	0.46

Table 4.1. Physical parameters used for the CI calculations (in eV).

to Ru 4*d* orbital level. As shown in Figure 4.7, the photoelectron always heads for O 2*p* hole strongly hybridized with Ru 4*d* orbitals. We can, in principle, determine the origin of each peak by examining the energy of the emitted photons. For example, if the electrons are relaxed from the 2*p* level hybridized with *t*_{2g} levels that are located right below the Fermi level, the process can be considered *d-d* excitations. In the case of CT between the 2*p* and 4*d* orbitals, however, the relaxation starts from the 2*p* states not participating in the hybridization.

4.3.3 Discussion 2: Quantum confinement effects

According to our CI calculations, the CT excitations correspond to peaks C and D as observed from 2 to 10 eV. Peak C, for instance, represents the CT between nonbonding O 2*p* states and Ru *t*_{2g} orbitals, while peak D mainly originates from bonding O 2*p* states and Ru *e*_g orbitals. As shown in the top graphs of Fig. 3, both peaks C and D undergo a considerable change depending on the thickness of the sample and the polarization of the incident beam. The remarkable change in peak C is clearly seen around 4.4 eV. It is notable that this variation occurs only for the σ polarization. Meanwhile, an additional peak emerges around 5 eV that is most likely due to the charge transfer between O 2*p* and Ru *e*_g

levels in both polarization channels, but the position of the peak is slightly different depending on the polarization as shown in Figure 4.9.

The splitting of both peaks shown in Figure 4.6 and 4.9 can be taken as evidence of the QCE, which is more pronounced for the thinner samples. The splitting of peaks around 4 and 5 eV reflects the energy splitting of Ru t_{2g} and e_g , respectively. Of interest, the QCE in monolayer SrRuO₃ modifies the electronic structure, which subsequently induces the separate orbital energy levels depending on the geometrical characteristics of each orbital. We comment that the energy difference between each singularity of the 2D-type band for d_{xy} and the 1D-type band of d_{xz} (d_{yz}) corresponds quite well to the amount of peak splitting in peak C [Ref.4.5]. It should also be noted that 0.8 eV of t_{2g} energy splitting cannot be obtained in the cases of the usual Jahn-Teller distortion, which is typically about 0.1 eV for t_{2g} of ruthenates [Ref.4.29].

A further interesting point is the polarization dependence of the peaks. In our explanation, the QCE pushes the energy levels of d_{xz} (d_{yz}) or d_{z^2} down, so that the energy of CT related to those orbitals gets shifted towards lower energy. On the other hand, orbitals such as d_{xy} and $d_{x^2-y^2}$ move in the opposite direction. In the case of the CT between d_{xz} (d_{yz}) and p orbitals, the same amount of energy shift compensates for the hopping integral $V_{pd\sigma}$. Thus, the additional peak at 4.4 eV appears only with the orbitals parallel to the surface of the samples, and the one around 5 eV emerges at different energies depending on the polarization of the incident beam. Because each polarization excites different O p orbitals, we believe that the “orbital-selective” characteristic of the QCE results in the observed polarization dependence.

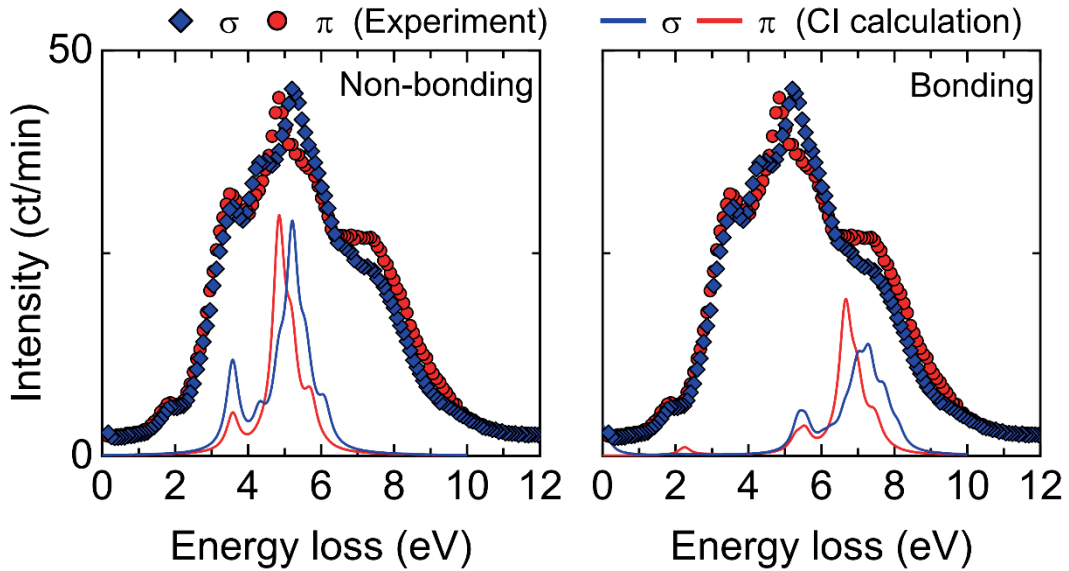


Figure 4.9. RIXS spectra with the results of CI calculation for monolayer SrRuO₃. The symbols represent the experimental results, while the lines show the theoretical results, with different colors used for the different polarizations. (Left) Calculation results with nonbonding p orbitals; (right) calculation results with bonding states.

4.3.4 Discussion 3: Metal-insulator transition

While the peaks related to the CT seem to support our scenario of the QCE process in SrRuO₃ films, the ones in the low-energy range produce the clearest evidence of MIT. For instance, with decreasing thickness peak A is suppressed rapidly, but peak B gets enhanced simultaneously below the thickness of 5 u.c. The opposite trends of peaks A and B can be easily understood in terms of MIT, as seen in the resistivity data shown in Figure 4.10. We

note that the critical thickness can depend on the growth conditions, according to our fabrication of several SrRuO₃ films used for this work.

According to our CI calculations, peak B can be ascribed to *d-d* excitations between intersite *t*_{2g} orbitals. Electrons are excited to O 2*p* levels that hybridize with Ru *t*_{2g} levels in the valence band, and afterwards relaxation occurs from the *t*_{2g} levels in the conduction band. Although the process can, in principle, involve oxygen *p* levels, it is intrinsically the excitations between two separate *t*_{2g} bands in the valence and conduction bands.

Meanwhile, the origin of peak A can be found by calculating the joint density of states (JDOS) from first-principles calculations with density functional theory. The JDOS represents the probability of allowed interband transitions including absorption or energy-loss functions [Ref.4.30, 4.31]. We calculated the JDOS by considering the energy levels in the valence and conduction bands. In our calculation, the JDOS is given as

$$J(\mathbf{q}) = \sum_{\mathbf{k}} \delta[|\varepsilon_f(\mathbf{k}) - \varepsilon_i(\mathbf{k} - \mathbf{q})|].$$

According to our experimental geometry with a grazing angle, we choose an interband transition with fixed momentum transfer of $\mathbf{q}_{\parallel} = 0.28[2\pi/a]$ and compute the DOS of the energy difference between two levels, which represent the theoretical spectrum of electron-hole excitations. By comparing our calculation results with the experimental data, as shown in Figure 4.10, the calculated JDOS for the electron-hole continuum is in good agreement with the lowest peak seen in bulk SrRuO₃. This means that peak A corresponds to itinerant quasiparticle excitations, while peak B corresponds to excitations between lower and upper Hubbard bands. In this sense, the spectral weight transfer from peak A to

peak B is in good agreement with the MIT in SrRuO₃ thin films. We note that the transfer of spectral weight from peak A to peak B is also consistent with MIT, as seen in the resistivity data: which exhibit the metal-insulator transition with the Mott-Loffe-Regal limit sitting in between the metallic 5 u.c. sample and the insulating 4 u.c sample.

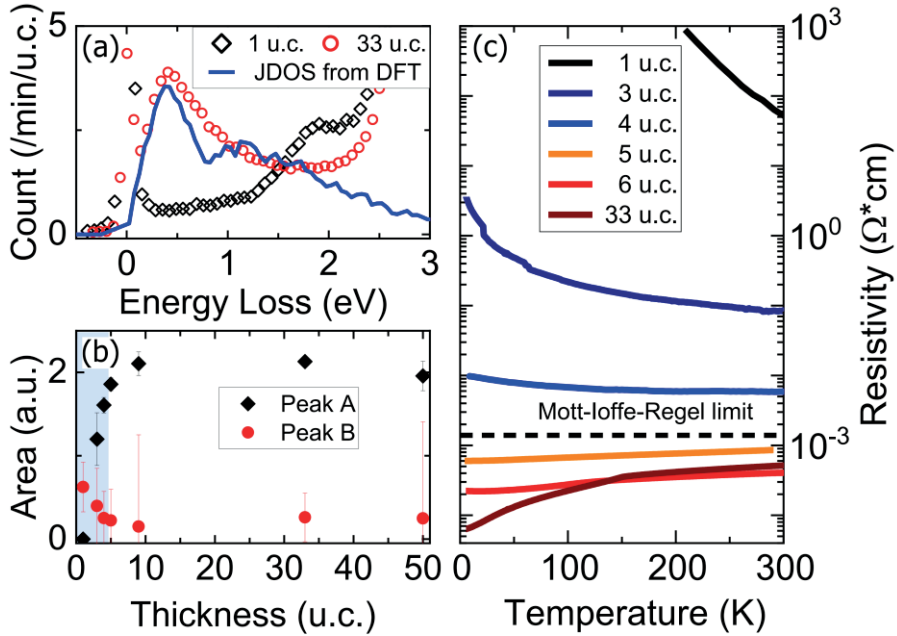


Figure 4.10. (a) and (b) Low-energy excitations are compared to the JDOS from the DFT calculation. We clearly observe the electron-hole continuum in the thick sample, which arises from its metallic phase. The intensity of peak A sharply decreases below 5 u.c., and it completely disappears for the monolayer SrRuO₃. (c) Electrical resistivity of SrRuO₃ thin films with different thickness. The resistivity increases progressively with reducing the thickness and crosses the theoretical Mott-Ioffe-Regel limit between 4 and 5 u.c. It is notable that the critical thickness from RIXS and the resistivity coincide with one another.

Another interesting point is the connection between the QCE and MIT, whose experimental evidence can be readily found in the very thin SrRuO₃ sample. In particular, a new peak is seen to be separated from the d_{xy} level below 5 u.c. and moves towards higher energy, as shown in Figure 4.9. This means that the QCE gets enhanced in thinner SrRuO₃ samples. With the QCE splitting the Ru 4*d* bands, the MIT in SrRuO₃ resembles that of Ca₂RuO₄, which is a classic example of an orbital-selective Mott insulator [Ref.4.32]. For our thinnest sample of 1 u.c. SrRuO₃, the QCE seems to split the otherwise degenerate t_{2g} orbitals, leading to a Mott-type insulating state. Therefore, we can maintain that a new way of realizing a Mott-type insulating phase is found in the ultrathin SrRuO₃ sample with thickness being a control parameter, which is different from the bulk sample.

4.4. Conclusion

In summary, we studied the QCE and MIT in SrRuO₃ thin films as a function of thickness making use of O K edge RIXS experiments. The peaks in the RIXS spectrum are composed with CT excitations extended from 2 to 10 eV, d - d excitations around 2 eV, and electron-hole continuum. The good agreement between the theoretical calculations and the experimental observations of CT excitation peak splitting in the RIXS spectra suggests the orbital-selective QCE in ultrathin SrRuO₃ films. We also found that the suppression of the low-energy excitations arises from the electron-hole continuum across the metal-insulator transition. Finally, our studies provide the clear experimental evidence that the QCE leads to a Mott insulating phase in ultrathin SrRuO₃.

References

- [Ref.4.1] E. Kaxiras, *Atomic and Electronic Structure of Solids* (Cambridge University Press, Cambridge, 2003).
- [Ref.4.2] M. C. Tringides, M. Jalochofski, and E. Bauer, *Phys. Today* **60**, 50 (2007).
- [Ref.4.3] V. B. Sandomirskii, *Sov. Phys. JETP* **25**, 101 (1967).
- [Ref.4.4] F. K. Schulte, *Surf. Sci.* **55**, 427 (1976).
- [Ref.4.5] Y. J. Chang, C. H. Kim, S.-H. Phark, Y. S. Kim, J. Yu, and T. W. Noh, *Phys. Rev. Lett.* **103**, 057201 (2009).
- [Ref.4.6] I. I. Mazin, and D. J. Singh, *Phys. Rev. B* **56**, 2556 (1997).
- [Ref.4.7] B. W. Lee, C. U. Jung, M. Kawasaki, and Y. Tokura, *J. Appl. Phys.* **104**, 103909 (2008).
- [Ref.4.8] H. N. Lee, H. M. Christen, M. F. Chisholm, C. M. Rouleau, and D. H. Lowndes, *Appl. Phys. Lett.* **84**, 4107 (2004).
- [Ref.4.9] M. Stengel and N. A. Spaldin, *Nature* **443**, 679 (2006).
- [Ref.4.10] S. C. Gausepohl and M. Lee, *Appl. Phys. Lett.* **67**, 1313 (1995).
- [Ref.4.11] K. S. Takahashi, A. Sawa, Y. Ishii, H. Akoh, M. Kawasaki, and Y. Tokura, *Phys. Rev. B* **67**, 094413 (2003).
- [Ref.4.12] T. Fuji and M. Kawasaki, *Appl. Phys. Lett.* **86**, 012107 (2005).
- [Ref.4.13] C. H. Ahn, J. M. Triscone, and J. Mannhart, *Nature* **424**, 1015 (2003).
- [Ref.4.14] J. Junquera and P. Ghosez, *Nature* **422**, 506 (2003).

- [Ref.4.15] J. Y. Jo et al., Phys. Rev. Lett. **97**, 247602 (2006).
- [Ref.4.16] R. Ramesh and N. A. Spaldin, Nature Mater. **6**, 21 (2007).
- [Ref.4.17] L. Klein, J. S. Dodge, C. H. Ahn, J. W. Reiner, L. Mieville, T. H. Geballe, M. R. Beasley, and A. Kapitulnik, J. Phys.: Condens. Matter **8**, 10111 (1996).
- [Ref.4.18] A. P. Mackenzie, J. W. Reiner, A. W. Tyler, L. M. Galvin, S. R. Julian, M. R. Beasley, T. H. Geballe, and A. Kapitulnik, Phys. Rev. B **58**, R13318(R) (1998).
- [Ref.4.19] D. Toyota, I. Ohkubo, H. Kumigashira, M. Oshima, T. Ohnishi, M. Lippmaa, M. Takizawa, A. Fujimori, K. Ono, M. Kawasaki, and H. Koinuma, Appl. Phys. Lett. **87**, 162508 (2005).
- [Ref.4.20] J. Xia, W. Siemons, G. Koster, M. R. Beasley, and A. Kapitulnik, Phys. Rev. B **79**, 140407 (2009).
- [Ref.4.21] J. Park, B.-G. Cho, K. D. Kim, J. Koo, H. Jang, K.-T. Ko, J.-H. Park, K.-B. Lee, J.-Y. Kim, D. R. Lee, C. A. Burns, S. S. A. Seo, and H. N. Lee, Phys. Rev. Lett. **110**, 017401 (2013).
- [Ref.4.22] M. Salluzzo, G. Ghiringhelli, N. B. Brookes, G. M. De Luca, F. Fracassi, and R. Vaglio, Phys. Rev. B **75**, 054519 (2007).
- [Ref.4.23] S. Kang, Y. Tseng, B. H. Kim, S. Yun, B. Sohn, B. Kim, D. McNally, E. Paris, C. H. Kim, C. Kim, T. W. Noh, S. Ishihara, T. Schmitt, and J.-G. Park, Phys. Rev. B **99**, 045113 (2019).
- [Ref.4.24] B. H. Kim and J. van den Brink, Phys. Rev. B **92**, 081105(R) (2015).
- [Ref.4.25] J. Park, S.-J. Oh, J.-H. Park, D. M. Kim, and C.-B. Eom, Phys. Rev. B **69**, 085108 (2004).

- [Ref.4.26] J. Kim, J. Chung, and S.-J. Oh, Phys. Rev. B **71**, 121406 (2005).
- [Ref.4.27] K. Maiti, and R. S. Singh, Phys. Rev. B **71**, 161102 (2005).
- [Ref.4.28] J. C. Slater, and G. F. Koster, Phys. Rev. **94**, 1498 (1954).
- [Ref.4.29] G. Cao, and L. DeLong, *Frontiers of 4d- and 5d-Transition Metal Oxides* (World Scientific, Lexington, 2013).
- [Ref.4.30] W. Y. Liang and A. R. Beal, J. Phys. C **9**, 2823 (1976).
- [Ref.4.31] C. I. Cabrera, D. A. Contreras-Solorio, and L. Hernández, Phys. E (Amsterdam, Neth.) **76**, 103 (2016).
- [Ref.4.32] D. Sutter, C. G. Fatuzzo, S. Moser, M. Kim, R. Fittipaldi, A. Vecchione, V. Granata, Y. Sassa, F. Cossalter, G. Gatti, M. Grioni, H. M. Rønnow, N. C. Plumb, C. E. Matt, M. Shi, M. Hoesch, T. K. Kim, T.-R. Chang, H.-T. Jeng, C. Jozwiak, A. Bostwick, E. Rotenberg, A. Georges, T. Neupert, and J. Chang, Nat. Commun. **8**, 15176 (2017).

Chapter 5

Summary and Outlook

5.1 Summary

I studied fundamental excitations and their correlation effects on solids in 2D limits via RIXS experiments. Especially, I made use of two different kinds of RIXS: TM (Ni) L edge and O K edge RIXS. The former case has an advantage to study magnetic and $d-d$ excitation because it excites a core p electron to valence d orbital level. The O K edge is usually a better choice when one wants to study charge-transfer properties in the sample. My research on NiPS₃ with Ni L edge mainly involves the spin-related excitations while one on SrRuO₃ with O K edge show CT excitations.

To investigate the specific excitations related to magnetic properties, I explored an up-and-coming system called magnetic vdW material: NiPS₃. The RIXS study involves magnon dispersions below 100 meV and multiplet excitations around 1.44 eV of energy loss. The magnon dispersions including both single- and two-magnon are the obvious evidence of XXZ-type antiferromagnetism in NiPS₃. The small charge transfer energy between a Ni ion and an S ligand lead to the advent of complex multiplet structure of NiPS₃. Especially, a multiplet excitation between the ZRT and ZRS state results in the sharp peak

at 1.44 eV on RIXS spectra. The sharpness of the peak shows the unusually long lifetime and stability of the excitation, which comes from the strong spin-charge coupling of self-doped NiPS₃ and the local dipole moment due to different hole-density counter to the long range magnetic ordering.

The studies on the ultrathin film of SrRuO₃ show the orbital-selective MIT. The RIXS spectra of SrRuO₃ as a function of thickness are mainly composed of three parts: electron-hole continuum (~1 eV), *d-d* (2 eV) and CT (2~10 eV) excitations. The spectral weight transfers from electron-hole continuum to *d-d* excitation reducing the thickness of the sample, which indicates the MIT of SrRuO₃. At the same time, the peak splitting of CT excitation provides a clue of QCE. The QCE in the ultrathin limits represents the energy splitting between *t_{2g}* orbitals with different geometry. From those results, the MIT on SrRuO₃ is orbital-selective.

5.2 Outlook

The RIXS study on NiPS₃ implies that the magnetic interactions between Ni ions can be explained with an effective XY-type Hamiltonian. While the spin of Ni has a certain DOF along z-axis, the strong single-ion anisotropy confines the freedom of spins. Thus, the spins lies on xy plane like XY-type magnetism, which is one of the most famous 2D magnetism model. As the layers of NiPS₃ have weak vdW interaction, it is possible to exfoliate and fabricate a single-layer sample. This opens a unique opportunity to research a “real” 2D magnetism. It will be a chance to realize the emergent phenomena on XY-type magnetism

such as BKT transition and vortex-antivortex pair fluctuations, which are theoretically predicted up to now.

As shown in the SrRuO₃ case, RIXS is also a powerful tool to observe respective orbitals and their energy levels in solids. Combined with spin DOF and special conditions, the levels can be split and result in spin-orbit entangled states. The 4*d* TMs such as Ru are in very special limit where the quantity of electron correlation is comparable to that of spin-orbit coupling. This extraordinary condition can induce an exotic ground state so-called spin-orbit entangled *J* state. For example, Ca₂RuO₄, a quasi-2D antiferromagnet, retains fully quenched orbital momentum due to the compressive crystal field distortion along its *c*-axis, and it results in a non-magnetic singlet *J*=0 ground state. A recent inelastic neutron scattering successfully captures the singlet-triplet excitation and more importantly the amplitude fluctuations of the local magnetization-the Higgs mode [Ref.5.1]. The studies on spin-orbit entangled states will explain the questions of fundamental physics such as the role of spin-orbit coupling in 4*d* TM compounds, and also can drive a technological design of new materials like functional devices or quantum computations.

References

[Ref.5.1] B.J. Kim, H. Ohsumi, T. Komesu, S. Sakai, T. Morita, H. Takagi, and T. Arima, *Science* **323**, 1329 (2009).

Publication lists

- [1] **Soonmin Kang**, Kangwon Kim, Beom Hyun Kim, JongHyeon Kim, Jae-Ung Lee, Sungmin Lee, Kisoo Park, Seokhwan Yun, Taehun Kim, Laurent Chapon, Kejin Zhou, Young-Woo Son, Jae Hoon Kim, Hyeonsik Cheong, and Je-Geun Park, “*Resolution-limited magnetic exciton in van der Waals antiferromagnet NiPS₃*”, in preparation.
- [2] **Soonmin Kang**, Yi Tseng, Beom Hyun Kim, Seokhwan Yun, Byungmin Sohn, Bongju Kim, Daniel McNally, Eugenio Paris, Choong H. Kim, Changyoung Kim, Tae Won Noh, Sumio Ishihara, Thorsten Schmitt, and Je-Geun Park, “*Orbital-selective confinement effect of Ru 4d orbitals in SrRuO₃ ultrathin film*”, Phys. Rev. B **99**, 045113 (2019)
- [3] Ganbat Duvjir, Byoung Ki Choi, Iksu Jang, Søren Ulstrup, **Soonmin Kang**, Trinh Thi Ly, Sanghwa Kim, Young Hwan Choi, Chris Jozwiak, Aaron Bostwick, Eli Rotenberg, Je-Geun Park, Raman Sankar, Ki-Seok Kim, Jungdae Kim, and Young Jun Chang, “*Emergence of a Metal–Insulator Transition and High-Temperature Charge-Density Waves in VSe₂ at the Monolayer Limit*”, Nano Lett. **18**, 5432 (2018)
- [4] Taehun Kim, Sumin Lim, Jaeyoung Hong, Soon Gu Kwon, Jun Okamoto, Zhi Ying Chen, Jaehong Jeong, **Soonmin Kang**, Jonathan C. Leiner, Jung Tae Lim, Chul Sung Kim, Di Jing Huang, Taeghwan Hyeon, Soonchil Lee, and Je-Geun Park, “*Giant thermal hysteresis in Verwey transition of single domain Fe₃O₄ nanoparticles*”, Scientific Reports **8**, 5092 (2018)
- [5] Seongil Choi, Hasung Sim, **Soonmin Kang**, Ki-Young Choi, and Je-Geun Park,

“Doping effects on trimerization and magnetoelectric coupling of single crystal multiferroic (Y, Lu)MnO₃”, J. Phys.: Condens. Matter **29**, 095602 (2017)

[6] Jae-Ung Lee, Sungmin Lee, Ji Hoon Ryoo, **Soonmin Kang**, Tae Yun Kim, Pilkwang Kim, Cheol-Hwan Park, Je-Geun Park, and Hyeonsik Cheong, “Ising-Type Magnetic Ordering in Atomically Thin FePS₃”, Nano Lett. **16**, 7433 (2016)

[7] Cheng-Tai Kuo, Michael Neumann, Karuppanan Balamurugan, Hyun Ju Park, **Soonmin Kang**, Hung Wei Shiu, Jin Hyoun Kang, Byung Hee Hong, Moon-sup Han, Tae Won Noh, and Je-Geun Park, “Exfoliation and Raman Spectroscopic Fingerprint of Few-Layer NiPS₃ Van der Waals Crystals”, Scientific Reports **6**, 20904 (2016)

국문초록

이차원 전이 금속 화합물의 독특한
들뜸 스펙트럼 연구

강순민

물리천문학부 물리학전공

서울대학교 대학원

응집물질 물리학에서 “차원”이라는 변수는 기존 고체에서 다뤄져 온 것과는 다른 새로운 발현 현상을 보여준다. 특히 그 중에서도 “이차원”은 자연에 존재하는 기초 자유도 (fundamental degrees of freedom)의 측면에서 매우 흥미롭고 중요하지만 아직까지도 그에 대한 이해는 부족하다. 자유도의 상호작용과 이차원에서 두드러지는 양자 요동 (quantum fluctuation)의 효과는 응집 물질을 설명하는 고전 모형으로는 설명할 수 없는 양자 스핀 액체 (quantum spin liquid), 독특한 초전도 (unconventional superconductivity), 양자 홀 효과 (quantum Hall effect) 등의 독특한 물리 현상을 야기한다. 공명 비탄성 엑스선 산란 실험 (resonant inelastic x-ray scattering, RIXS)은 물질의 여기 상태를 관측함으로써 물질 내 자유도와 상호작용을 직접적으로 관측할 수 있는 실험 기법이다. 이 논문에서는 RIXS 실험 기법을 통해 이차원 강상관계물질의 다양한 여기 상태를 관측한 결과를 정리하였다. 특히, NiPS_3 의 자성 구조와 강한 스핀-전하 상호작용으로 인한 독특한 발현

현상과 SrRuO_3 박막에서 나타나는 양자 속박 효과 (quantum confinement effect)로 인한 금속-절연체 상전이를 연구하였다.

NiPS_3 는 160 K 이하의 저온에서 지그재그 형태의 반강자성을 띠는 물질이다. 고해상도의 Ni L_3 edge RIXS 실험은 단일 마그논 분산과 이중 마그논 연속체를 통해 물질의 자성 구조를 정확하게 알아내는데 중요한 단서를 제공한다. 특히, 이를 통해 NiPS_3 의 자성 구조를 설명하는 XXY 형태의 해밀토니안 모형을 알아냄으로써 기존에 이론적으로 정립된 이차원 XY 모델을 이해하는 데 실마리를 얻을 수 있다. 또한 NiPS_3 의 니켈 (Ni)과 황 (S) 이온 사이의 전하 전이 에너지는 다른 물질에 비해 매우 작은 값을 가지기 때문에 서로 다른 여러가지 전하 배열을 가질 수 있다. 다양한 전하 배열의 결합은 NiPS_3 내에 복잡한 다중항 상태를 만든다. 이러한 다중항 상태의 여기 상태를 관측함으로써 물질의 독특한 특성들을 연구할 수 있는데, 특히 본 연구에서는 리간드 홀의 스핀-뒤집음 (spin-flip)으로 형성되는 Zhang-Rice 단일항 상태를 통해 강한 스핀-전하 상호작용을 확인하였다.

SrRuO_3 박막의 경우, O K edge RIXS 실험을 통해 두께에 따른 전자 구조를 관측하여 전자 자유도와 오비탈 자유도의 상호작용을 주로 연구하였다. 전하 전이로 인한 여기 상태를 관측함으로써 오비탈 의존성을 가진 양자 속박 효과가 물질 내 루테튬 (Ru)의 오비탈 에너지 준위를 변화시킴을 확인하였다. 게다가 저에너지 영역에서 나타나는 전자-홀 연속 상태 (electron-hole continuum)의 변화는 SrRuO_3 의 금속-절연체 상전이를 분명히 보여준다. RIXS 실험의 결과를 통해 해당 상전이와 양자 속박 효과가 동시에 일어나는 것을 관측함으로써 두께가 매우 얇은 박막 영역에서 오비탈에 가해지는

기하학적 제한이 SrRuO_3 의 금속-절연체 상전이를 유도함을 밝혀내었다.

주요어: 공명 비탄성 엑스선 산란, 강상관계물질, 자성 반데르발스 물질, 스핀-전하 상호작용, 마그논, 다중항 상태, 양자 속박 효과

학 번: 2013-20350

감사의 글

대학원에 입학하고 6 년이라는 길다면 길고 짧다면 짧은 시간이 흘러 어느덧 졸업을 앞두고 있습니다. 박사 학위를 취득하는 동안 정말 다양한 경험을 하고 수 많은 실패와 성공 속에서 큰 성장을 이룰 수 있었습니다. 이러한 꿈만 같은 순간을 맞이할 수 있었던 것은, 이 힘든 과정을 버틸 수 있었던 것은 결코 저 혼자만의 힘이 아니었습니다. 박사 학위라는 길을 걸어오는 동안 저에게 도움을 주셨던 많은 분들께 이렇게 짧은 글로나마 감사의 마음을 표현하고자 합니다.

우선 저의 지도 교수님, 박제근 교수님께 감사드립니다. 교수님께서는 언제나 열정적인 지도로 제가 학자로서 그리고 사회의 한 구성원으로서 살아갈 방법과 방향을 알려주셨습니다. 연구단의 그 누구보다도 먼저 하루를 시작하시는 한결같은 성실함을 바탕으로 치열하고 열정적으로 연구를 수행해 나가시는 교수님의 모습은 저에게 늘 귀감이 되었습니다. 제가 연 이은 실패 속에서 갈 길을 헤맬 때, 중요한 갈림길에서 고민할 때도 진심으로 함께 고민해주시고 나아가갈 방향을 제시해 주셨습니다. 쉽지 않은 주제로 연구를 진행하는 동안에도 오랫동안 저를 믿어 주시고 지원해 주신 덕분에 흔치 않은 기회를 얻고 좋은 경험을 할 수 있었습니다.

제 박사 학위 논문의 심사를 맡아 주신 차국린 교수님, 박철환 교수님, 김도현 교수님, 김범준 교수님께도 감사의 말씀을 전합니다. 심사 과정을 통해 주신 조언과 질문을 통해 제가 미처 생각하지 못했던 부분에 대해 깊게 고민하고 다양한 관점에서 저의 연구 주제를 다시 한 번 바라볼 수 있는 기회가 되었습니다. 바쁘신 와중에도 성심껏 제 학위 논문을 심사해주시고 학위 발표를 경청해 주셔서 감사합니다.

더불어 제 학위 기간동안 곁에서 함께한 연구실 동료들께도 감사의 말씀을 드리고 싶습니다.

저에게 좋은 사람의 표본이 되어 주신 성일이 형, 형을 통해 누군가에게 따뜻한 사람이 되는 것이 어떤 의미인지 배울 수 있었습니다. 늘 큰 형처럼 버팀목이 되어 주셔서 감사드립니다. 이 연구실로 저를 이끌어 주고 나아가 저에게 늘 멘토가 되어 주셨던 재홍이 형, 아직도 23 동에서 형을 처음 만났던 6 년전 그 순간이 기억이 납니다. 처음 연구를 시작했을 때부터 지금까지 언제나 진심 어린 조언을 해 주시고

아낌없이 가르쳐 주신 덕분에 학문적으로도 인간적으로도 참 많은 것을 배웠습니다. 누구보다 따뜻하면서도 이성적인 형의 모습은 저에게 하나의 목표였습니다. 진심으로 감사드립니다. 저에게 연구의 기본을 가르쳐 주신 상현이 형, 제가 수행했던 많은 실험은 형의 가르침으로부터 시작했습니다. 기초적인 시료 합성부터 수 많은 물성 측정과 구조 분석까지, 제 연구의 기반을 단단하게 다져준 형에게 이렇게 다시 한 번 감사의 말씀을 전합니다.

짧은 시간이었지만 저에게 제 연구의 시작을 든든하게 지켜 주셨던 찬영이 형, 제가 그 당시에는 이해하지 못 했던 형의 많은 조언들이 시간이 갈수록 정말 큰 도움이 되었습니다. 제 박사 과정동안 가장 오랜 기간을 함께한 선배이자 허물없는 친구 하성이, 친절하고 꼼꼼하게 가르쳐준 많은 실험 방법과 분석 방법은 연구를 진행하며 막히는 것이 있을 때마다 큰 도움이 되었습니다. 살아가며 만난 사람 중 가장 비상한 주성이 형을 통해서 연구자에게 꼭 필요한 다양한 관점과 유연한 사고방식을 배울 수 있었습니다. 형과의 토론을 통해서 제 연구의 빈틈을 찾을 때도, 새로운 돌파구를 찾을 때도 많았습니다.

6 년내내 바로 옆자리에 앉아 있었던 대학원 동기 환범이 형, 형이 늘 든든한 버팀목이 되어주어 그 기간을 버텨낼 수 있었습니다. 힘들 때는 많이 의지가 되었고 서로가 좋은 일이 있을 때는 정말 자기 일처럼 기뻐해주는 형이 동기인 것은 정말 큰 행운이었습니다. 새로운 환경에서 적응하며 연구하고 있을 형의 미래가 늘 행복하길 바랍니다. 매사에 능하고 똑똑한 기수에게는 제가 분광학이라는 새로운 분야에 도전할 때 많은 도움을 받았습니다. 익숙하지 않은 문제에 대한 풀이법을 고민할 때 실용적이고 저에게 꼭 필요한 해결 방향을 제시해주어 고맙습니다. 앞으로 어디서 어떤 일을 해 나가더라도 잘 해낼 것이라 믿어 의심치 않습니다. 내 짝궁 석환이, 지난 몇 년간 이 학위 논문에 포함된 많은 실험을 하는 동안, 그 가장 힘들었던 순간들을 가장 가까운 곳에서 함께 해주어 감사합니다. 학부 동기이자 동갑내기 친구이지만 늘 많은 것을 배웁니다. 끊임없이 고민하고 열정적이고 적극적으로 공부하며 물리학자의 길을 묵묵히 걸어가는 석환이를 보면 학자로서 가져야 할 마음가짐에 대해 다시 한 번 생각하게 됩니다.

후배이지만 어른스럽고 결단력 있는 성민이, 연구실에 있을 때 좀 더 잘해주고 힘이 되어주지 못해 미안합니다. 제 학위 논문의 주제 중 한 가지인 NiPS₃ 연구는 물론 지금의 반데르발스 물질 팀의 많은 연구가 성민이의 공이 크다는 것을 알고 있습니다. 곧 새로운 가정을 이루게 될 성민이의 앞날에 축복이 가득하길 바랍니다. 늘 자기의 자리에서 묵묵히 최선을 다하는 태훈이, 중간에 연구 주제를 크게

바꾸면서 걱정도 많이 했지만 긍정적인 마음과 성실함으로 지금은 연구실의 누구보다도 특별한 길을 걷고 있는 모습을 보고 있다면 괜스레 마음이 뿌듯해 집니다. 지금처럼 끈기있게 연구를 이어간다면 어느 새 남들은 생각치도 못했던 새로운 연구를 할 날이 올 거라 믿습니다. 책임감 있고 든직한, 반데르발스 팀의 실질적 팀장 수한이, 비록 나보다 나이는 어리지만 지금 연구실의 든든한 만형 역할을 잘 해내주어 미안함과 고마움이 동시에 듭니다. 지금까지 해왔던 것처럼 항상 자신의 중심을 잃지 않고 우직하게 본인의 연구에 집중하여 좋은 성과를 이루길 바랍니다. 뚜렷한 주관을 가지고 연구하는 인호, 내가 선배들에게 받았던 것처럼 조금 더 친절하게 많은 것들을 전해주지 못해 미안한 마음이 큼니다. 지금은 다소 연구에 힘든 부분이 있더라도 언제라도 도와줄 좋은 동료들이 곁에 있다는 것을 명심하고 함께 나눌 수 있으면 더 좋은 연구자가 될 수 있을 것입니다. 우리 팀의 막내 채빈이, 말년 병장 같은 연구실 선배 따라 다니느라 고생 많았습니다. 처음 연구실을 알아보고자 상담을 왔을 때부터 총명하고 성실한 친구라는 것을 느낄 수 있었습니다. 지금 당장은 작게 느껴지더라도 자신이 맡은 연구를 하나씩 하나씩 해 나가다 보면 어느새가 훌쩍 성장해 있는 자기 자신을 발견하게 될 것입니다. 늘 골똘히 생각 중인 유진이, 마음 고생도 많고 고민도 많았을 텐데 앞으로는 노력한 만큼 좋은 연구 성과를 낼 수 있길 바랍니다. 조용하지만 늘 밝고 매사에 최선을 다하는 정현이, 연구실에 잘 적응해 나가고 있어 이제는 마음이 놓입니다. 지금처럼 묵묵하게 최선을 다해 좋은 연구를 많이 하길 바랍니다. 새롭게 연구실에 들어온 희준이와 영관이, 새로운 환경에 잘 적응하여 좋은 연구자로 성장하길 바랍니다.

제 연구에 도움을 주셨던 연구자 분들께도 감사의 말씀을 드립니다. 먼저 제 비탄성 엑스선 산란 실험의 해석의 대부분을 함께 해 주신 김범현 박사님, 쉽지 않은 계산과 해석, 그리고 논문 작성까지도 많은 도움을 주셔서 감사합니다. 박사님께서 계시지 않았다면 이 학위 논문의 많은 부분에 구멍이 뚫려 있었을 것입니다. 이 글을 빌어 다시 한 번 박사님의 노고에 감사드립니다. 까다로운 요청에도 고품질의 박막 시료 제작을 도맡아 해 주신 김봉주 박사님과 손병민 학생, 두 분 덕분에 제가 원하는 연구를 진행할 수 있었고 이렇게 성과를 낼 수 있었습니다. 밤 잠 설치며 노력하시는 모습에 많은 자극을 받았습니다. 곁에서 연구에 대한 조언을 해주시고 연구에 지원을 해 주신 노태원 교수님과 김창영 교수님께 감사드립니다. 그리고 제 연구 주제에 대한 추가 실험과 함께 실험 해석에 대한 논의를 함께 해주시고 현재 논문을 같이 작성중인 서강대학교 정현식 교수님, 연세대학교 김재훈 교수님, 고등과학원 손영우 교수님께도 감사의 말씀을 전합니다. 새롭게 개발한 비탄성 엑스선 산란 실험의 시험 가동에 기회를 주시고 자신의 연구처럼 꾸준하게 관심을 가져 주신 영국 Diamond Light Source 의 Kejin Zhou 박사님과 연구진들에게도

감사의 말씀을 전합니다. 세계 최고의 빔라인에서 실험할 기회를 주신 스위스 Paul Scherrer Institut 의 Thorsten Schmitt 박사님과 실험을 함께 수행한 Yi Tseng 에게도 감사드립니다.

제가 학위 기간동안 소속되어 있었던 IBS-CCES 의 다른 식구분들에게도 감사드립니다. 지원팀의 박원구 박사님, 이인호 선생님, 강태동 박사님, 김금채 선생님, 배현이 선생님, 조혜인 선생님, 이나현 선생님, 송인경 박사님, 장비와 물품 관리는 물론이고 사소한 일부터 큰 공사까지 아낌없는 지원과 헌신으로 연구에만 집중할 수 있었습니다. 행정팀의 전지현 실장님, 김정란 선생님, 주양희 선생님, 지정은 선생님, 손주희 선생님, 박주영 선생님, 그리고 권지성 선생님과 엘리카 선생님께도 감사드립니다. 연구 특성상 많은 물품을 구매하고 잦은 국내외 출장을 다녀왔고 그 과정에서 많은 일들을 해결해주시고 원활히 연구를 진행할 수 있도록 도와 주셔서 감사드립니다.

마지막으로 언제나 제 곁을 지켜주고 응원해준 가족들께 감사드립니다. 저의 영원한 이상인 아버지, 힘들 때나 기쁠 때나 언제나 같은 곳에 서서 제가 쉬어갈 세상 어느 곳보다 튼튼한 그늘막이 되어주셔서 감사합니다. 당신께서 계시기에 저는 늘 안정감을 느끼고 나아갈 방향을 찾습니다. 제가 늘 닦고 싶은 어머니, 애정 가득한 응원과 진심 어린 조언은 지칠 때 다시 일어설 수 있는 힘이고 흔들리는 저를 곧은 길로 이끌어주는 등불입니다. 어머니의 사랑과 지지가 있었기에 지금의 이 자리까지 올 수 있었습니다. 못난 형의 가장 가까운 곳에서 늘 응원해주고 함께 걸어가는 든든한 동생에게도 감사합니다.

2019년 7월 26일

강 순 민

